NASA/CR—2001-210715

Viscoplastic Model Development to Account for Strength Differential: Application to Aged Inconel 718 at Elevated Temperature

Saiganesh Iyer
Pennsylvania State University, University Park, Pennsylvania

April 2001

The NASA STI Program Office . . . in Profile

Since its founding, NASA has been dedicated to the advancement of aeronautics and space science. The NASA Scientific and Technical Information (STI) Program Office plays a key part in helping NASA maintain this important role.

The NASA STI Program Office is operated by Langley Research Center, the Lead Center for NASA's scientific and technical information. The NASA STI Program Office provides access to the NASA STI Database, the largest collection of aeronautical and space science STI in the world. The Program Office is also NASA's institutional mechanism for disseminating the results of its research and development activities. These results are published by NASA in the NASA STI Report Series, which includes the following report types:

- TECHNICAL PUBLICATION. Reports of completed research or a major significant phase of research that present the results of NASA programs and include extensive data or theoretical analysis. Includes compilations of significant scientific and technical data and information deemed to be of continuing reference value. NASA's counterpart of peer-reviewed formal professional papers but has less stringent limitations on manuscript length and extent of graphic presentations.

- TECHNICAL MEMORANDUM. Scientific and technical findings that are preliminary or of specialized interest, e.g., quick release reports, working papers, and bibliographies that contain minimal annotation. Does not contain extensive analysis.

- CONTRACTOR REPORT. Scientific and technical findings by NASA-sponsored contractors and grantees.

- CONFERENCE PUBLICATION. Collected papers from scientific and technical conferences, symposia, seminars, or other meetings sponsored or cosponsored by NASA.

- SPECIAL PUBLICATION. Scientific, technical, or historical information from NASA programs, projects, and missions, often concerned with subjects having substantial public interest.

- TECHNICAL TRANSLATION. English-language translations of foreign scientific and technical material pertinent to NASA's mission.

Specialized services that complement the STI Program Office's diverse offerings include creating custom thesauri, building customized data bases, organizing and publishing research results . . . even providing videos.

For more information about the NASA STI Program Office, see the following:

- Access the NASA STI Program Home Page at ***http://www.sti.nasa.gov***

- E-mail your question via the Internet to help@sti.nasa.gov

- Fax your question to the NASA Access Help Desk at 301–621–0134

- Telephone the NASA Access Help Desk at 301–621–0390

- Write to:
  NASA Access Help Desk
  NASA Center for AeroSpace Information
  7121 Standard Drive
  Hanover, MD 21076

NASA/CR—2001-210715

Viscoplastic Model Development to Account for Strength Differential: Application to Aged Inconel 718 at Elevated Temperature

Saiganesh Iyer
Pennsylvania State University, University Park, Pennsylvania

Prepared under Cooperative Agreement NCC3–597

National Aeronautics and
Space Administration

Glenn Research Center

April 2001

Acknowledgments

I would like to thank Professor C.J. Lissenden for advising me on the thesis and am grateful to him for encouraging me throughout the duration of this research. I also thank Professor F. Costanzo, Professor D.A. Koss, Professor A.D. Belegundu, and Professor R.A. Queeney for reading of the thesis and suggesting useful modifications to it. The experimental results that I present were conducted in the Fatigue and Structures Laboratory at the NASA Glenn Research Center by Professor C.J. Lissenden, Dr. Brad Lerch, Chris Gil, and Jason Colaiuta. I am obligated to Professor Anindya Chatterjee and Professor F. Costanzo for enlightening discussions on the mathematical aspects of the formulation. The metallography conducted by Chris Gil is appreciated. I am grateful to Senthil Gopinathan, Dr. Divas Sanwal, Raviprakash Jayaraman, and Nikhil Rao for interesting technical discussions. Computer support by Abraham Mathew, Mark Catalano, and Anirudh Modi is gratefully acknowledged. Assistance in document preparation by Raviprakash Jayaraman and Balaji Venkataraman is appreciated. I thank Sanjay Rangan for useful tips for presentation of this work. Finally, I would like to thank NASA Glenn Research Center for sponsoring this work (NCC3-597).

Available from

NASA Center for Aerospace Information
7121 Standard Drive
Hanover, MD 21076
Price Code: A10

National Technical Information Service
5285 Port Royal Road
Springfield, VA 22100
Price Code: A10

Available electronically at http://gltrs.grc.nasa.gov/GLTRS

Contents

List of Figures

List of Tables

List of Symbols

σ_{ij}	Stress tensor
σ_i	Principal stresses
σ_y	Yield Stress
σ_t	Yield Stress in tension
σ_c	Yield Stress in compression
S_{ij}	Deviatoric stress
α_{ij}	Internal stress
a_{ij}	Internal deviatoric stress
Σ_{ij}	Effective deviatoric stress
I_i	Invariants of stress tensor
J_i	Invariants of deviatoric stress tensor
$\tilde{J}_i$	Invariants of effective stress tensor
J_i'	Invariants of internal stress tensor
f	Yield Function
g	Potential function
ϵ_{ij}^I	Inelastic strain
Λ_β	Internal Strain
$\dot{\epsilon}_{ij}^I$	Inelastic strain rate
$\dot{\Lambda}_\beta$	Internal strain rate

U_c	Complementary strain energy
n_{ij}	Normal to yield surface
u	Internal energy
S	Entropy
q	Heat Flux
$\overline{H}$	Helmholtz free energy
Ω	Dissipation potential
Φ	Gibb's potential
C_{ijkl}	Stiffness tensor
Q_{ijkl}	Internal compliance tensor
L_{ijkl}	Internal stiffness tensor
F	Function of effective stress invariants
G	Function of internal stress invariants
κ,μ,n	Flow law parameters
m,R	Recovery parameters
$H\beta$	Hardening parameters
a,b,c,m_1	Threhold surface parameters

Chapter 1

Introduction

Inelastic behavior of materials is a subject that has fascinated engineers and researchers over many decades. Sustained interest in this topic is due to its direct relevance in numerous engineering applications. The real challenge is to accurately predict inelastic deformation when the material is subjected to thermal transients and complex mechanical loading. Gas turbine engines, power generation systems, and automotive engines are just a few examples of where materials experience complex thermo-mechanical loading. In these situations, the material is subjected to multiaxial states of stress, different loading rates and variable temperature conditions. The accurate representation of stress, strain and temperature fields within the structural components depends strongly on the mathematical representations or constitutive equations of the inelastic behavior of these materials at various temperature levels. Further, to be generally applicable, the constitutive equations must be expressed in tensorial form.

The total strain in the material can be separated into elastic and inelastic parts. Classical decomposition of the inelastic component into time independent (plastic) and time dependent (creep) contributions facilitates modeling of material behavior. The plastic component is considered to be history dependent, i.e., the current plastic strain depends on the loading history. The creep component is treated as time dependent and is responsible for deformation when the external loads and the temperature are held constant.

At elevated temperatures, however, the classical decomposition into plastic and creep strains

breaks down. In structural alloys creep and plastic strains occur simultaneously and interactively. This suggests that we need a unified constitutive model to represent deformation of metals at elevated temperatures. Many such models have been developed in the last few decades (e.g. Walker [1981], Bodner [1987], Helling and Miller [1987], Robinson and Duffy [1990], Freed and Walker [1995], Arnold et al [1996]). Most constitutive theories use internal variables and appropriate evolutionary equations for simultaneously treating all aspects of inelastic deformation including plasticity, creep and stress relaxation. These theories are based on thermodynamics of irreversible processes and will be elaborated on in Chapter 3.

1.1 Materials for high temperature applications

Safety is a primary concern in aerospace applications. Thus, all substructures must remain structurally sound during all phases of flight. For gas turbine engine components, materials having good strength properties over a wide range of temperatures are required. Metal-matrix composites (MMCs) and superalloys possess this quality and hence are suitable for this application. Owing to its complexity, the fabrication of MMCs is expensive and time consuming. Hence, superalloys like Inconel 718 (a Nickel-based alloy) and Haynes 188 (a cobalt-based alloy) are more popular than MMCs in the aerospace industry for engine applications. Aged Inconel 718 is strengthened by precipitate hardening, in which fine particles of a second phase are dispersed throughout the grains, thereby slowing down the movement of dislocations. The physical mechanisms responsible for strengthening of this alloy are explained in Chapter 2.

1.2 Objective of the present research

Inconel 718 is a wrought nickel-based alloy that is precipitation hardenable to obtain high strength and is the material to be investigated in the present research.

Recent experiments on Inconel 718 indicate that the yield stress and subsequent flow stress are significantly higher in compression than in tension (Gil et al [1999b]). This phenomenon, known as the strength differential (SD), is observed for a wide range of temperatures as

shown in Figure 1.1. Figure 1.1(a) shows higher yield and post-yield stresses in compression at $650°C$. Yield loci at $23°C$ and $650°C$, shown in Figure 1.1(b), clearly show eccentricity in the compressive stress direction. The SD effect can be mathematically defined as

$$SD = 2\left(\frac{\sigma_c - \sigma_t}{\sigma_c + \sigma_t}\right) \times 100 \tag{1.1}$$

where σ_c and σ_t are yield strengths in uniaxial compression and uniaxial tension, respectively. At the initiation of yielding the SD has a high value; it then decreases, and finally reaches a constant value at higher inelastic strains.

A yield function, based solely on the second invariant of deviatoric stress (J_2) is not able to correctly represent a material with a SD. **Thus, the goal of the current work is to generalize a viscoplastic model, currently based solely on J_2, to account for the strength differential effect.**

1.3 Generalization of Plasticity Theory

Having established the need to generalize the yield function to capture the SD effect, it is worthwhile to look at some yield functions and flow rules used by other researchers, that deviate from J_2 plasticity theory. This section starts with some basic elements of J_2 plasticity followed by instances where deviations from the classical approach are required to capture material behavior.

1.3.1 Metal Plasticity

(Hill [1950], Mendelson [1983], Lubliner [1990], Chen [1994], Khan and Huang [1995])

At the continuum level, the initial material behavior is taken to be linear elastic up to the yield point. The yield surface delineates the current elastic region in stress space. For an elastically isotropic metal, yielding depends on stress, temperature, and internal state (described by hardening or internal state variables). Under isothermal conditions, initial

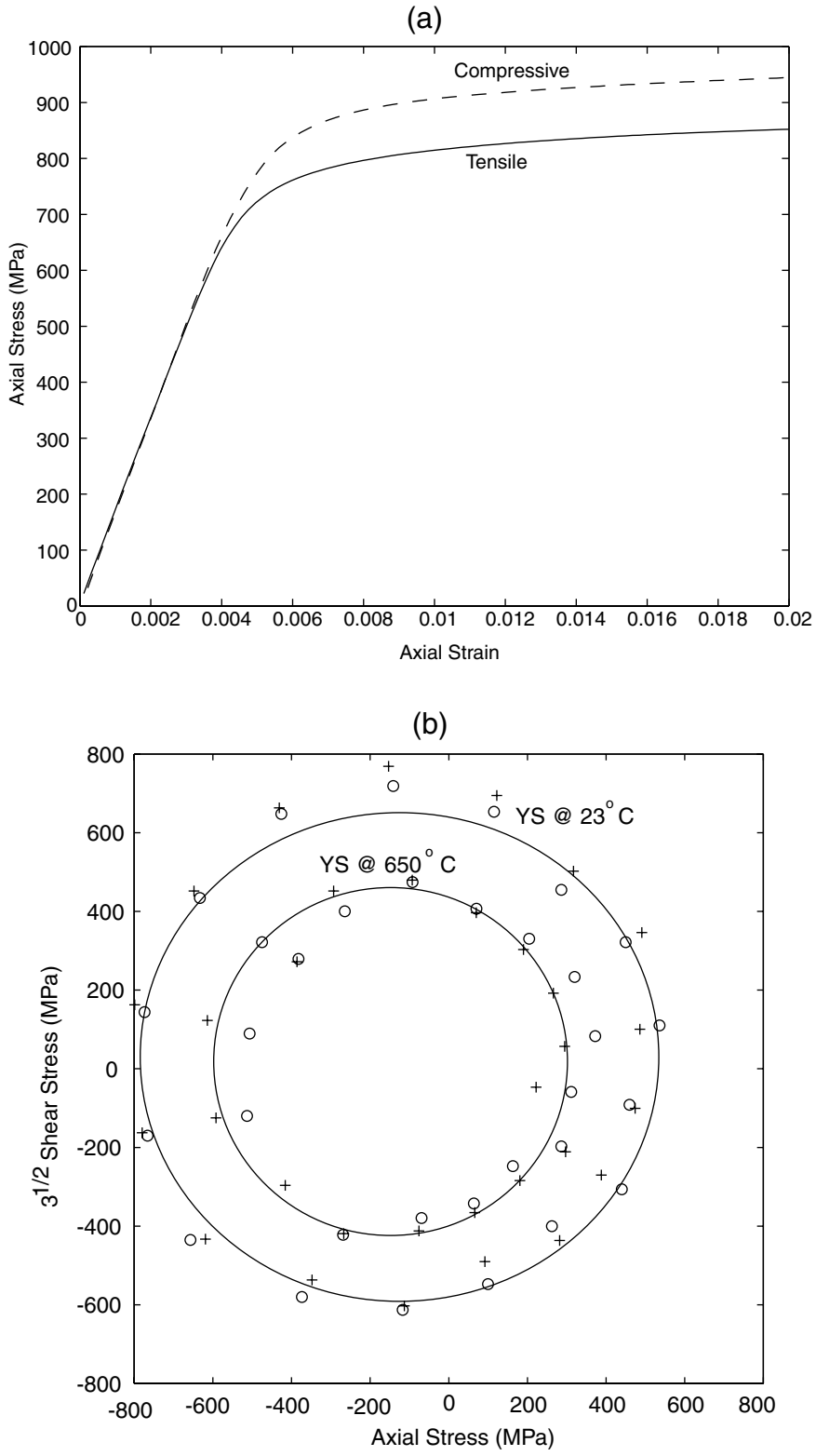

Figure 1.1: Strength Differential in aged Inconel 718: (a) Uniaxial Response at 650°C (b) Yield Loci for a 30μm/m offset strain definition

yielding depends only on the stress state, which is often described by three stress invariants:

$$\begin{aligned} I_1 &= \sigma_{ii} \\ J_2 &= \frac{1}{2} S_{ij} S_{ij} \\ J_3 &= \frac{1}{3} S_{ij} S_{jk} S_{ki} \end{aligned}$$

where I_1 is the first stress invariant, J_2 and J_3 are the second and third deviatoric stress invariants respectively, σ_{ij} and S_{ij} denote the Cauchy and deviatoric stress components respectively. The yield function can be expressed as

$$f(\sigma_{ij}) = f(I_1, J_2, J_3) = 0. \tag{1.2}$$

Physically, I_1 represents the hydrostatic stress and J_2 represents the distortional energy in the material. Though no definite physical quantity is attributed to J_3, it can be treated as a weighting parameter that induces asymmetry in yield and flow behavior between tension and compression.

Based on the work of Bridgman [1952], yielding in most metals (e.g. mild steel, copper, aluminum) was found to be relatively insensitive to hydrostatic pressure. This suggests that I_1 is unimportant in the definition of yield. Also, for many metals the tensile and compressive flow behavior are identical (e.g. aluminum, titanium, unaged maraging steel, unaged Inconel 718), making J_3 unimportant. Hence the yield function depends only on J_2 and the yield surface is an infinite cylinder in the principal stress space with its axis along the hydrostatic stress line. The von Mises yield criterion takes the form of a cylinder with a circular cross-section, resulting in

$$\sqrt{3J_2} = \sigma_y \tag{1.3}$$

where σ_y is the uniaxial tensile yield strength.

When applied to these materials, Drucker's stability postulate (Drucker [1951] and [1959]) results in the inelastic strain rate vector being normal to the yield surface. Thus, the yield function can be treated as a plastic potential and the inelastic strain rate can be determined by use of an associated flow law,

$$\dot{\epsilon}_{ij}^I = \dot{\lambda} \frac{\partial f}{\partial \sigma_{ij}} \tag{1.4}$$

where $\dot{\lambda}$ is a scalar that is determined from the consistency condition discussed in Chapter 3. Hence classical plasticity theory, when applied to metals, suggests that the yield function is based only on shear stress and that the flow law is associative.

1.3.2 Deviations from classical plasticity

Though many metals follow the von Mises (J_2 based) yield criterion and associative flow law, there are some that deviate from either or both. In this section, we present some instances where these deviations are observed. By doing so, we further emphasize the need for the proposed investigation.

Starting from the middle 1960s, experimental results were published which show that yield and flow stresses in tension and compression are different for some high strength steels (e.g.. Leslie and Sober [1967]; Kalish and Cohen [1969]; Rauch and Leslie [1972]; Chait [1972]; Spitzig et al [1975]). The physical mechanisms that can cause a SD were reviewed by Hirth and Cohen [1970] and Drucker [1973]. For an elastically isotropic material exhibiting SD, a yield function that only depends on J_2 will not give an accurate representation of the material behavior.

Experiments on iron single crystals (Spitzig [1979]) showed that contrary to Schmid's law (Schmid [1924]), the normal stress on the slip planes affects the dislocation interactions. The results suggest that the predominant effect of hydrostatic pressure is to retard the generation of mobile dislocations, resulting in an increase in dislocation density which in turn causes an increase in volume. This suggests that application of hydrostatic pressure affects inelastic behavior of the material, indicating that flow is dependent on I_1.

The above examples are a few instances where a J_2 based yield description falls short in representing the material behavior. Chapter 3 reviews more instances where a generalization of the yield function is needed.

1.3.3 Modified Yield Functions

Some researchers have extended J_2 plasticity theory to account for deviations from classical plasticity. Drucker [1949] compared Osgood's [1947] experimental data on aluminum alloy tubes to classical Tresca and von Mises yield criterion. While neither the Tresca criterion, nor the Mises criterion, agreed well with the experimental data, a function of the form

$$f(J_2, J_3) = J_2^3 - 2.25\ J_3^2 - 1, \tag{1.5}$$

did fit the data well. This was one of the first functions to go beyond the J_2 representation of yield for metallic materials.

For materials exhibiting SD, J_2 plasticity theory needs to be generalized. Yield functions for such materials must be represented by an odd power of I_1, an odd power of J_3, or a combination of the two. Dependence on I_1 requires pressure sensitivity, while dependence on J_3 (and not I_1) requires pressure insensitivity. Spitzig et al [1975] superimposed tensile and compressive loads on hydrostatic pressure for different materials. The results clearly showed that the flow stress is pressure dependent. In many cases, the flow stress appears to be linearly related to hydrostatic pressure, suggesting the use of a Drucker-Prager yield criterion (Drucker and Prager [1952]);

$$f = \alpha\ I_1 + \sqrt{J_2} - k \tag{1.6}$$

where α and k are experimentally determined constants. In other cases, the relationship was not truly linear suggesting that either a J_3 term or a different function of I_1 is required.

Spitzig et al [1975] had good success using a Drucker-Prager type yield criterion of the form:

$$\sqrt{3J_2} = c - a\ I_1 \tag{1.7}$$

where a and c are both strain dependent, but their ratio $a/c(= \alpha)$ is shown to be independent of strain. The SD predicted by equation 1.7 is simply $2a$.

Use of an associated flow law with a pressure dependent yield function results in a predicted permanent volume change approximately 15 times greater than that determined by pre-test and post-test density measurements and strain gage measurements (Spitzig et al [1975,1976]; Spitzig and Richmond [1980], Richmond and Spitzig [1984]). This suggests the use of a non-associated flow law with pressure dependent yield representations for these materials.

1.4 Method of Generalization

The generalization of classical plasticity theory lies in not ignoring the dependence of flow on the stress invariants I_1 and J_3. This necessarily complicates the mathematics and raises the issue of what functional form of the stress invariants best represents inelastic flow.

A general approach for determining the inelastic flow dependence on each of the three stress invariants would be to follow stress paths where only one of the three invariants varies. Two classical experiments that do this are: a hydrostatic pressure test, where only I_1 varies; and a pure torsion test, where only J_2 varies. There are many other stress paths that are possible. Unfortunately, these stress paths generally require three-dimensional stress states, which are difficult to obtain in the laboratory. For experimental expediency, tests involving axial-torsional loading of thin-walled tubes are to be used in determining the significance of the first and third stress invariants, I_1 and J_3, respectively.

Once the form of the threshold function is determined for IN718, characterization is done to quantify the material parameters in the model. Characterization experiments include shear tests and uniaxial (tensile and compressive) tests. Multiple combinations of stress invariants in the threshold function can result in an equally good correlation with the uniaxial test data. Experimental validation is required to help choose the proper combination of invariants. This is done by following load paths that extremize the differences between the predicted responses, based on the chosen threshold functions and by comparing the experiments with predictions. This approach can be applied to any material exhibiting a SD, e.g. martensitic steels, and intermetallics like titanium aluminide.

1.5 Overview

Various mechanisms of deformation in IN718 are discussed in Chapter 2. Also reviewed are the strengthening mechanisms in metallic alloys and the mechanisms responsible for SD in metals. By comparing and contrasting different mechanisms, an attempt is made to identify the ones that could be responsible for the observed SD effect in IN718.

Theoretical background, explaining the fundamentals of rate-independent and rate-dependent

plasticity with emphasis on metal plasticity, is presented in Chapter 3. Thermodynamic considerations leading to the use of internal state variables to account for various aspects of time dependent inelastic deformation are explained therein. Related work on various aspects of inelastic deformation, viz. yield and flow is also reviewed.

The viscoplastic model to be used for this investigation is proposed in Chapter 4. Starting with the proposed threshold function, the flow and evolution laws are derived. The requirement of convexity of the yield function is discussed. The experimental program for determination of the material parameters in the proposed model is discussed in Chapter 5. A brief review of experimental work in metal plasticity is followed by a description of the experimental setup to be used in the present research. Test matrices for characterization and validation experiments are developed.

Experimental results and the correlation between model and experiments are provided in Chapter 6. Six material parameter sets that fit the characterization data are presented. Choice of the right parameter set for Inconel 718 by correlating the predicted responses to biaxial validation tests and hydrostatic pressure tests is discussed in detail. This is followed by concluding remarks and suggested future work in Chapter 7.

Chapter 2

Microstructure and deformation Mechanisms

In this chapter, a detailed review of the microstructure and strengthening mechanisms in Inconel 718 is presented. Also documented are the mechanisms responsible for the SD effect in metallic materials in general. The effect of these mechanisms on the macroscopic behavior of metals is reviewed. Finally, by comparing and contrasting various mechanisms, an attempt is made to identify the ones responsible for the SD in Inconel 718.

Numerous structural studies on Inconel 718 have been carried out in an attempt to correlate its properties to microstructure and heat treatment. This alloy has a large number of phases that form in a specific temperature range and have a characteristic morphology. The following is a list of different phases that are formed during various stages of heat treatment:

1. *MC phase*: discrete particle phase formed on solidification and is stable up to 1200°C.
2. *Laves phase*: round, island shaped particles that form on solidification in the high-niobium areas and are stable up to 1175°C.
3. *δ phase*: needle-like/plate-like that form on cooling during solidification in high niobium areas and are stable up to 1010°C in wrought alloys, and up to 1120°C in cast alloys, precipitating from 840°C to 980°C.

Table 2.1: Material Composition of Inconel 718

Element	Content(wt.%)
Ni	53.58
Cr	17.52
Mo	2.87
(Nb+Ta)	5.19
Ti	0.95
Al	0.57
Co	0.39
C	0.034
S	0.002
Mn	0.12
Si	0.07
B	0.004
Cu	0.05
P	0.006
Fe	Bal.

4. γ'' *phase*: disc shaped precipitates form during cooling or heat treatment between 730°C and 900°C. During cooling these precipitates tend to become smaller.

5. γ' *phase*: spheroidal precipitates form when cooling or heat treatment is in the range, 720°C-620°C.

2.1 Microstructure of Inconel 718

Wrought Inconel 718 alloy was obtained in the form of extruded 31.8 mm bars, all from the same heat treatment. The weight composition of the alloy is listed in Table 2.1. The machined samples were solutioned at 1038°C in argon for one hour and then air cooled. Then they were aged at 720°C in argon for eight hours, cooled at 55°C/hour to 620°C and held for eight hours, then air cooled to room temperature.

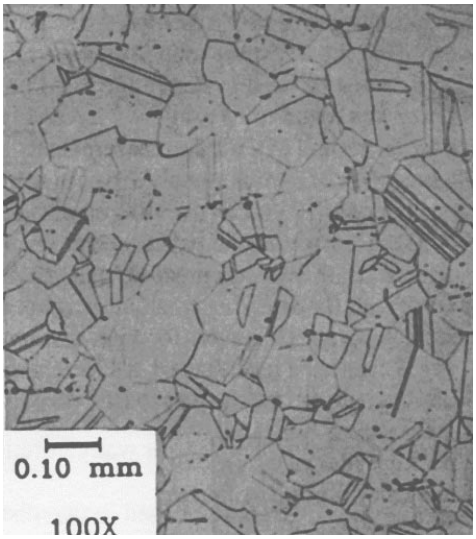

Figure 2.1: Optical Micrograph of aged Inconel 718

Gil et al [1999b] performed metallography on this alloy by polishing and etching using Tucker's reagent (45 ml HCl, 25 ml H_2O, 15 ml HNO_3, and 15 ml HF) to reveal the grain structure as seen in Figure 2.1. The grain structure consisted of equiaxed grains having an ASTM size of 4 (90 μm in diameter). Carbide particles were observed throughout the microstructure. Microhardness was measured to be Vicker 440 / Rockwell C of 45.

Transmission electron microscopy showed a fine dispersion of γ'' precipitates with preferred orientation within a particular grain. This is shown in Figure 2.2 (samples prepared by C. Gil, observed by P. Howell, Earth and Mineral Sciences, PSU). The precipitate particles were observed to be platelets approximately 10-15 nm in length. Texture analysis (by M. Angelone, Material Characterization Lab, PSU) showed that there is no preferred grain orientation. Thus the preferred orientation of the precipitates within the grain is not expected to cause anisotropic behavior.

2.2 Mechanisms of deformation in metals

This section reviews some of the physical mechanisms that occur during inelastic deformation in metallic materials. Strengthening mechanisms in aged Inconel 718 and the interaction between the applied stress and microstructure are discussed next.

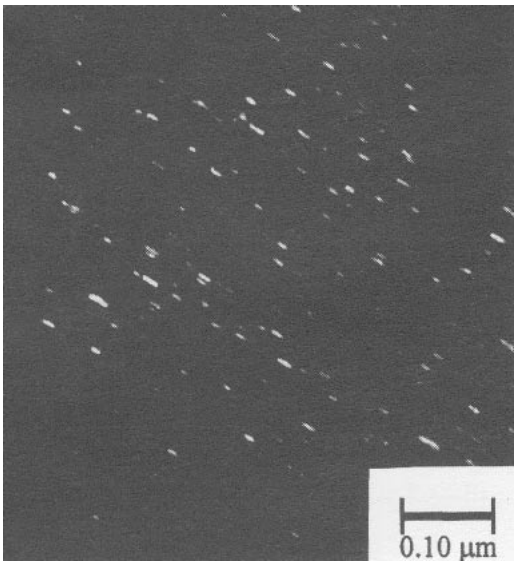

Figure 2.2: Transmission Electron Microscopy of aged Inconel 718 showing γ'' precipitates

At low temperature, slip is the most common mechanism of deformation. Slip occurs on the plane of highest atomic density in the direction closest to the planes of maximum shear stress. These planes and directions differ depending on the crystallographic structure of the metal and the direction of the applied load.

During inelastic deformation most materials exhibit a resistance to slip called strain hardening. Hardening occurs due to interaction of dislocations with precipitates, grain boundaries, or other dislocations and is often a manifestation of dislocation pileups. Dislocation interaction may result in internal stress, causing a resistance to further deformation. However, upon reversal of loading, the dislocations will propagate more easily and may cause yielding to occur at much lower applied stress level, resulting in the Bauschinger effect (Khan and Huang [1995]).

Another important factor that affects hardening behavior is the grain size. For a coarse grain material, slip is restricted to the grain boundaries. However, for a fine grain material like Inconel 718, slip systems are also activated in the interior of the grains causing higher dislocation interaction in the material. This results in higher strain hardening.

2.2.1 Strengthening mechanisms in Inconel 718

Generally, strengthening in metals is achieved by slowing the movement of dislocations. In a precipitate hardened material, the precipitates are dispersed throughout the grains. Dislocations are pinned at these precipitates causing dislocation pileups. In order to overcome the precipitates the dislocations either climb over or shear through them, both of which require additional shear stress.

Strengthening Phases

Paulonis et al [1969] showed that the major strengthening phase in aged Inconel 718 is the disc-shaped $\gamma''(DO_{22})$ precipitates rather than the spheroidal γ' (Ll_2) phase found in most nickel superalloys. The unit cells showing ordering for the body-centered tetragonal (bct) γ'' and the face-centered γ' are shown in Figure 2.3. They observed that fully heat treated and deformed samples of Inconel 718, both at room and elevated temperatures, exhibited planar deformation banding, a slip mode characteristic of nickel-based superalloys. They pointed out that the alloy exhibits good tensile strength between cryogenic temperature to about 705°C, even with as low as 20% by weight of the strengthening γ'' phase. Excellent weldability was attributed to sluggish precipitation kinetics of the γ'' phase. They found that the rapid deterioration of the tensile and creep strengths from 650-760°C was primarily due to rapid coarsening of the γ'' phase and partial solution of the γ' phases with concurrent formation of stable orthorhombic Ni_3Nb. Nevertheless, γ'' forms coherently and tends to remain so throughout the coarsening period. Coherency of the precipitate is a significant factor that contributes to the strength of the alloy.

Deformation Mechanisms

Analysis of deformed samples is difficult because the combination of high particle density, coherency strain contrast, and dislocation strain contrast results in extremely complicated electron micrographs (Paulonis et al [1969]). Compression at room temperature causes {1 1 1} planar slip banding. Tensile loading at elevated temperature results in heterogeneous slip which is confined to planar bands. Precipitate shearing within the slip bands is also

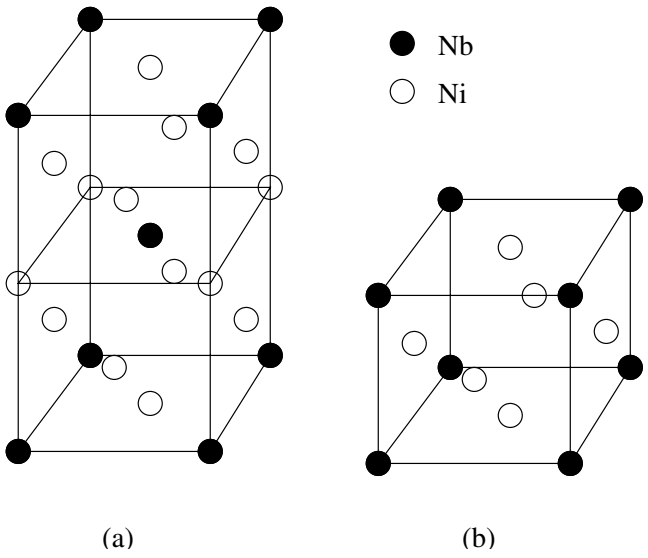

Figure 2.3: Unit cells showing ordering: (a) bct (γ'') structure (b) fcc (γ') structure

observed during tensile deformation.

Oblak et al [1974] observed that since γ'' particles produce a tetragonal distortion of the matrix, the specific variants of γ'' can be controlled by the application of stress during aging. To restore order in the DO_{22} phase, atoms have to displace differently in different directions. Also, dislocation movement to restore order in different variants of γ'' is different. Hence order strengthening is a complex interplay between the stress axis, Burgers vector of dislocations and the variant present in the microstructure. Aging the material under tensile and compressive loads suppresses or enhances the formation of a particular variant of DO_{22}. This results in a stronger material when aged under tensile load and a weaker material when aged under compressive load. This suggests that different variants of γ'' interact differently with the applied stress field and this could be a possible cause of the SD.

While no evidence was found for a stacking fault mode of shear, motion of dislocation pairs seemed to cause shear (Oblak et al [1974]). Smaller particle sizes result in dislocations being arranged in quadruplets rather than in pairs. While the lowest energy mode of deformation is the motion of dislocation quadruplets, the comparison with experimental data on increase in critical resolved shear stress (CRSS) points towards deformation by motion of dislocation pairs. For these reasons, it is felt that while order ensures the pairwise motion of dislocations, the principal obstacles to these pairs are not the ordered particles per se, but

rather their coherency strain fields. Hence, a coherency strengthening seems more probable than order strengthening. Also, the temperature dependence of CRSS is better predicted by coherency strengthening model. A possible role of the γ' phase may be to inhibit deformation by stacking fault mode of shear. Hence, extremely stable microstructures can be obtained by formation of compound γ''-γ' precipitate particles.

Small and Large Deformation Effects

Amongst other mechanisms in Inconel 718, the possibility of shearing ordered precipitates by deformation twinning is discussed by Sundararaman et al [1988] for room temperature deformation. Circular dislocation loops were found near γ' and a large number of dislocation pairs were found near γ'' phase in samples deformed to 2% strain. Some dislocations were observed to split up into partial dislocations on entering γ'' precipitates. Offset produced on γ'' particles due to the passage of the deformation bands indicates that these precipitate regions contain multi-layered stacking faults. Also observed were two sets of deformation bands, lying on two different {1 1 1} plane variants.

For large strains (19%), Sundararaman et al [1988] observed similar deformation bands in the material. In addition, the presence of deformation twins was seen within these bands. The flow stress required for deformation twinning is less than that required for precipitate bypassing and hence twinning is favored. Deformation of samples aged for longer periods resulting in coarser precipitates showed that the γ'' particles had apparently fragmented into slices along {1 1 1} planes. Deformation twinning of γ'' precipitates conserves order within the twin bands, hence the matrix-precipitate lattice correspondence for the twinned regions is the same as that for the twin-free regions. Some matrix twin segments appeared to propagate through a few γ'' precipitates. Offsets caused by the deformation twinning leads to rotation of the macroscopic γ'' habit plane. Each precipitate variant is associated with a favored twin-plane (of the type {1 1 1}), the selection of which is presumably dictated by the relative orientation of the stress axis. Again, deformation twinning is not seen in samples with very fine sized γ'' precipitates.

Work Hardening

The work hardening rate in precipitate hardened alloys generally increases abruptly as the precipitate size grows beyond a certain critical value (Sundararaman et al [1988]). This effect is attributed to the transition from precipitate shearing to the precipitate bypassing mechanism regime where the deformation results in the accumulation of dislocations in the vicinity of the non-deformable precipitates. In Inconel 718, however, a drop in the work hardening rate is observed when the precipitate radius is greater than 10 nm. This strongly suggests that precipitate bypassing mechanisms, like Orowan, are not active. The passage of shear through the precipitate particles by deformation twinning does not increase the dislocation density to any significant extent and consequently this deformation mechanism is not expected to increase the work hardening rate. The stress required to nucleate deformation twins in the precipitate particles is larger than that required for the growth of such twins. Thus, nucleation is immediately followed by easy propagation of deformation twins across the precipitates. This brings down the work hardening rate when precipitate size is greater than 10 nm.

Effect of Strain Rate and Temperature

The effect of strain rate and temperature on the thermo-mechanical behavior of Inconel 718 was investigated by Zhou et al [1993] to understand the relationships between the dynamic restoration process and the flow stress-strain curves. Also, changes of microstructure associated with different degrees of reduction during compression processing were investigated. Study of stress-strain response shows higher peak stresses at lower temperatures. The flow stress is mildly sensitive to strain rates between 0.1-0.05 sec^{-1}, but this sensitivity increases with temperature. Dynamic recovery and dynamic recrystallization are observed in the microstructure throughout the range of the experiments. Nucleation of dynamically recrystallized grains occurs at strains corresponding to peak stress (referred to as peak strain) and the dislocation density in the deformed region is considerable at this strain. The fraction of the recrystallized grains increases with temperature. Preferred nucleation sites for the recrystallized grains are the strained grain boundaries. Dynamic recovery is a slow process and hence the dislocation density can increase considerably before dynamic

recrystallization initiates at peak strain.

A critical dislocation density, which depends on the condition of deformation, must be exceeded before recrystallization can proceed. An increase in temperature leads to an increase in grain boundary mobility and a decrease in the critical dislocation density for dynamic recrystallization, which in turn results in a decrease in peak strain. The strain rate has the opposite effect. The fraction of dynamically recrystallized grains increases with temperature, and the fully recrystallized microstructure is obtained at temperatures greater than 1050°C and a strain of around 0.7. Beyond this peak strain, more dislocations are generated which is a driving force for further nucleation and grain growth.

2.2.2 Mechanisms Causing Strength Differential Effect

Several hypotheses were proposed to explain the strength differential (SD) effect. These include microcracking, residual stresses, internal Bauschinger effect, particle-dislocation interactions, and volume expansion during inelastic deformation. In this section a brief history of these investigations is presented. Comparing and correlating these with the deformation mechanisms in Inconel 718, an attempt can be made to qualitatively arrive at the most probable cause of the SD.

Volume Expansion Hypothesis

Leslie and Sober [1967] were among the first to observe SD in martensitic steels. They found that untempered carbon martensite is significantly stronger in compression than in tension. The SD effect appeared to increase with increasing carbon content. Radcliffe and Leslie [1969] were the first to attribute SD effect to volume expansion during inelastic deformation, which would theoretically lead to larger stress in compression than in tension. The volume expansion hypothesis is also supported by Drucker [1973] for plastics and granular media.

In some cases the effect of hydrostatic stress is to cause an increase in dislocation density, which can result in permanent volume expansion. However, some hydrostatic pressure dependent materials do not exhibit a permanent volume change during deformation. Spitzig et al [1975] have reported that the yield strength of quenched AISI 4310 and 4330 steels

increases evenly in both tension and compression with increasing hydrostatic pressure. Furthermore, they detected a permanent volume change proportional to inelastic strain. They suggested that the change in volume is due to a large increase in the dislocation density. Consequently, SD of 6% is observed for both steels, which remained constant with increase in inelastic strain and hydrostatic pressure. They proposed a modified yield function to account for this SD (see equation 3.43).

Precipitate Dislocation Interaction

Rauch [1975] speculated that a significant generation of dislocations would lead to a volume change, especially in aged materials where pre-existing dislocations are immobilized by precipitates. However, their experimental results for tempered AISI 4310, 4320 and 4330 steels disagree. No evidence of permanent volume expansion was observed. SD appeared to increase with decreasing temperature.

Rauch et al [1975] point out that though the initial density decrease (volume increase) in as-quenched AISI 4310, 4320, and 4330 steels can be attributed to transformation of retained austenite, the rate of density change continues to be high even at large strains. Thus SD at large strains can be better explained by increase in dislocation density during flow. According to them, the volume expansion hypothesis is a potential explanation for SD effect. Pinning of transformation dislocations by carbon and rapid mobilization of newly created dislocations result in volume increase during deformation. This is consistent with no SD effect in unaged maraging steels, which have no precipitates. All this points to hydrostatic stress dependence of yield and flow in martensitic steels.

Nonlinear Elastic Interaction Hypothesis

Another theory for the SD effect was proposed by Hirth and Cohen [1970]. They ruled out: (1) microcracks, because ultra fine grained martensitic steels have enhanced fracture toughness, are resistant to microcracking, and yet exhibit SD; (2) residual stresses, because at sufficiently high strains, residual stresses are overcome and yet the SD persists; (3) retained austenite; and (4) internal Bauschinger effect, because of randomness in the

orientation of the martensite plates. They attribute the SD effect to the solute-dislocation interaction. The barrier for the dislocation segments near an interstitial carbon atom is influenced by the normal stress across the glide plane that is increased by compression and decreased by tension. Severe distortion of the iron lattice around the interstitial carbon atom leads to local elastic strains that become non-linear. This inevitably alters the atomic force-displacement relationships such that they are different in tension and compression. This hypothesis suggests that a significant portion of the SD phenomenon may be due to nonlinear elastic interactions. They were able to account for a SD of up to 3-6% using this hypothesis in martensitic steels.

Kalish and Cohen [1969] suggest that displacement of iron atoms are so large that associated elastic strains are nonlinear and the interstitial-dislocation binding energy becomes greater in compression than in tension. Coherency strains around the precipitated particles result in greater dislocation interaction under compression than under tension. This suggestion is supported by Chait [1973], who tested three titanium alloys in the aged condition and found that coherent precipitation contributes to strength differential effect. Two of these alloys that exhibited large SD, possessed coherent $\alpha - \beta$ phase, while one alloy showed very small SD due to α phase in it being not coherent. Chait attributed the SD effect in Zircalloy to formation of deformation twins, which is more difficult in compression than in tension. Similar results in titanium alloys are reported by Winstone et al [1973]. The SD effect is much smaller in alloys in which the precipitates are not coherent with the matrix.

Pampillo et al [1972] add to the theory of Hirth and Cohen [1970] by suggesting that the nonlinear elastic behavior leads to a change in elastic moduli at sufficiently large elastic strains. The change occurs such that the elastic modulus decreases in tension and increases in compression. As a result, the internal stress, which depends on the interaction between the long range stress fields of the dislocations and that of the precipitates, decreases in tension and increases in compression, and this causes a SD. This theory explains the effect of carbon concentration and dislocation density for martensitic steels. Also, it explains the increase in SD at low temperatures. It is also consistent with the observation of Rauch and Leslie [1972], who reported that the elastic modulus of martensitic AISI 4320 steel was consistently 1-3.5% less in tension than in compression.

Gil et al [1999a] observed an increase in instantaneous stiffness of aged Inconel 718 in compression. They speculated that this *stiffening* could be associated with nonlinear interaction between precipitates and dislocations. However, stiffening was not observed in tension.

Effect of Interface Decohesion

Olsen and Ansell [1969] proposed a different theory for the SD effect in two phase alloys. TD-Nickel with 2% by volume dispersion of spherical ThO_2 particles tested at room temperature showed a 0.2% offset yield strength that was 30% higher in compression than in tension. The dislocations bypassed the ThO_2 particles both in tension and compression and hence is not the cause of SD. They suggested that voids form at the particle matrix interface as a result of interface decohesion during tensile loading prior to yielding. Interface decohesion prevents build-up of residual dislocation loops and high shear stress on particles, permitting a sufficient amount of dislocations to bow between particles to give macro yielding at lower stress level. This is not seen in compression. Thus, the mechanism in tension is bowing of dislocations and that in compression is shearing of precipitate particles, for which the required stress is greater and hence the SD.

This theory applies to two-phase alloys with a weak bond between the particles and the matrix. Olsen and Ansell [1969] also studied Al-Al_2O_3 which is known to exhibit very good bonding characteristics. Here, no decohesion was seen and this results in no SD. Contrary to this, Mannan and Rodriguez [1973] observed that the SD in zirconium alloy increased with increasing interstitial content, even though no decohesion was observed. Here, the SD is due to the differences in the long range internal stress. This supports our contention that the SD phenomenon is due to different mechanisms in different materials.

Stress Interaction with Precipitates

Plietsch and Ehrlich [1997] studied the strain-controlled tension/compression behavior of pseudoelastic shape memory alloys of Ni-Ti type. They proposed an explanation of SD based on the generation of stress induced martensite (SIM) during loading. For a given stress axis, the largest possible transformation strains in tension loading can be more than

twice as high as the respective compressive strains. They studied austenitic, pseudoelastic, and purely martensitic samples (pseudoelastic samples were obtained by special thermo-mechanical conditioning and are capable of completely recovering deformation strains up to 8% by reversible transformation). The austenitic samples showed no SD. In martensitic samples, martensite is present as 12 variants that are internally twinned. During tension or compression loading, these variants are altered by successive transformations to a single variant that is capable of compensating for the applied stress most effectively. The strain induced by martensitic transformation is much larger in tension than in compression for the same stress level. This results in a moderate SD. Pseudoelastic samples on the other hand, exhibited maximum SD. This is because the variant group formed in compression can deliver only a small transformation strain. This results in a much steeper rise in stress and results in a large SD.

2.3 Effect on Macroscopic Response

At this point, the strengthening mechanisms in aged Inconel 718 and other mechanisms that result in a SD effect in metals, are reviewed. It is required to relate these mechanisms to the macroscopic response (experimentally observable).

Drucker [1973] ruled out the possibility of microcracks or residual stresses being the cause for SD effect. According to him, it is the inhibiting influence of compression normal to the slip plane or twin plane which causes SD. Thus, it is most critical to verify whether or not the application of hydrostatic pressure (which adds equal compression normal to each plane) raises the magnitude of yield or flow strength in shear, tension or compression. For a material exhibiting a SD, a permanent volume change is a necessary accompaniment to inelastic deformation if the normality flow rule is applied. Generation of dislocations as well as vacancies in metals is associated with a volume increase and so might lead to similar macroscopic behavior. Stability at a material point implies convexity of the yield surface and for convexity to hold, the effect of added hydrostatic pressure on solid materials is limited by the theoretical strength. Drucker concludes that the most critical experiment to understand the SD is a tension test or a compression test in the presence of hydrostatic pressure.

The pressure dependency of flow results from the fact that the basic flow events like dislocation glide are pressure dependent (Spitzig [1979], Spitzig and Richmond [1984]). Spitzig [1979] showed that the normal stress on the slip planes affects the dislocation interactions in iron single crystals. The results suggest that hydrostatic pressure retards the generation of mobile dislocations. Jung [1981] presented a thermodynamics based model which shows that pressure should increase the interaction between dislocations. He used this model to explain dislocation annihilation and show that the pressure induced friction impedes dislocation motion and completely compensates for the increased interaction between dislocations. Spitzig and Richmond [1984] were able to directly relate equation 1.7 to Jung's model and conclude that the pressure dependence of the flow stress does not come from the plastic dilatancy as required by the associated flow law. Rather, it comes from the effect of pressure on dislocation motion.

Jesser and Kuhlmann-Wilsdorf [1972] found that the dislocation structure of commercially pure Nickel is not altered by hydrostatic pressure. They conclude that pressure causes a strong rise in frictional stress, which is associated with the Peierls-Nabarro stress being pressure dependent. They relate the pressure dependence to the extra volume that the atoms in the dislocation core occupy.

2.4 Possible mechanisms causing SD in Inconel 718

As mentioned earlier, microstructural analysis of deformed samples is difficult due to high particle density, coherency, and dislocation strain contrast. Thus, it is worthwhile to identify the possible mechanisms that cause SD in Inconel 718.

From the above discussion of SD, the experimental results on different materials suggest that a microstructure containing precipitate particles is a prerequisite for SD effect. The exact mechanism responsible for a SD differs depending on the microstructure of the material. Theories such as the internal Bauschinger effect and microcracking hypothesis, suggest that the SD will increase with increasing inelastic strain, which was not observed in experiments.

Interface decohesion between the γ'' precipitates and the matrix can be ruled out because the γ'' platelets remain coherent up to large strains and also during coarsening. Thus, this

is not the cause for a SD in aged Inconel 718. There is no significant difference between the elastic moduli in tension and compression. SD persists at strains beyond 2% where the inelastic strains are dominant and nonlinear elastic interactions are negligible. Thus, nonlinear elastic interaction is not the sole cause of SD. Gil et al [1999a], however, identified this mechanism as a cause for stiffening in compression, which occurs at the onset of yielding where the inelastic strains are low in comparison with the nonlinear elastic strains.

Differential formation of deformation twins in tension and compression does not seem to be a primary cause for a SD. The effect of loading on different variants of γ'' precipitate, which have different favored twin planes, can cause a difference in response under tension and compression. Though no definite evidence has been seen for or against this possibility, deformation twinning seems to be a secondary effect and is not likely to be a dominant cause for SD in Inconel 718.

Two theories that seem more convincing are: (1) volume expansion hypothesis; and (2) the particle-dislocation interaction hypothesis. In most cases, both of these underestimate the observed SD effect, suggesting that both of these mechanisms contribute to this effect. It remains to be seen whether hydrostatic pressure has an influence on the SD in Inconel 718. As suggested by Drucker, tensile and compressive experiments under varying hydrostatic pressure are planned on aged Inconel 718. In general, hydrostatic pressure impedes the motion of dislocations causing an increase in dislocation density which in turn causes a volume expansion.

In the event of hydrostatic pressure-independence, the most probable cause for SD in aged Inconel 718 appears to the interaction between coherency strain fields around the γ'' precipitates and the dislocations. It appears that the precipitate-dislocation interaction causes an increase in the dislocation density, the coherency strains seem to cause greater dislocation interaction under compression than under tension. If the material is hydrostatic pressure-dependent, the SD can be attributed in part to the particle-dislocation interaction and in part to the volume expansion.

Chapter 3

Continuum Plasticity

Starting with the definitions of stress invariants, this chapter presents the basic elements of rate-independent (classical) plasticity theory, viz. yield criterion, flow law, hardening law, and loading criteria. Then, the internal variable approach to rate-dependent plasticity is presented which leads into the internal variable theory of viscoplasticity. Finally, a review of general yield functions and flow laws that go beyond classical plasticity theory, is provided.

Any material deforms when subjected to external forces. The deformation is *elastic* if it is reversible and time-independent, *viscoelastic* if it is reversible and time-dependent, and *plastic* if it is irreversible or permanent. Brittle materials like glass and concrete exhibit very little inelastic deformation before fracturing. On the other hand, metals can undergo significant inelastic deformation before failure and therefore are ductile materials.

The theory of plasticity deals with the stress-strain and load-deformation relationships for a ductile material beyond the elastic limit. The establishment of these relationships generally follows two steps: (1) the experimental observation and (2) the mathematical representation. The stress states that are normally achieved in an experiment are uniform, but the ultimate goal of any plasticity theory is a general mathematical formulation that can predict the inelastic deformation of materials under complex loads.

The theories of plasticity can be established in two categories: (1) *mathematical theories* and (2) *physical theories*. Mathematical theories are formulated to represent the experimental

observations as general mathematical formulations. These theories do not require deep knowledge of physics of plastic deformation and are based on hypotheses and assumptions from experimental results. Therefore, the mathematical theories are referred to as *phenomenological* theories. The physical theories on the other hand, attempt to quantify the plastic deformation at the microscopic level and explain why and how the plastic deformation occurs. The movements of atoms and the deformation of single crystals and grains are important considerations. Here, metals are viewed as aggregates of single crystals or polycrystals and their response to applied loads are derived from their building blocks, namely single crystals and grains (Khan and Huang [1995]).

Most applications, such as metal forming or structural design, are based on macroscopic quantities. Any plasticity theory must therefore contain mathematical variables that can be measured during experiments at the macroscopic level. To make reasonable hypotheses and assumptions on the basis of experiments and to fully understand the meaning and limitations of a proposed theory, knowledge of material structure and physics of inelastic deformation is very helpful.

3.1 Invariants of the stress tensor

The stress state at any material point may be represented by the stress tensor σ_{ij}. Its components in the cartesian coordinate system can be represented by a matrix of second order

$$\sigma_{ij} = \begin{bmatrix} \sigma_{xx} & \sigma_{xy} & \sigma_{xz} \\ \sigma_{yx} & \sigma_{yy} & \sigma_{yz} \\ \sigma_{zx} & \sigma_{zy} & \sigma_{zz} \end{bmatrix}. \tag{3.1}$$

Since the stress tensor is symmetric, only six stress components $\sigma_{xx}, \sigma_{xy}, \sigma_{xz}, \sigma_{yy}, \sigma_{yz}, \sigma_{zz}$ are independent. Thus, six independent stress components determine a stress state uniquely and visa versa. Using the above stress tensor, the three principal stresses can be determined using the characteristic equation

$$|\sigma_{ij} - \sigma\delta_{ij}| = 0 \tag{3.2}$$

which can be expanded to

$$\sigma^3 - I_1\sigma^2 + I_2\sigma - I_3 = 0 \tag{3.3}$$

where δ_{ij} is the Kronecker delta, I_1, I_2, and I_3 are the invariants of the stress tensor. In terms of the principal stresses, σ_1, σ_2 and σ_3, the invariants are

$$\begin{aligned} I_1 &= \sigma_1 + \sigma_2 + \sigma_3 \\ I_2 &= \sigma_1\sigma_2 + \sigma_2\sigma_3 + \sigma_3\sigma_1 \\ I_3 &= \sigma_1\sigma_2\sigma_3. \end{aligned} \tag{3.4}$$

In plasticity theory, it is customary to decompose the stress tensor as

$$\sigma_{ij} = \sigma_m\delta_{ij} + S_{ij} \tag{3.5}$$

where σ_m is the hydrostatic stress given by

$$\sigma_m = \frac{1}{3}\sigma_{ii} = \frac{1}{3}(\sigma_{xx} + \sigma_{yy} + \sigma_{zz}) = \frac{1}{3}(\sigma_1 + \sigma_2 + \sigma_3) \tag{3.6}$$

and S_{ij} is the deviatoric stress tensor. Using the deviatoric stress tensor, the deviatoric stress invariants can be defined as

$$\begin{aligned} J_1 &= S_{ii} = 0 \\ J_2 &= \frac{1}{2}S_{ij}S_{ij} = \frac{1}{6}[(\sigma_1 - \sigma_2)^2 + (\sigma_2 - \sigma_3)^2 + (\sigma_3 - \sigma_1)^2] \\ J_3 &= \frac{1}{3}S_{ij}S_{jk}S_{ki} = S_1S_2S_3. \end{aligned} \tag{3.7}$$

The three invariants, I_1, J_2 and J_3 were discussed in Chapter 1. Invariants of the effective stress which are used in the proposed model are defined in a similar manner (Chapter 4).

3.2 Rate Independent Plasticity

In this section, the fundamental aspects of classical or rate-independent plasticity are explained. The three basic elements of classical plasticity are yield criterion, flow rule and hardening rule.

3.2.1 Yield Criteria

In a uniaxial stress state, the elastic limit is defined by the yield stress. Under combined stresses, the elastic limit is defined by a surface in stress space. Mathematically, the elastic limit, for a general anisotropic material is expressed as

$$f(\sigma_{ij}) = 0. \tag{3.8}$$

Invariant representation of yield

For an isotropic material, the orientation of principal axes is immaterial and hence the principal stresses, σ_1, σ_2 and σ_3 are sufficient to uniquely describe the state of stress. The principal stresses form the integrity basis (Spencer and Rivlin [1962]). It is customary to use I_1, J_2, and J_3 as an integrity basis. Hence, the yield function becomes

$$f(I_1, J_2, J_3) = 0. \tag{3.9}$$

As a further refinement to this criterion, evolution of material state can be incorporated in the integrity basis to represent the flow behavior.

Pressure independent yield criteria

Since yielding of most metals is found to be insensitive to hydrostatic pressure, it follows that shear stresses must control the yielding of such materials. There are several shear stress based yield criteria. Traditionally, Tresca and von Mises criteria are widely used for defining yield in metals.

1. **Tresca Yield Criterion** states that yielding occurs at a material point, when the maximum shearing stress at that point reaches a critical value k. In three dimensional principal stress space, the yield surface is a regular hexagonal cylinder with its axis along the hydrostatic stress axis.

2. **von Mises Yield Criterion** states that yielding occurs when the strain energy of distortion in a material reaches a critical value. In three dimensional principal stress

space, the yield surface is an infinite circular cylinder with its axis aligned with the hydrostatic stress axis.

The Tresca and Mises yield functions are independent of: I_1, implying hydrostatic pressure-independence; and J_3, meaning no asymmetry between tensile and compressive stresses (no SD).

Pressure-dependent yield criteria

Geological materials such as soils, rocks and concrete are hydrostatic pressure sensitive. Hence, their yield representation must involve I_1. Some metallic materials are also pressure sensitive and require a different yield representation compared to the conventional Tresca or Mises criterion (Drucker [1973], Spitzig [1975]). The simplest and most popular two-parameter models are those of Mohr-Coulomb and Drucker-Prager.

Mohr-Coulomb Criterion

Mohr's criterion is based on the assumption that the maximum shear stress is the decisive measure of yielding. It states that yielding occurs when the radius of the largest principal circle touches the yield envelope, which are straight lines in the (σ, τ) space as shown in Figure 3.1. Mathematically, this can be expressed as

$$|\tau| = c - \sigma \ tan\phi \tag{3.10}$$

in which c is the *cohesion* and ϕ is the *angle of internal friction*; both are material constants determined by experiments. In special cases of frictionless materials, for which $\phi = 0$, equation 3.10 reduces to the Tresca criterion. In terms of the stress invariants, the criterion can be written as

$$f(I_1, J_2, \theta) = \frac{1}{3} I_1 sin\phi + \sqrt{J_2}[sin(\theta + \frac{\pi}{3}) + \frac{1}{\sqrt{3}} cos(\theta + \frac{\pi}{3}) sin\phi] - c \ cos\phi \ = 0 \tag{3.11}$$

where θ depends on J_2 and J_3 as

$$cos(3\theta) = \frac{3\sqrt{3}}{2} \frac{J_3}{J_2^{\frac{3}{2}}}.$$

Graphically, this criterion is shown in different stress planes in Figure 3.1.

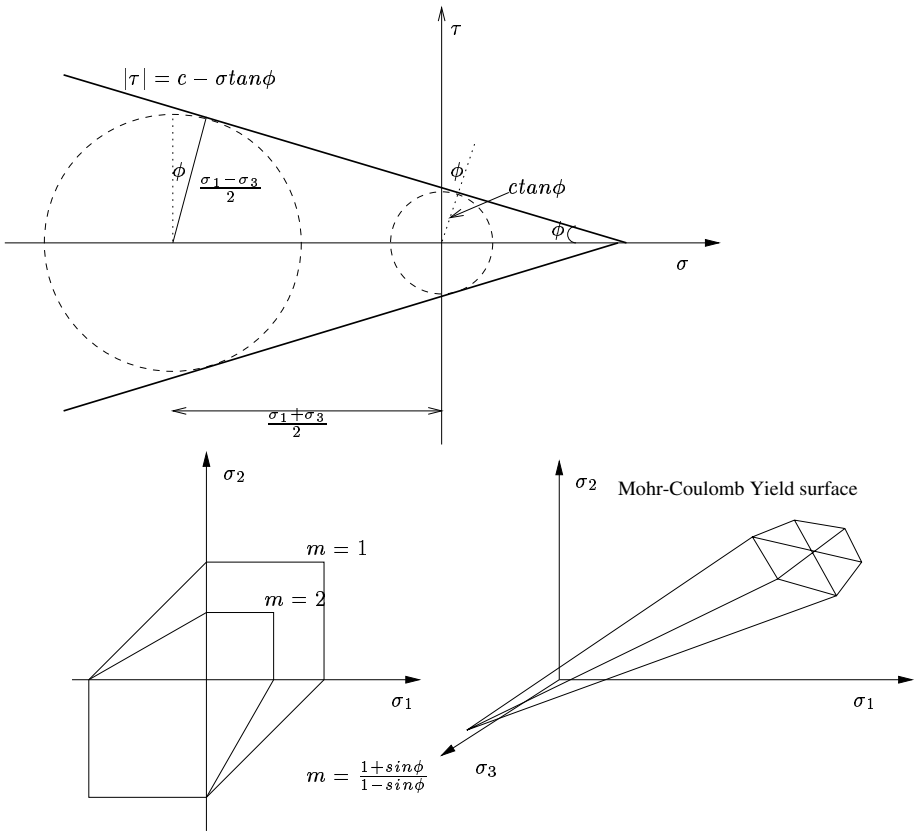

Figure 3.1: The Mohr-Coulomb Yield Criterion

Drucker-Prager Criterion

The Drucker-Prager criterion is a simple modification of the von Mises criterion to include the effect of hydrostatic pressure on yielding. Mathematically,

$$f(I_1, J_2) = \alpha I_1 + \sqrt{J_2} - k = 0 \tag{3.12}$$

where α and k are material constants. When α is zero, it reduces to the von Mises criterion. The yield surface here, is a right circular cone in the principal stress space, as shown in Figure 3.2.

Unlike the Mohr-Coulomb hexagonal yield surface, the Drucker-Prager surface is smooth. This facilitates its application in plasticity theory because it becomes easy to calculate the normal vector to the yield surface numerically.

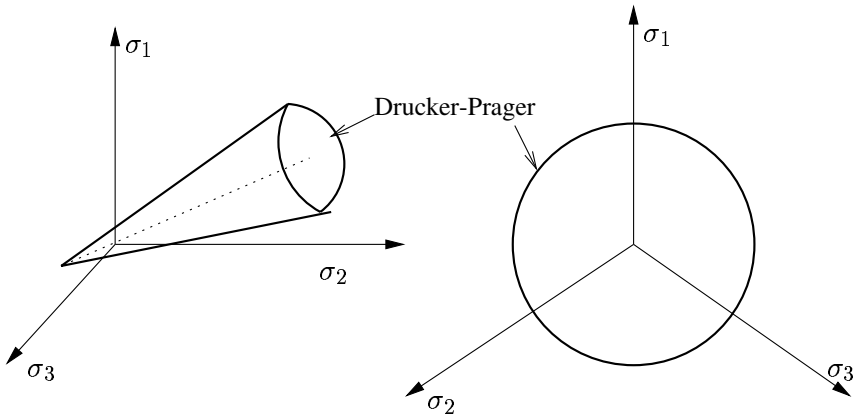

Figure 3.2: The Drucker-Prager Yield Criterion

3.2.2 Flow Law

Plastic Potential Theory

The general mathematical treatment of the constitutive equation for plastic deformation was proposed by von Mises in 1928. He noticed that in elasticity theory, the strain tensor was related to the stress through an elastic potential function, the complementary strain energy U_c such that

$$\epsilon_{ij} = \frac{\partial U_c}{\partial \sigma_{ij}}. \tag{3.13}$$

By generalizing and applying this idea to plasticity theory, Mises proposed that there exists a plastic potential $g(\sigma_{ij})$, such that the inelastic strain rate $\dot{\epsilon}^I_{ij}$ could be derived from the following flow rule:

$$\dot{\epsilon}^I_{ij} = \dot{\lambda}\frac{\partial g}{\partial \sigma_{ij}} \tag{3.14}$$

where $\dot{\lambda}$ is a proportional positive scalar factor which can be determined from the yield criterion. Plasticity theory based on the above flow rule is called *plastic potential theory.* The following remarks should be noted about the above flow rule:

1. Geometrically, the plastic potential $g(\sigma_{ij}) = 0$, represents a surface in the stress space and $\dot{\epsilon}^I_{ij}$ can be represented by a vector in this space. The inelastic strain rate vector is normal to $g(\sigma_{ij}) = 0$. Therefore, equation 3.14 is also referred to as the normality flow rule in plasticity theory.

2. If inelastic flow is hydrostatic pressure independent, and thus incompressible, the corresponding plastic potential surface in the principal stress space must be cylindrical (not necessarily with a circular cross section) with $\sigma_1 = \sigma_2 = \sigma_3$ as its axis. $\dot{\epsilon}^I_{ij}$ is perpendicular to this axis representing only shape changes of the surface. This is not the case for hydrostatic pressure-dependent materials.

3. A common approach in plasticity theory is to assume that the plastic potential function $g(\sigma_{ij})$ is the same as the yield function $f(\sigma_{ij})$, so that the flow law can be written as

$$\dot{\epsilon}^I_{ij} = \dot{\lambda}\frac{\partial f}{\partial \sigma_{ij}} \tag{3.15}$$

and the inelastic strain rate vector is normal to the yield surface. This is called the *associated flow rule*. On the other hand, if $g \neq f$, the flow rule is called *nonassociated*.

4. In general, experimental observations show that inelastic deformation of metals can be characterized quite well by an associated flow rule, but for some porous materials a nonassociated flow rule provides a better representation of inelastic deformation.

Prandtl-Reuss Incremental Stress-Strain Relations

The Prandtl-Reuss flow theory is based on the following three assumptions:

1. The principal axes of the inelastic strain increment are coincident with those of the current stresses.

2. The inelastic strain increments are proportional to the deviatoric stress tensor.

3. No volume change occurs during inelastic deformation.

4. Initial response is isotropic.

In contrast to the deformation theory, the stress-strain relation in the flow theory is given in an incremental form. Here, the inelastic (deviatoric) strain increments are given by

$$d\epsilon^I_{ij} = d\lambda\ S_{ij} \tag{3.16}$$

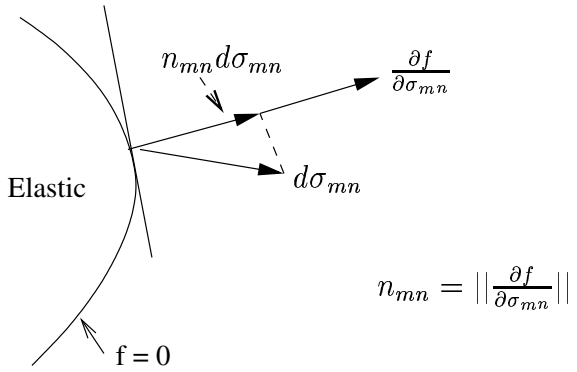

Figure 3.3: Graphical Representation of Flow Rule

where $d\lambda$ is a positive scalar factor. This relation is called the *Prandtl-Reuss relation.* An interesting observation is that the associated flow law for the Mises yield function is the Prandtl-Reuss relation. This means that the Prandtl-Reuss relations are associated with the Mises yield criterion. The flow rule is graphically shown in Figure 3.3.

Subsequent Yield Surface

For an elastic-perfectly plastic material, the subsequent yield surface is the same as the initial yield surface since there is no increase in stress carrying capacity of the material beyond the yield stress. But, for hardening materials, the two surfaces are different and there are various models to describe how the initial surface evolves into the subsequent yield surface. Before discussing these models, the criteria for loading and unloading should be defined.

Loading criteria

For a hardening material, if the stress state tends to move out of the yield surface, we have a *loading* process and elastic-plastic deformation is observed. Additional plastic strains are produced and the configuration of the current yield or loading surface changes, so that the stress state always stays on the subsequent loading surface. If the stress state tends to move into the yield surface, we have an *unloading* process. Only elastic deformation occurs and the loading surface remains unchanged. The other possibility of stress change from a plastic

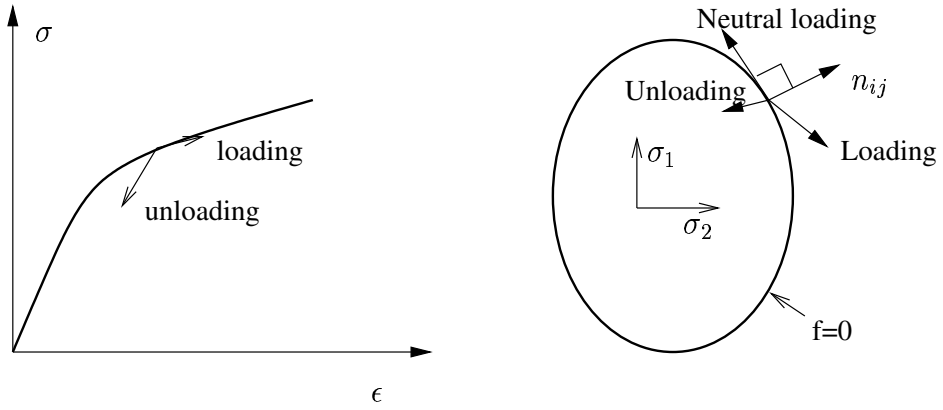

Figure 3.4: Loading Criterion for a Work-Hardening Material

state is that the stress point moves along the current yield surface. This process is called *neutral loading*. Mathematical expressions for classifying these criteria are called *loading criteria*, and may be expressed by:

$$\begin{aligned} f &= 0\ ,\ \frac{\partial f}{\partial \sigma_{ij}} d\sigma_{ij} > 0 \ :\ Loading \\ f &= 0\ ,\ \frac{\partial f}{\partial \sigma_{ij}} d\sigma_{ij} = 0 \ :\ Neutral\ loading \\ f &= 0\ ,\ \frac{\partial f}{\partial \sigma_{ij}} d\sigma_{ij} < 0 \ :\ Unloading. \end{aligned} \tag{3.17}$$

The gradient vector, $n_{ij}(=\partial f/\partial \sigma_{ij})$ is the outward normal to the yield surface $f = 0$. These criteria are illustrated schematically in Figure 3.4.

Consistency Condition

During inelastic deformation, the elastic region has to change so that the stress state remains on the yield surface. Mathematically, this condition is expressed as

$$f(\sigma + d\sigma, \kappa + d\kappa) = 0 \tag{3.18}$$

where κ is the hardening parameter. In incremental form, it may be rewritten as

$$\frac{\partial f}{\partial \sigma} d\sigma + \frac{\partial f}{\partial \kappa} d\kappa = 0. \tag{3.19}$$

This equation is known as the *consistency condition*, and lends itself to the determination of the magnitude of plastic strain increment. The consistency condition ensures that the

plastic loading path begins at the current yield surface and ends at the subsequent surface, and that changes in the size and location of the yield surface are consistent with the adopted hardening rule.

Hardening Laws in Plasticity

For work hardening materials, stress states can exist beyond the initial yield surface and the yield surface evolves such that the current stress state always lies on it. There are various models describing this evolution of the yield surface. These are called hardening models.

Isotropic Hardening

This is the simplest hardening model and is based on the assumption that the yield surface expands uniformly without distortion, as the inelastic flow occurs, as shown in Figure 3.5(a). If the yield surface has the form $f(\sigma_{ij}) = k^2(\epsilon_p)$, the size of the yield surface is governed by the value of k^2, which depends upon either effective inelastic strain or plastic work. Isotropic hardening can be observed in materials with forest dislocations.

Since the loading surface expands uniformly(or isotropically), it can not account for the Bauschinger effect exhibited by most structural metals. Hence, it will not lead to realistic results when complex loading paths involving significant changes in the direction of stress vector are considered.

Kinematic Hardening

The kinematic hardening model assumes that during inelastic deformation the yield surface translates as a rigid body in the stress space, keeping its shape, size, and orientation the same as that of the initial yield surface. Kinematic hardening is often associated with dislocation pileups in a material. This model has the form

$$f(\sigma_{ij} - \overline{\alpha}_{ij}) - k^2 \;=\; 0 \tag{3.20}$$

where k is a constant and $\overline{\alpha}_{ij}$ are the coordinates of the center of the yield surface, which changes as inelastic deformation progresses. This is shown graphically in Figure 3.5(b).

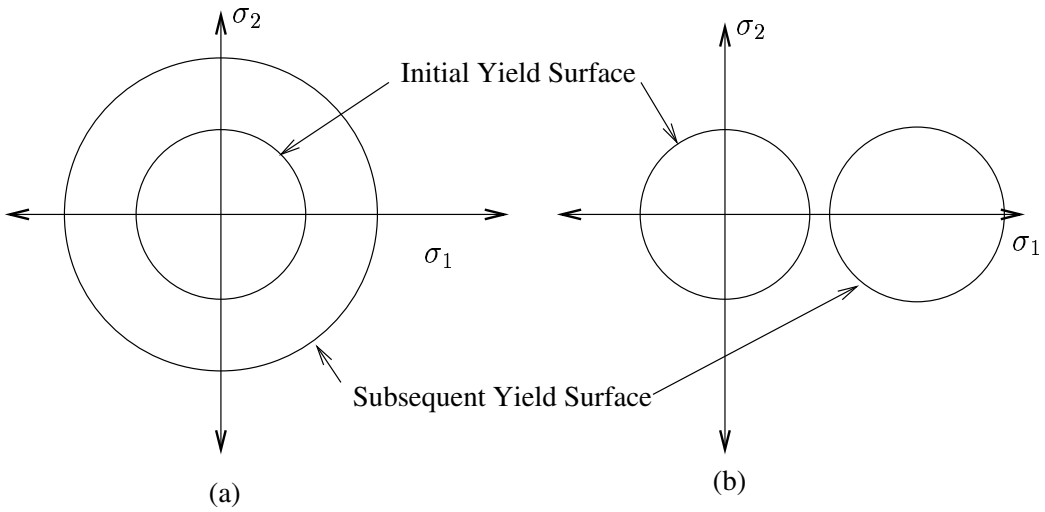

Figure 3.5: Hardening Rules: (a)Isotropic; (b)Kinematic

Mixed Hardening

A combination of isotropic and kinematic models leads to a more realistic *mixed hardening model* whose loading function can be expressed as

$$f(\sigma_{ij} - \overline{\alpha}_{ij}) - k^2(\epsilon_p) = 0. \tag{3.21}$$

In engineering application for metals, the concept of mixed hardening is attractive. The loading surface translates and uniformly expands in all directions; i.e. it retains its original shape. With mixed hardening, different levels of Bauschinger effect can be simulated.

Drucker's Stability Postulate

Drucker [1959] defined a stable material as one which satisfies the following conditions:

1. The work done by an external agency during the application of an added set of forces on the change in displacement it produces, is positive.

2. The net work performed by the external agency over the cycle of application and removal of the added set of forces on the changes in displacements it produces is nonnegative.

These criteria are called *Drucker's Stability postulate.* The first is for a work increment during loading and is called *stability in small* and the second is for a work increment after full load/unload cycle, and is termed *stability in cycle.* Mathematically, these reduce to

$$d\sigma d\epsilon \;>\; 0 \quad \textit{loading}; \tag{3.22}$$

$$d\sigma d\epsilon^I \;\geq\; 0 \quad \textit{complete cycle.} \tag{3.23}$$

Stability in a complete cycle leads to the following:

$$(\sigma_{ij} - \sigma^*_{ij})\dot{\epsilon}^I_{ij} \;\geq\; 0 \tag{3.24}$$

where σ_{ij} is a stress state on the yield surface and σ^*_{ij} is any possible stress state inside or on the yield surface. This is called *maximum plastic dissipation postulate.*

Convexity and Normality

If the plastic strain coordinates are superimposed upon the stress coordinates, as shown in Figure 3.6, equation 3.24 can be interpreted geometrically as the scalar product of the stress increment vector $(\sigma_{ij} - \sigma^*_{ij})$ with the strain increment vector $d\epsilon^I_{ij}$. A positive scalar product indicates an acute angle between these two vectors. The stability postulate therefore leads

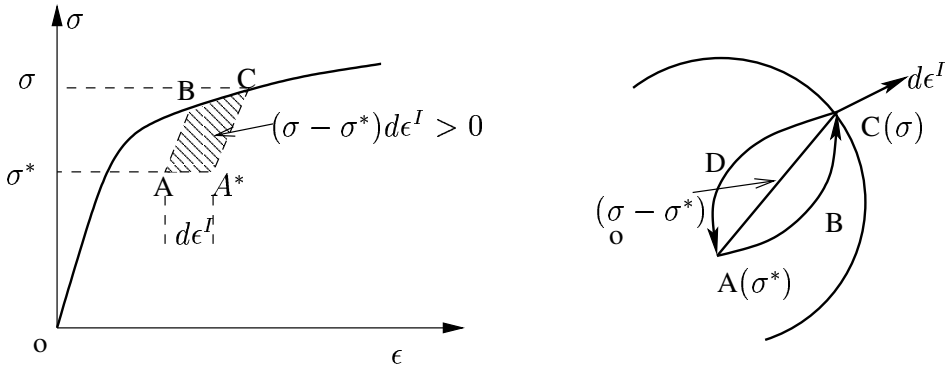

Figure 3.6: Stability in Cycle: Stress Path ABC produced by External Agency

to the following consequences for work hardening materials (Drucker [1960]):

1. Convexity: The initial yield surface and all the subsequent yield surfaces must be convex.

2. Normality: The inelastic strain increment vector, $d\epsilon_{ij}^I$ must be normal to the yield surface at a smooth point and must lie between adjacent normals at a corner.

3.3 Rate Dependent Plasticity

One way that loading history affects the constitutive relation is through *rate sensitivity*; the deformation produced by a slow loading rate is different, almost invariably greater than that produced by rapid stressing. A particular manifestation of the time dependence is the fact that the deformation will in general, increase in time at a constant stress; called *creep*. *Relaxation*, on the other hand is the decrease in stress with time for a given strain.

Many physical and chemical processes in metals are thermally activated and hence the dependence of material behavior on temperature. For most metals, creep is thermally activated if the temperature is higher than 30% of the melting temperature. Creep can cause failure, either due to excessive deformation or creep rupture. These processes are often governed by the *Arrhenius rate equation*, which has a general form

$$\dot{\epsilon}_{ss} \;=\; A\; e^{\triangle E/kT} \tag{3.25}$$

where $\dot{\epsilon}_{ss}$ is the steady state creep rate, $\triangle E$ is the activation energy, k is *Boltzmann's constant* and T is the absolute temperature. The rate sensitivity of a work-hardening material itself increases with temperature. The above equation permits, in principle, the simultaneous representation of the rate sensitivity and the temperature sensitivity of metallic materials.

An alternative way of representing the dependence of material response on temperature and rate is by assuming that the strain, in addition to stress and temperature, depends on an array of variables, α_β. These variables are called *internal*, or hidden variables, that usually take on scalar or second rank tensor values. The strain is accordingly given by

$$\epsilon = \epsilon(\sigma_{ij}, T, \alpha_\beta). \tag{3.26}$$

Another important effect observed in metals is creep which depends on stress level and temperature. Rate independent plasticity does not represent these effects. This section

starts with general principles in mechanics that lead to the internal variable theory of plasticity.

3.3.1 General Principles in Mechanics

Before we discuss the internal variables approach, it is necessary to lay out the universal laws that must be obeyed during any process, regardless of the properties of the material which is undergoing the process. There are five such principles to be considered in plasticity theory (Khan and Huang [1995]).

Conservation of Mass

According to the law of *conservation of mass*, no mass can be created or destroyed in a given volume v of the material, which leads to

$$\rho \, dv \;=\; constant \tag{3.27}$$

where ρ is the material density.

Conservation of Momentum

The rate of change of total momentum of any given set of particles equals the vectorial sum of all the forces acting on this set of particles. For a set of particles that currently occupies a spatial volume, v, with surface traction and the body forces acting on it, this law leads to

$$\sigma_{ij,j} \;+\; \rho b_i \;=\; \rho a_i \tag{3.28}$$

where b_i's are the body forces per unit volume and a_i's are the components of the acceleration of the body. Equations 3.28 are also known as the *local equations of equilibrium.*

Conservation of Angular Momentum

This principle is also a generalization of Newton's second law of motion for continuum mechanics. It states that the rate of change of moment of momentum for any given set

of particles equals the vectorial sum of the moments acting on it. Mathematically, the principle of *conservation of angular momentum* can be stated as

$$\int_v (\rho\ e_{ijk}\ r_j\ a_k) dv\ =\ \int_R (e_{ijk}\ r_j\ t_k) ds\ +\ \int_v (\rho\ e_{ijk}\ r_j\ b_k) dv \tag{3.29}$$

where e_{ijk} is the alternator, t_i is the traction force vector and r_i is the position vector of the body (volume v enclosed by surface R) under consideration. This, along with equation 3.28, establishes the symmetry of the stress tensor. i.e. $\sigma_{ij} = \sigma_{ji}$.

Conservation of Energy: The First Law of Thermodynamics

Extensive experimental observations indicate that energy can never be created or destroyed in the universe, but can only be transformed from one form to another. For a closed system the total rate of work done on the system by all the external agencies must equal the rate of increase of the total energy of the system. This principle is also called the *first law of thermodynamics*. If we consider only mechanical and thermal energy in a closed system, the first law can be written as

$$\rho \dot{u}\ =\ \sigma_{ij} \dot{\epsilon}_{ij}\ +\ \rho r\ -\ q_{i,i} \tag{3.30}$$

where $\dot{u}$ is the internal energy per unit volume, r is the internal heat source per unit volume, $q_{i,i}$ is the heat flux out of the system through its boundaries, and $\sigma_{ij} \dot{\epsilon}_{ij}$ represents the mechanical work done by the external forces that is not converted into kinetic energy.

Clausius-Duhem Inequality: The second Law of Thermodynamics

The *second law of thermodynamics* limits the direction of the energy transformation. Whenever a transformation occurs, the energies involved must obey the first law. It has been experimentally observed that while some energies transform from one type to another, there are other types of transformations that are impossible. For example, heat flow can occur from a warmer system to a colder system, but the reverse heat flow can never occur. The kinetic energy of a moving body can be converted into heat by friction, but the heat caused by friction can never be converted into kinetic energy. While the first law cannot describe these observations, it is the second law that governs this directional phenomenon observed in the energy transformation processes.

The second law postulates that there exists a state function called the entropy; the change in entropy is given by

$$\triangle S = S_2 - S_1 = \int_1^2 \frac{dQ}{T} \qquad \text{for a reversible process}$$

$$\triangle S = S_2 - S_1 > \int_1^2 \frac{dQ}{T} \qquad \text{for an irreversible process}$$

where dQ is the heat input during the process, T the temperature, and indices 1 and 2 denote the starting and ending points of the process. It can be seen that the change in entropy of a system can never be negative; it is zero for a reversible process and positive for an irreversible process. If only mechanical and thermal energies are considered, the second law can be written as

$$\rho \dot{s} - \rho \frac{r}{T} + \left(\frac{q_i}{T}\right)_{,i} \geq 0 \tag{3.31}$$

where s is the specific entropy. This relation is called *Clausius-Duhem inequality*. Using equation 3.30, r can be eliminated and we get

$$\rho T \dot{s} - \rho \dot{u} + \sigma_{ij} \dot{\epsilon_{ij}} - \frac{1}{T} q_i T_{,i} \geq 0. \tag{3.32}$$

By introducing a thermodynamic potential H, called the *Helmholtz free energy*, given by $H = u - sT$, we can rewrite equation 3.32 as

$$-\rho \dot{H} - \rho s \dot{T} + \sigma_{ij} \dot{\epsilon_{ij}} - \frac{1}{T} q_i T_{,i} \geq 0. \tag{3.33}$$

In thermodynamics, the internal energy u, entropy s, heat flux q and the stress σ are all considered state functions that can be determined by the state variables using *state equations* or *constitutive equations*.

3.3.2 Internal Variables: General Theory

In thermoelasticity, internal energy u, entropy s, and heat flux q, can be fully described by the current value of stress and temperature. The situation becomes more complex when deformation is inelastic. Here, in addition to the current values of the state variables, the history of the deformation is also important. This requires identifying more state variables to describe the deformation history. It is very hard to enumerate all of the relevant state

variables from macroscopic observations alone. Microscopic deformation considerations are needed and some assumptions have to be made to use certain macroscopic (observable) variables as representatives of the microscopic phenomenon. After the state variables are chosen, the mathematical forms of the constitutive equations should be determined. This involves experimental evaluation and mathematical formalization, which at times are very complex (Lubliner [1990]).

In thermomechanics, the state variables are identified by using the concept of *internal* variables. It is postulated that the current state of an inelastically deformed solid can be determined by the current values of stress, temperature, and a set of internal variables. The history of deformation is indirectly included in the evolution of these internal variables. Mathematically, this can be stated as

$$\begin{aligned} u &= u(\sigma_{ij}, T, \alpha_\beta) \\ s &= s(\sigma_{ij}, T, \alpha_\beta) \\ q &= q(\sigma_{ij}, T, \alpha_\beta) \end{aligned} \tag{3.34}$$

where α_β, i=1,2,...,n are internal variables which can be scalars, vectors or tensors. These variables can be considered in two categories; (1) *physical* variables describing the aspects of local physico-chemical structure which may change spontaneously, and (2) mathematical constructs or *phenomenological variables*, in which case the functional dependence of stress(or strain) on the internal variables, and their rate equations, is assumed a-priori.

Thermomechanical Aspects

An *equilibrium state* of a system is a state that has no tendency to change without a change in external controls. The local state (σ, T, α) may be called a *local equilibrium state* if the internal variables remain constant at a constant stress and temperature. This can be mathematically stated as

$$\dot{\alpha} \;=\; g_i(\sigma, T, \alpha) \;=\; 0, \qquad i = 1, 2, ...n. \tag{3.35}$$

In an elastic continuum, every local state is an equilibrium state, though the continuum need not be globally in equilibrium. On the other hand, existence of *non-equilibrium* states

is an essential feature of rate-dependent inelastic continua. Such states evolve in time by means of *irreversible* processes, of which creep and relaxation are examples. Hence, the thermomechanics of inelastic continua belongs to the domain of *thermodynamics of irreversible processes* (Lubliner [1990]).

3.3.3 Generalized Flow Potential

A general concept of the flow potential is due to Rice [1970,1971]. First, a generalized flow potential is defined which is assumed to depend on the the stress, temperature and a set of internal variables. The flow and evolution laws can be obtained by simply differentiating this potential.

For a strain formulation, generally the Helmholtz free energy, $\overline{H}(\epsilon_{ij}, T, \epsilon^i_{ij}, \Lambda_\beta)$ is used as the generalized potential. This potential is convex and the mechanical and thermal quantities can be obtained as follows:

$$\sigma_{ij} \;=\; \frac{\partial \overline{H}}{\partial \epsilon^e_{ij}}, \quad s \;=\; -\frac{\partial \overline{H}}{\partial T}, \quad \alpha_\beta = \; -\frac{\partial \overline{H}}{\partial \Lambda_\beta}. \tag{3.36}$$

For a stress formulation, Gibb's complementary free energy (Φ), given by

$$\Phi(\sigma_{ij}, T, \alpha_\beta) \;=\; \sigma_{ij}\epsilon_{ij} \;-\; \overline{H} \tag{3.37}$$

is used as the generalized potential, from which the state variables can be obtained as

$$\epsilon_{ij} \;=\; \frac{\partial \Phi}{\partial \sigma_{ij}}, \quad s \;=\; -\frac{\partial \Phi}{\partial T}, \quad \Lambda_\beta \;=\; -\frac{\partial \Phi}{\partial \alpha_\beta}. \tag{3.38}$$

Further, the evolution is governed by the *dissipation potential*, $\Omega(\sigma_{ij}$,T,$\alpha_\beta)$ as

$$\dot{\epsilon}^I_{ij} \;=\; \frac{\partial \Omega}{\partial \sigma_{ij}}, \quad \dot{\Lambda}_\beta \;=\; -\frac{\partial \Omega}{\partial \alpha_\beta}. \tag{3.39}$$

3.3.4 Internal Variable Theory of Viscoplasticity

Most researchers use the term viscoplasticity in the classical sense, that is, to denote the description of rate-dependent behavior with a well defined yield criterion, but this usage is not universal. Others, following Bodner [1968], use the term for highly non-linear behavior,

without a well defined yield, that is characteristic of metals, especially at higher temperatures. These are unified models. Nevertheless, both of these are subclasses of the internal variable models (Lubliner [1990]).

Classical Viscoplasticity

Suppose we have a continuous function $f(\sigma, T, \alpha)$ such that there exists a region in stress space where $f(\sigma, T, \alpha) < 0$ and $\dot{\epsilon}^I_{ij} = 0$, then $f(\sigma, T, \alpha) = 0$ is the threshold surface in the stress space and the elastic region forms its interior. This definition does not require simultaneous vanishing of all the internal variable rates ($\dot{\alpha}_\beta$) in the elastic region. Hence, phenomenon like strain-aging, which require evolution of local structure while the material is stress-free, can be represented. However, this is of importance only for processes whose time scale is comparable to the relaxation time for strain-aging.

The dependence of the threshold function on the internal variables α_β describes the *hardening* properties of the material. During hardening, the threshold function decreases from a positive value toward zero at a constant stress and temperature, that is $\dot{f} < 0$. Similarly, softening is characterized by $\dot{f} > 0$. In the limiting case $\dot{f} = 0$, i.e. f is independent of α_β and the material is perfectly plastic material.

Unified Viscoplasticity

According to Bodner [1968], yielding is not a separate or independent criterion but is a consequence of a general constitutive law of the material behavior. Since the 1970's, several constitutive models for the rate-dependent inelastic behavior of metals have been formulated without a formal hypothesis of threshold surface. These models can successfully represent creep especially under high temperature without a decomposition of strain into plastic and creep strains. They have consequently come to be known as *unified* viscoplasticity models, and are particularly useful for the description of bodies undergoing significant temperature changes.

Perhaps the simplest unified model is due to Bodner and Partom [1972,1975] in which the

flow equations are given by

$$\dot{\epsilon}^I_{ij} \;=\; \phi\; S_{ij} \tag{3.40}$$

where

$$\phi = \phi(D_o, n, Z) \tag{3.41}$$

and D_o, n are material parameters and Z depends on the inelastic power ($\dot{W}_i$). The rate equation is

$$\dot{W}_i \;=\; \sigma_{ij}\dot{\epsilon}^I_{ij} \;=\; 2J_2\phi(W_i, J_2). \tag{3.42}$$

Here, temperature dependence is achieved through temperature-dependent material parameters.

More recently, sophisticated unified viscoplastic models, that describe many features of the behavior of metals at elevated temperatures have been developed. Arnold and Saleeb [1994] developed a *Generalized Viscoplastic model with Potential Structure* (GVIPS). In GVIPS, the total strain is decomposed into elastic and inelastic strains. However, it is still unified in the sense that the inelastic strain in not further decomposed into plastic and creep strains. It is a fully associative, multiaxial, non-isothermal, non-linear kinematic hardening model that accounts for most aspects of temperature and rate-dependent inelastic deformation. This is the baseline model that is modified in the current work and will be presented in detail in Chapter 4.

3.4 Review of Related Work

It is clear that the SD cannot be represented by the classical Mises yield criterion with an associated flow rule. This prompts us to look at more general constitutive models that can better represent the yield and flow behavior of the materials that exhibit a SD effect. Reviewed here are some forms of threshold functions, definitions of flow, and flow rules that have been used to capture different aspects of flow behavior in materials.

3.4.1 General Threshold Functions

One of the first general yield functions for metals was proposed by Drucker [1949] as described in equation 1.5. A function based on J_2-J_3 was better than either Tresca or von Mises functions in correlating yield surface data for the aluminum alloy. Further, he proved that the deformation theory of plasticity falls short in representing a general state of stress in a material and is not compatible with the J_2-J_3 representation of yield.

Spitzig et al [1975] proposed a generalized yield function to account for the observed SD effect in tempered AISI 4310 and 4330 steels.

$$f = J_2^{1/2} - a\, I_1 - b\, J_3^{1/3} - c \tag{3.43}$$

where a, b, and c are material constants. To be able to correctly predict the observed volume expansion during inelastic deformation, they suggested the use of a non-associated flow law.

Lee and Ghosh [1996] addressed the problem of expressing the non-coaxiality of stress path in constitutive modeling. Due to shear banding, all the stress increments in a given stress path do not have the same principal axes. This is referred to as non-coaxiality and is attributed to the rigid body rotations associated with pure shear, compressibility due to Poisson effect and plastic dilation. To account for non-coaxiality and shear banding commonly observed in deforming metals, they proposed the inclusion of J_3 in the constitutive model. To this end, they proposed two modifications to the Drucker-Prager criterion; one for materials weak in shear and another for those weak in tension.

Lissenden et al [1999] developed a method for determining rate dependent flow surfaces for Inconel 718. Inadequacy of J_2 based models to represent the asymmetry in yield (between tension and compression) led them to use the following forms for the yield functions:

$$\begin{aligned} f &= a\, I_1 + b\, J_2^{1/2} - 1 \\ f &= b^3 J_2^{3/2} + c\, J_3 - 1 \end{aligned} \tag{3.44}$$

where a, b, and c are material constants that fit to the experimental data. These functional forms fit the yield surface data very well and the outward normals to the surfaces were found to be consistent with the experimentally determined directions of the inelastic strain

rate vectors.

In order to characterize the viscoplastic behavior of geological materials, Desai and Zhang [1987] proposed a generalized yield function of the form

$$f = J_2 - (-\alpha\ I_1^n + \gamma\ I_1^2)[exp(\beta\ I_1) - \beta\ S_r]^m \tag{3.45}$$

where α, γ, β, n, and m are response functions and $S_r = J_3^{1/3}/J_2^{1/2}$. This yield function is continuous in stress space. It permits hierarchical development to incorporate progressive complexities such as associative and non-associative responses, anisotropic hardening, strain softening and fluid pressure.

Mandl and Luque [1970] analyzed a fully developed shear flow of frictional granular material. They justified the use of Mohr-Coulomb criterion for planar elements that have normals in the flow plane to describe yield in this situation. They rewrote the criterion in cartesian coordinates as

$$f = \left(\frac{\sigma_{xx} + \sigma_{yy}}{2}\right)\sin\rho + c\cos\rho - \left[(\frac{\sigma_{xx} - \sigma_{yy}}{2})^2 + \sigma_{xy}^2\right]^{1/2}. \tag{3.46}$$

Functions based on Internal Variables: Threshold Functions

Wegener and Schlegel [1996] studied the suitability of different yield functions for approximation of subsequent yield surfaces to capture various effects of distortional hardening. They chose a yield function of the form

$$f = f(\overline{\tau}, z_k, k = 1...) \tag{3.47}$$

where $\overline{\tau}$ is the effective shear stress, z_k are the internal variables that are tensorial in nature. They compared four experimental yield surfaces corresponding to different load paths from the work of Phillips and Tang [1972] and found that a sixth order tensor for z_k gave a good representation of the subsequent surfaces for all the cases.

Chaboche [1977] used inelastic strain(ϵ^I) and strain like symmetric second-rank tensor Λ as internal variables. The thermodynamic force conjugates to these variables are the stress-like variables, R and α_{ij}, respectively, and the assumed threshold surface is

$$f(\sigma, \alpha, R) \ = \ \sqrt{\tilde{J}_2} \ - \ \frac{R}{\sqrt{3}} \ - \ k_o \ = \ 0 \tag{3.48}$$

where

$$\tilde{J}_2 \;=\; \frac{1}{2}(s_{ij} - a_{ij})(s_{ij} - a_{ij}) \tag{3.49}$$

a_{ij} being the deviator of α_{ij} and k_o is the yield strength in shear. The yield surface is of Mises type, capable not only of expansion (as measured by R) but also of translation represented by a_{ij} which marks the center of elastic region. The invariants used in the yield function are effective deviatoric stress invariants.

Robinson and Ellis [1986] assumed the following form for the dissipation potential:

$$\Omega = k\left[\frac{1}{2\mu}\int F^n dF + \frac{R}{H}\int G'^m dG'\right] \tag{3.50}$$

where μ, R, H, n, m, k are material constants. The threshold function F depends on $\tilde{J}_2$ and $\tilde{J}_3$ and has its origin in Drucker's form (equation 1.5).

$$F(J_2, J_3) = \frac{(\tilde{J}_2^3 - c\tilde{J}_3^2)^{1/3}}{K^2} - 1 \tag{3.51}$$

and the function G' depends on the corresponding invariants of the internal stress (J_2' and J_3') as

$$G'(J_2', J_3') = \frac{({J_2'}^3 - c{J_3'}^2)^{1/3}}{K^2}. \tag{3.52}$$

The effective and internal stress invariants are defined in Chapter 4. The threshold function reduces to the Mises criterion for c=0, and Drucker's model for c=-1.75.

Hopkins [1990] developed the flow and the evolutionary laws for the above model. He arrived at the limits on the value of c using material stability criterion. He also determined functional forms for F and G' for non-monotonic loading conditions like stress reversals.

Janosik and Duffy [1997] pointed out that ceramic materials exhibit complex rate dependent thermo-mechanical behavior. To account for the SD effect and the sensitivity of these materials to hydrostatic pressure, they introduced $\tilde{I}_1$ and $\tilde{J}_3$ in the definitions of F and G' in the Willam and Warnke model [1975]. These functions were in turn used in Robinson's model to develop the constitutive laws for ceramics.

3.4.2 Flow Definitions

At elevated temperatures, metallic alloys exhibit strong time-dependent behavior and the concept of yield surface, in the classical sense, generally breaks down as we move into the realm of viscoplasticity. However, analogous geometrically and thermodynamically based concepts such as surfaces of constant strain rate (SCISRs) and surfaces of constant dissipations (SCDs) have been postulated to play the same central role in viscoplastic constitutive theories as yield surfaces do in classical plasticity. Physical quantities used to define the amount of inelastic flow in a material are defined mathematically as follows:

1. *Inelastic power* is the product of the stress and the inelastic strain rate.
2. *Dissipation* represents the rate of work that cannot be recovered in a process and mathematically is the difference between inelastic power and the product of internal stress and internal strain rate.
3. *Equivalent inelastic strain rate* is the square root of the self product of strain rate.

Battiste and Ball [1986] used SCISRs and Clinard and Lacombe [1988] used SCDs to describe the dissipation potentials at elevated temperature for monolithic materials. Lissenden et al [1997a] pointed out that SCISRs and SCDs need not represent the same surfaces under all conditions and hence needs careful consideration. A good example of this would be the dissipation potential in equation 3.50. For this potential, the two surfaces are different and become identical only if the J_3 dependence is removed. Of all the surface definitions that represent inelastic flow, the SCDs are most meaningful from the thermodynamics viewpoint.

An important issue is that the SCDs are not experimentally measurable. At best, experiments can measure the surfaces of constant inelastic power (SCIPs) as explained by Lissenden et al [2000]. Hence, it is important to correlate SCIPs that can be experimentally determined, to SCDs that are theoretically meaningful. This subject was addressed by Iyer et al [2000a].

3.4.3 Inelastic Behavior

In the inelastic region, the flow law relates the incremental stress to incremental inelastic strain. The associated flow law, which is widely used in classical plasticity theory, was described earlier. Here, the focus is on the *non-associated flow laws* that are required for describing inelastic flow in some materials.

Mroz [1963] pointed out that the vector of incremental plastic strain can rotate significantly for small inhomogeneity, even for a smooth yield surface, thereby leading to a non-associated flow rule. This inhomogeneity is caused by plastic deformation at the microscale and is a function of grain size, temperature, and elastic and plastic properties of the grain. According to him, the separation of total strain into elastic and plastic parts is difficult due to inhomogeneity, which affects hardening characteristics and laws of plastic deformation.

Spitzig et al [1975] used the yield function in equation 1.7 for describing flow in martensitic steels. An associated flow law overpredicted the volume expansion by a factor of 15. They proposed the use of non-associated flow law for accurate prediction of volume expansion during inelastic deformation. In Robinson's model the flow law is associative but the evolution law is non-associative.

Frantziskonis et al [1986] attributed the non-coaxiality of the plastic strain increment and the stress increment in granular materials to intergranular friction and changes in the physical state of the material during deformation. They proposed a correction to the yield function in equation 3.45 based on the deviation of the plastic strain increment from normality.

$$\overline{F} = f + h(J_i, \xi) \tag{3.53}$$

where h is the correction function that depends on the three invariants J_i, i=1 to 3, and ξ, which is a hardening parameter. The use of $\overline{F}$ for the yield function leads to a non-associated flow law, which is able to capture the effects such as volume change and stress path dependence.

Mandl and Luque [1970] found that the internal kinematical constraints cause the direction of the principal macrostress to deviate from the direction of strain increment, though the granular material is assumed to be completely isotropic. This non-coaxiality is perfectly

compatible with material isotropy and has only minor consequences on the mathematics of classical plasticity. They found the angle of deviation to be the half angle of internal friction for a critical void ratio. Drucker's stability postulate is not satisfied in the overall sense. They decompose the stress tensor into two parts; one capable of performing inelastic work and the other not capable of performing work. The inelastic strain increment is coaxial with the working part of stress, thereby indicating that a weakened form of the stability postulate holds.

Another instance of application of non-associated flow laws is by Kang and Willam [1999] who used a yield function that depends on all the three stress invariants and is continuous in stress space except at the point of equitriaxial tension. Application to concrete resulted in satisfactory prediction of brittle failure mode in tension and compression failure in pure shear with volumetric constraint.

Chapter 4

Proposed Viscoplastic Model

In this chapter, a viscoplastic model capable of predicting a SD is proposed and subsequently specialized for aged IN718 at $650°C$. This model is an extension of the Generalized Viscoplastic Model with Potential Structure (GVIPS), developed by Arnold and Saleeb [1994]. First, a background relating to the internal variables used in GVIPS is presented. This is followed by the theoretical framework of GVIPS and constitutive equations. The proposed modifications to GVIPS to account for the observed SD are presented and the resulting formulation is derived, giving the flow and evolutionary laws. Finally, a detailed procedure to estimate the material parameters in the model is proposed.

4.1 Background

Inelasticity exhibited by the thermomechanical response of engineering materials is related to *irreversible thermodynamic processes*. These involve energy dissipation and material stiffness variations due to physical changes in the microstructure. Consequently, thermodynamic arguments have often been utilized in the *internal variable approach* in the formulation of phenomenological constitutive laws (Coleman and Gurtin [1967]; Rice [1971]; Lubliner [1972,1973]; Lemaitre and Chaboche [1990]).

Thermodynamic admissibility restrictions associated with various dissipative mechanisms underlying the above models reduce to the well-known Clausius-Duhem or *dissipation*

inequality. The thermodynamically based constitutive equations in these models are discussed with respect to the above restriction. Mathematical constructs of *flow or dissipation potential* and the associated normality conditions are introduced for convenience in satisfying the above constraints based on simple properties of *non-negativeness* and *convexity* of these functions (Ponter and Leckie [1976]; Rice [1970]; Ponter [1976], Onat and Leckie [1988]; Robinson and Duffy [1990]; Lemaitre and Chaboche [1990]; Freed et al [1991]). Such forms however, do not automatically imply the existence of total or integrated forms of thermodynamic potentials; for example, the Helmholtz free energy or the Gibb's complementary free energy. If the latter is assumed a-priori, the corresponding formulation is termed a *complete* potential-based structure; on the other hand, those derived from an assumed dissipation potential form are referred to as *incomplete* potential-based models.

The complete potential-based class of inelastic constitutive equations possesses a number of distinct and important attributes:

1. They constitute the cornerstone of numerous regularity properties and bounding theorems in plasticity and viscoplasticity (Ponter [1976,1979,1980]).

2. They result in sufficiently general variational structure, whose properties can be exploited to derive a number of useful material conservation laws (Eshelby [1951,1956]; Rice [1968]).

3. The discrete form of the assumed Gibb's potential is numerically advantageous in the development of efficient algorithms for finite element implementation (Saleeb et al [1990]; Saleeb and Wilt [1993]; Maier and Novati [1990]).

A number of variables have been used to describe the evolution of the internal structure, as inelastic deformation occurs. The ones usually used in sophisticated unified theories are defined here.

1. *Internal Stress* represents the inner stress field associated with immobile dislocations. It is smaller than the applied stress.

2. *Effective Stress* is the difference between applied and the internal stresses.

3. *Drag Stress* is based on the dislocation motion. Increase in drag stress decreases the inelastic strain rate and thus increases the size of the elastic region, similar to isotropic hardening.

   GVIPS uses two variables; the *drag stress* which is non-evolving, and the *internal stress*, which is tensorial and evolves with inelastic deformation.

4.2 Theoretical Framework

GVIPS applies to an initially isotropic material. It is limited to small deformations and the initial state of the material is assumed to be stress-free. Gibb's thermodynamic potential function (Φ) is assumed to depend on stress, temperature, and an array of internal variables (Coleman et al [1967]; Lubliner [1972,1973]).

In its differential form, the Gibb's potential, $\Phi(\sigma_{ij}, \alpha_\beta, T)$, is written as follows (Lubliner [1973]; Ponter [1979]):

$$d\Phi \;=\; -\epsilon_{ij} d\sigma_{ij} \; - S dT \; - \Lambda_\beta d\alpha_\beta \tag{4.1}$$

where S denotes the entropy, α_β the internal state variables, Λ_β the thermodynamic affinities corresponding to α_β, ϵ_{ij} the total strain and σ_{ij} the stress tensor. It follows from equation 4.1 that

$$\begin{aligned} \epsilon_{ij} &= -\frac{\partial \Phi}{\partial \sigma_{ij}} \\ S &= -\frac{\partial \Phi}{\partial T} \\ \Lambda_\beta &= -\frac{\partial \Phi}{\partial \alpha_\beta} \end{aligned} \tag{4.2}$$

are defined as the *equations of state* (Malvern [1969]; Lemaitre and Chaboche [1990]) and σ_{ij}, α_β, and T are force-like thermodynamic state variables while ϵ_{ij}, Λ_β, and S are the corresponding conjugate displacement-like variables. The most general expression for the total strain rate is obtained by differentiating the first of the above equations as

$$\dot{\epsilon}_{ij} \;=\; \frac{d}{dt}\left(-\frac{\partial \Phi}{\partial \sigma_{ij}}\right) \;=\; -\frac{\partial^2 \Phi}{\partial \sigma_{ij} \partial \sigma_{rs}} \dot{\sigma}_{rs} \; - \; \frac{\partial^2 \Phi}{\partial \sigma_{ij} \partial \alpha_\beta} \dot{\alpha}_\beta \; - \; \frac{\partial^2 \Phi}{\partial \sigma_{ij} \partial T} \dot{T}. \tag{4.3}$$

Two options are available for describing the flow and evolutionary equations. The first option assumes a *fully coupled* form, i.e., the inelastic strain rate is intimately linked to

the thermodynamic internal state, hence its functional dependence is completely defined once Φ is assumed. This form is too restrictive, in that it requires proportionality between the inelastic strain and the rate of change of internal state (Arnold and Saleeb [1994]). As a result, the classical definition of steady state creep which requires an evolving inelastic strain at a constant internal state, cannot be attained using this coupled form. This leads us to the second option; a *decoupled Gibb's* form, in which the selected internal state variables are grouped a priori by separation of the inelastic strain as an independent state parameter and suppressing all stress dependency of the remaining associated internal state groups in the selected Φ function. This form indeed allows the classical steady state creep.

4.2.1 Decoupled form

In the decoupled form, the evolution of inelastic strain is independent of the internal force-like state variables, α_β, associated with material inelasticity. It is this separation that allows for inclusion of the classical notation of steady state creep. The Gibb's potential for an isothermal case is expressed as

$$\Phi \;=\; E(\sigma_{ij}) \;-\; \sigma_{ij}\epsilon^I_{ij} \;+\; H'(\alpha_\beta) \tag{4.4}$$

where E is negative of the elastic strain energy, the second term is inelastic work, and H' is a material function.

Differentiating equation 4.4 with respect to stress, gives the total strain rate as a sum of two components; elastic (or reversible)($\dot{\epsilon}^e_{ij}$), and inelastic($\dot{\epsilon}^I_{ij}$).

$$\dot{\epsilon}_{ij} = -\frac{\partial \Phi}{\partial \sigma_{ij}} = \dot{\epsilon}^e_{ij} \;+\; \dot{\epsilon}^I_{ij} \tag{4.5}$$

where

$$\dot{\epsilon}^e_{ij} = \left[-\frac{\partial^2 E}{\partial \sigma_{ij}\partial \sigma_{rs}}\right]\dot{\sigma}_{rs} \tag{4.6}$$

and inelastic strain rate, $\dot{\epsilon}^I_{ij}$, is defined separately.

For an isothermal process, the energy balance requires that the external work rate be equal to the sum of the internal work rate and the dissipation, i.e.

$$\sigma_{ij}\dot{\epsilon}^I_{ij} = \Omega(\sigma_{ij}, \alpha_\beta) + \alpha_\beta \dot{\Lambda}_\beta.$$

The second law states that the change in entropy is positive. For an isothermal process

$$\Omega(\sigma_{ij}, \alpha_\beta) \;=\; \sigma_{ij}\dot{\epsilon}^I_{ij} \;-\; \alpha_\beta \dot{\Lambda}_\beta \;\geq\; 0. \tag{4.7}$$

This is called the *dissipation inequality.*

The inelastic strain rate $\dot{\epsilon}^I_{ij}$ is defined such that the dissipation inequality is satisfied. Differentiating the dissipation potential Ω with respect to σ_{ij} and α_β we get the flow and evolution laws,

$$\dot{\epsilon}^I_{ij} \;=\; \frac{\partial \Omega}{\partial \sigma_{ij}} \tag{4.8}$$

$$\dot{\Lambda}_\beta \;=\; -\frac{\partial \Omega}{\partial \alpha_\beta} \tag{4.9}$$

respectively. Using the Gibb's potential, the evolution law can also be written as

$$\dot{\Lambda}_\beta \;=\; \frac{d}{dt}\left[-\frac{\partial \Phi}{\partial \alpha_\beta}\right] \;=\; Q_{\beta l}\, \dot{\alpha}_l \tag{4.10}$$

where

$$Q_{\beta l} \;=\; -\frac{\partial^2 \Phi}{\partial \alpha_\beta \partial \alpha_l} \tag{4.11}$$

relates the internal force-like variables to the internal displacement-like variables and is called the *internal compliance operator.* This operator is completely defined once Φ is chosen. It is interesting to note that this operator provides information about the curvature of the Gibb's potential as well as the relaxation trajectories in the associated stress space (Arnold [1987]). The evolution law for the internal variable is

$$\dot{\alpha}_l \;=\; -\,[Q^{-1}_{\beta l}]\frac{\partial \Omega}{\partial \alpha_\beta}. \tag{4.12}$$

The Gibb's and dissipation potentials are directly linked through the internal state variables. Clearly, this framework provides a structure in which the flow and evolutionary laws are fully associative and hence easily integrable.

4.3 Generalized Viscoplastic model with Potential Structure

Using the above framework, Arnold et al [1996] developed a multiaxial, potential based, fully associative, isothermal, unified viscoplastic model. This model possesses one tensorial internal state variable, the internal stress (α_{ij}) that is associated with dislocation motion.

The forms of the Gibb's potential (Φ) and the dissipation potential (Ω) are chosen as follows (Saleeb and Wilt [1993]):

$$\Phi \;=\; \frac{1}{2}\sigma_{ij}\epsilon_{ij} \;-\; \frac{\kappa^2}{(1+\beta)H}G^{\beta+1} \tag{4.13}$$

$$\Omega \;=\; \kappa^2\left[\frac{1}{2\mu}\frac{\langle F\rangle^{n+1}}{(n+1)} \;+\; \frac{R}{H}\frac{\langle G\rangle^{m+\beta+1}}{(m+\beta+1)}\right] \tag{4.14}$$

where κ, μ, $n(\geq 1)$, $m(\geq \beta+1/2)$, β, R, and H are positive material parameters. The first three are associated with the flow law and the rest with the evolution equation. The scalar function F depends on the effective stress and G depends on the internal stress invariants. The McCauley brackets are such that

$$\begin{aligned}\langle F\rangle &= F \quad if \quad F>0\\ &= 0 \quad otherwise\end{aligned}$$

$$\begin{aligned}\langle G\rangle &= G \quad if \quad G>G_o\\ &= G_o \quad otherwise.\end{aligned}$$

This ensures use of different forms of F in different regions of the state space to account for stress-reversals, cyclic-loading and dynamic recovery effects. Also, G_o is the cut-off value of G, which is a small constant that helps fit the experimental data and prevents singularity in the numerical solution when G tends to zero.

In the spirit of von Mises and owing to the deviatoric nature of the inelastic deformation, only the quadratic invariants are considered in the definitions of the potentials for this model. Hence the definitions of F and G are as follows:

$$F \;=\; \frac{\tilde{J}_2}{\kappa^2} - 1 \tag{4.15}$$

$$G \;=\; \frac{J_2'}{\kappa^2} \tag{4.16}$$

where $\tilde{J}_2$ is the effective deviatoric stress invariant defined as

$$\tilde{J}_2 \;=\; \frac{1}{2}\Sigma_{ij}\Sigma_{ij} \tag{4.17}$$

and J_2' is the internal deviatoric stress invariant given by

$$J_2' = \frac{1}{2} a_{ij} a_{ij} \tag{4.18}$$

and the effective deviatoric stress is

$$\Sigma_{ij} = S_{ij} - a_{ij}. \tag{4.19}$$

The function F, acts like a threshold surface because no inelastic strain will occur if $F < 0$. The size of this surface is dictated by the shear strength (κ) and its location is determined by α_{ij}. Following the above framework and using these potentials (equations 4.13 and 4.14), the flow law is derived as

$$\dot{\epsilon}_{ij}^I = \frac{F^n}{2\mu} \Sigma_{ij} \tag{4.20}$$

and the evolution equations for the internal stress are

$$\dot{\alpha}_{ij} = \left(I_{ijkl} - \frac{\beta}{G(1+2\beta)} a_{ij} a_{kl} \right) \left(\frac{H}{G^\beta} \dot{\epsilon}_{kl}^I - R G^m a_{kl} \right) \tag{4.21}$$

where I_{ijkl} is the fourth order identity tensor.

The above equation consists of two terms that represent competing mechanisms in the material; (1) a hardening term (associated with H, β) that accounts for the strengthening mechanisms, and (2) a recovery term (associated with R, m) that accounts for the softening mechanisms and is called *strain-induced recovery* or *dynamic recovery*. These competing terms in the evolution equations are consistent with the assumption about the nature of internal mechanisms in the material (Miller [1987]; Freed et al [1991]).

4.4 Proposed Model

The model described in the previous section is J_2-based, which is suitable for many metals like titanium (Arnold et al [1996]). It cannot, however, account for the SD phenomenon which is observed in aged Inconel 718. To do so, we need to generalize the above model. The starting point here is the choice of Gibb's and the dissipation potentials which have the same form as equations 4.13 and 4.14 respectively. The threshold function is generalized and then the flow and evolutionary laws are derived.

Table 4.1: Material parameters for various threshold functions

Source	Threshold (Yield) Function	m	a	b	c
Mises	$\sqrt{J_2}$-k	1/2	0	1/k	0
Drucker-Prager	$\alpha I_1 + \sqrt{J_2}$-k	1/2	α/k	1/k	0
Drucker	J_2^3-$\frac{9}{4}J_3^2$-k^6	3	0	$1/k^6$	-9/($4k^6$)

4.4.1 Modified Threshold Function

As mentioned before, an elastically isotropic material that exhibits a SD must be represented by a threshold function that depends on an odd power of $\tilde{I}_1$ or $\tilde{J}_3$ or a combination of both. Pressure sensitivity requires dependence on $\tilde{I}_1$ while pressure insensitivity requires dependence on $\tilde{J}_3$ (and not $\tilde{I}_1$). Here, the threshold function is generalized to include all the effective stress invariants as follows:

$$F = a\ \tilde{I}_1^{2m_1} + b\ \tilde{J}_2^{m_1} + c\ \tilde{J}_3^{\frac{2m_1}{3}} - 1 \tag{4.22}$$

where a, b, c, and m_1 are constants to be fit to the experimental data. The invariants $\tilde{I}_1$ and $\tilde{J}_3$ are defined as

$$\begin{aligned} \tilde{I}_1 &= \sigma_{ii} - \alpha_{ii} \\ \tilde{J}_3 &= \frac{1}{3}\Sigma_{ij}\Sigma_{jk}\Sigma_{ki}. \end{aligned}$$

This form is convenient to use because it is an additive combination of all three effective stress invariants. Initially, when the internal variables are zero, the invariants depend on the external deviatoric stresses only, and the threshold function F is the yield function.

There are several advantages of choosing such a form of threshold function.

1. It is most general in that it incorporates all the three effective stress invariants.
2. The polynomial form is convenient for differentiation which is required to derive the flow and evolution laws.
3. Equation 4.22 can be easily reduced to some of the classical yield functions by choosing suitable values for a, b, c, and m_1 as shown in Table 4.1.

4. For pure shear loading ($\tilde{I}_1$=$\tilde{J}_3$=0), the above functional form reduces to

$$F = b\tilde{J}_2 - 1$$

which has the same form as the baseline GVIPS model. This feature will be useful in characterizing the model, which is detailed in subsequent sections.

Further, for better flexibility of data fitting, the above threshold function is modified as

$$F = [a\ \tilde{I}_1^{2m_1} + b\ \tilde{J}_2^{m_1} + c\ \tilde{J}_3^{\frac{2m_1}{3}}]^{\frac{1}{m_1}} - 1. \tag{4.23}$$

Notice that threshold function in the equation 4.23 also reduces to the baseline GVIPS model for pure shear loading ($\tilde{I}_1$=$\tilde{J}_3$=0).

4.4.2 Flow and Evolution laws

Function G, which depends on the internal variables is chosen to have the same form as F and can be written as

$$G = [aI_1'^{2m_1} + bJ_2'^{m_1} + cJ_3'^{\frac{2m_1}{3}}]^{\frac{1}{m_1}} \tag{4.24}$$

where a, b, c, and m_1 are same as those in equation 4.23. The invariants I_1' and J_3' are defined as

$$\begin{aligned} I_1' &= \alpha_{ii} \\ J_3' &= \frac{1}{3}a_{ij}a_{jk}a_{ki}. \end{aligned}$$

Using these functions in the Gibb's and the dissipation potentials (equations 4.13 and 4.14), and by appropriate differentiation of the potentials, we can derive the flow and evolution laws. In this section, only the final formulae are given. Detailed derivation is given in Appendix A.

Flow Law

The associated flow law (equation 4.8) is used to derive the flow law. Using Ω (equation 4.14) the inelastic strain rate tensor is obtained as

$$\dot{\epsilon}_{ij}^I = \frac{\kappa^2}{2\mu}F^n(F+1)^{1-m_1}\Upsilon_{ij} \tag{4.25}$$

where

$$\Upsilon_{ij} = (2a\tilde{I}_1^{2m_1-1} - \frac{4}{9}c\tilde{J}_2\tilde{J}_3^{\frac{2}{3}m_1-1})\delta_{ij} + b\tilde{J}_2^{m_1-1}\Sigma_{ij} + \frac{2}{3}c\tilde{J}_3^{\frac{2}{3}m_1-1}\Sigma_{iq}\Sigma_{jq}.$$

Equation 4.25 is the flow law for the proposed model.

Evolution Law

The evolution equations for the internal variables can be obtained in a similar manner using equation 4.12 as follows:

$$\begin{aligned} \dot{\Lambda}_{ij} &= -\frac{\partial\Omega}{\partial\alpha_{ij}} \\ &= \dot{\epsilon}^I_{ij} - \frac{\kappa^2 R}{H}G^{(1+\beta+m-m_1)}\Theta_{ij} \end{aligned} \tag{4.26}$$

where

$$\Theta_{ij} = (2aI_1'^{2m_1-1} - \frac{4}{9}cJ_2'J_3'^{\frac{2}{3}m_1-1})\delta_{ij} + bJ_2'^{m_1-1}a_{ij} + \frac{2}{3}cJ_3'^{\frac{2}{3}m_1-1}a_{iq}a_{jq}$$

where a_{ij} is the internal deviatoric stress tensor. Equation 4.26 is the evolution law for the proposed model.

Internal Constitutive Equation

The internal compliance tensor Q_{ijkl} is obtained by differentiating Φ (equation 4.13).

$$Q_{ijkl} = -\frac{\partial^2\Phi}{\partial\alpha_{ij}\partial\alpha_{kl}} = \frac{\kappa^2}{H}\frac{\partial[G^\beta\frac{\partial G}{\partial\alpha_{kl}}]}{\partial\alpha_{ij}}. \tag{4.27}$$

The internal constitutive rate equation is

$$\dot{\alpha}_{ij} = L_{ijkl}\dot{\Lambda}_{kl} \tag{4.28}$$

where Λ_{ij} are displacement like variables that are conjugate to internal stress tensor (α_{ij}) and L_{ijkl} is the internal stiffness tensor ($= Q^{-1}_{ijkl}$). Using G in equation 4.24 and differentiating

we get

$$
\begin{aligned}
Q_{ijkl} = & \qquad (4.29)\\
& \frac{\kappa^2}{H} G^{(1+\beta-m_1)}[(2a(2m_1-1)I_1'^{2m_1-2} - \frac{b}{3}J_2'^{m_1-1} + \frac{8c}{27}(\frac{2}{3}m_1-1)J_2'^{2}J_3'^{\frac{2}{3}m_1-2})\delta_{ij}\delta_{kl}\\
& + b(m_1-1)J_2'^{m_1-2}a_{ij}a_{kl} + bJ_2'^{m_1-1}\delta_{ik}\delta_{jl}\\
& + \frac{2c}{3}J_3'^{\frac{2}{3}m_1-1}(a_{il}\delta_{kj} + a_{jl}\delta_{ik} - \frac{2}{3}a_{ij}\delta_{kl} + (\frac{2}{3}m_1-1)\frac{1}{J_3'}(a_{iq}a_{jq}a_{kp}a_{lp} - \frac{2J_2'}{3}a_{iq}a_{jq}\delta_{kl}))\\
& - \frac{4c}{9}J_3'^{\frac{2}{3}m_1-1}((\frac{2}{3}m_1-1)\frac{J_2'}{J_3'}a_{kp}a_{lp}\delta_{ij} + a_{kl}\delta_{ij}) + \left(\frac{1+\beta-m_1}{G^{m_1}}\right)\Theta_{ij}\Theta_{kl}].
\end{aligned}
$$

This compliance tensor, when inverted and substituted in equation 4.28, will completely define the evolution of internal stress. It is seen from equation 4.27 that the internal compliance is not constant. It depends on the deviatoric and mean internal stresses. Thus equation 4.28 is highly non-linear and rate dependent. A key difference between this model and the baseline GVIPS model is the internal constitutive rate equation. Here, the total internal stress rates are related to the internal strain rate ($\dot{\Lambda}_{ij}$), while in the baseline model the deviatoric variables are employed.

4.5 Characterization of Material Parameters

The model now has eleven independent material parameters that need to be determined for aged Inconel 718 at 650°C. These parameters are summarized below.

1. Flow law parameters (κ, μ, n): κ is the threshold stress in pure shear, μ is associated with the viscosity of the material, and n is an exponent.

2. Hardening parameters (H, β): These are responsible for work hardening of the material during plastic deformation.

3. Recovery parameters (R, m): These parameters are associated with the recovery mechanism that competes with the hardening mechanism in the material.

4. Threshold function parameters (a, b, c, m_1): Parameter a scales the mean stress invariant I_1 while c scales J_3, and m_1 is an exponent.

The parameter b is set to $1/\kappa^{(2m_1)}$ so that for a pure shear loading the threshold function, and hence the flow and evolution equations will reduce to the baseline GVIPS model.

The methodology for characterizing the remaining ten material parameters is as follows:

1. Conduct pure shear experiments on aged Inconel 718. Fit the parameters associated with flow and evolution laws (GVIPS parameters), κ, μ, n, m, β, R and H to these data using optimization. Since $\tilde{I}_1$=$\tilde{J}_3$=0 the parameters a, c, and m_1 will not affect the prediction of GVIPS parameters.

2. Conduct axial tension and axial compression experiments on aged Inconel 718. Use the GVIPS parameters (obtained from step 1) to fit the parameters a, c, and m_1 to these data.

3. Ensure that a, b, c, and m_1 are such that the resulting initial threshold surface is convex, thereby satisfying Drucker's stability postulate at a material point.

These steps are necessary, in part, due to limitations with the current characterization tools, which are explained in detail in the following subsections.

4.5.1 Parameters associated with flow and evolution

GVIPS parameters are fit to the pure shear experimental data on Inconel 718. This is done using the Constitutive Material Parameter Estimator (COMPARE), a software package developed by Saleeb et al [1998]. COMPARE was run on a NASA-GRC computer system. Material parameters are determined by minimizing the errors between the experimental data and the predicted response. It uses both optimization and constitutive model (J_2 based) analysis, casts the estimation as a minimum error weighted, multi-objective optimization problem, and then solves the optimization using a sequential quadratic programming technique. It has three main parts that are summarized below.

Primal Analysis

This module is responsible for numerically simulating the load paths used in the experiments. It is similar to nonlinear finite element code built upon a single four node plane stress element with material nonlinearity capability. A fully implicit backward Euler scheme with corresponding algorithmic (consistent) tangent stiffness matrix is used because of its robustness and superior stability and convergence properties.

Sensitivity Analysis

Sensitivity analysis involves the calculation of parameter sensitivities to the predicted response. The sensitivity analysis is of the direct type performed on the basis of an explicit recursive form associated with the above integrator. The sensitivities are naturally derived from exact expressions in conformity with the underlying integration scheme. The advantage of this approach is the improved computational efficiency, while the disadvantage is the necessary analytical derivation of sensitivities that at times become complicated. However, the former outweighs the accompanying complexity.

Optimization

The multi-objective optimization problem is formulated in COMPARE and solved using a sequential quadratic nonlinear programming technique (Schittkowski [1981]). Its salient features are:

1. Design variable formulation that includes component synthesis, i.e. active/passive design variables. During optimization, the active design variables are modified and the passive ones are not.

2. General scaling of objective functions as well as design variables for numerical simplicity.

3. Formulation of a single design optimization problem through a weighted objective function.

The weighted objective function $\mathcal{F}(\S)$ for p tests is minimized to find n variables $\S$. Here $\mathcal{F}(\S)$ is expressed as

$$\mathcal{F}(\S) = \sum_{i=1}^{p} \frac{W_i f_i(\S)}{A_o} \tag{4.30}$$

where

$$f_i(\S) = \frac{1}{2} \sum_{j=1}^{n_p} \sum_{k=1}^{n_R} \left(1 - \frac{R_k}{R_{p_k}}\right)^2$$

and

$$A_o = \sum_{i=1}^{p} W_i |f_{io}(\S)|.$$

W_i is the weighted parameter for the i^{th} test such that

$$\sum_{i=1}^{p} W_i = 1.$$

$f_i(\S)$ is the objective function for the i^{th} test with initial value $f_{io}(\S)$. n_p is the number of measurement stations along a load history. R_k and R_{p_k} are the k^{th} components of response from analysis and test, respectively. n_R is the number of measured components at a particular j^{th} station.

The input requirements and procedure followed for using COMPARE to estimate these material parameters are detailed in Chapter 6.

4.5.2 Determination of threshold function parameters

After the seven parameters associated with flow and evolution law are determined and having set $b = 1/\kappa^{2m_1}$, it remains to determine the parameters a, c, and m_1. Material response to a general loading path that results in non-zero stress invariants $\tilde{I}_1$ and $\tilde{J}_3$ is required to determine these parameters. Data from uniaxial tension and compression experiments (which result in non-zero $\tilde{I}_1$ and $\tilde{J}_3$) are to be used for this.

The $\tilde{J}_2$ model (a = c =0) will predict identical responses in tension and compression and thus will not capture the SD effect. By suitably choosing the values for a, c, and m_1 it is possible to match the predicted responses in tension and compression with experimental

data. This is done iteratively. Multiple sets of parameters (a, c, m_1) can be found that may fit the data equally well, resulting in I_1J_2, J_2J_3, and $I_1J_2J_3$ models. The procedure for determining the proper combination of (a, c, m_1) for Inconel 718 is explained later. This will determine whether the SD phenomenon is caused by the effect of hydrostatic pressure, or by influence of J_3, or both.

4.5.3 Convexity Requirement

Convexity of the yield surface is a consequence of Drucker's stability postulate. This means that the values of a, b, c, and m_1 are not completely arbitrary. Thus, for a given m_1, though multiple combinations of a and c may fit the axial experimental data in tension and compression, only those combinations that satisfy the convexity requirement are acceptable.

Outlined here is a procedure to verify convexity of any given function in three-dimensional space (Iyer and Lissenden [2000b]). Using this procedure, we can determine the limits that the convexity requirement places on the threshold function parameters.

The basic requirement for convexity of a three-dimensional surface is that its curvature must be non-negative everywhere on the surface. That is, the curvature of the function in two mutually perpendicular directions in the tangent plane at any given point on the surface, must be non-negative. Mathematically, this requires that the curvature tensor be positive definite.

An arbitrary vector u_i and the tangent plane to the threshold surface are shown in principal stress space in Figure 4.1 . The components of this vector in the normal and tangential directions to the threshold surface are also shown. Since u_i is arbitrary, all vectors that lie in the tangent plane are given by $(\delta_{ij} - n_i n_j)u_j$, where n_i denotes the unit outward normal to F. The unit vectors in the tangent plane are $\delta_{ij} - n_i n_j$. Orthonormalizing this vector gives a set of three basis vectors, two of which lie on the tangent plane, the third being the unit normal vector itself.

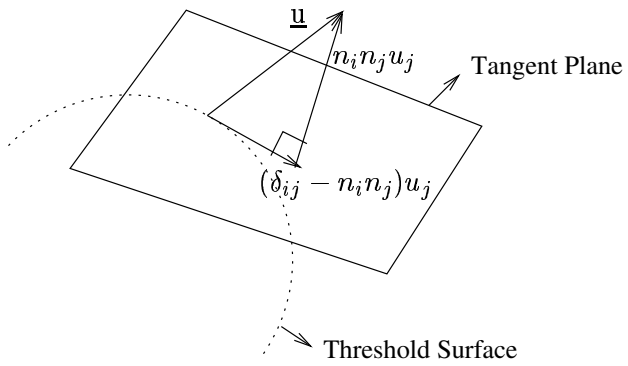

Figure 4.1: Basis vector determination

The curvature in the tangential plane is given by

$$\aleph_{pq} = \begin{bmatrix} U_{11} & U_{12} & U_{13} \\ U_{21} & U_{22} & U_{23} \end{bmatrix} \begin{bmatrix} H_{11} & H_{12} & H_{13} \\ H_{21} & H_{22} & H_{23} \\ H_{31} & H_{32} & H_{33} \end{bmatrix} \begin{bmatrix} U_{11} & U_{12} \\ U_{12} & U_{22} \\ U_{13} & U_{23} \end{bmatrix} \tag{4.31}$$

where H_{ij} is the Hessian of F given by

$$H_{ij} = \frac{\partial^2 F}{\partial \sigma_i \partial \sigma_j} \tag{4.32}$$

where σ_i is the principal stress vector. $\mathbf{U}$ consists of two basis vectors that lie in the plane tangent to F in the principal stress space.

Using the above procedure, material parameters associated with flow and evolution laws (κ, μ, n, β, m, R, H) and prescribed combinations of threshold surface parameters (a, c, m_1) will be determined. To find the right combination of (a, c, m_1) that describes the material behavior accurately, we need to consider material response for load paths other than pure shear and uniaxial loadings. These are validation experiments that will be detailed in subsequent chapters. Uniaxial testing under hydrostatic pressure will be an added advantage. These will help us to confirm the importance of I_1 (value of a) for this material.

Chapter 5

Experimental Program

This chapter starts with a brief review of relevant experimental work on inelastic deformation of metals. Next, the details of the test system and specimens used in the present investigation are presented. A detailed section on the design of experiments follows, which establishes a method to isolate the effect of each stress invariant on deformation in three dimensional principal stress space. The method is then simplified for axial-torsional space. Finally, the test matrix for the characterization tests of Inconel 718 is presented.

Experimental evaluation is an important step in the development of multiaxial viscoplasticity models. In general, three types of experiments are necessary to support the development of any potential based models (Robinson [1985]) for high temperature structural materials. These are as follows:

1. *Exploratory tests*: These tests guide the development of the theoretical framework and help examine the mathematical aspects of the framework. For a potential based framework, they help in developing the functional forms of the Gibb's and the dissipation potentials.

2. *Characterization tests*: These tests provide the required database for determining the specific functional forms and the parameters that represent a specific material for a specific temperature range. Usually these are simple tests like tension, compression and shear on relatively simple specimen geometries.

3. *Validation tests*: These tests provide the ultimate test of the constitutive model by comparing actual structural component response with analytical predictions based on the proposed model. For most cases, simple specimen geometries are used and the loadings are complex enough to rigorously test the model.

Tensile and compressive tests with superimposed hydrostatic pressure provide information about the significance of I_1 in describing the flow and evolution laws for the material. In the present investigation, these tests are intended to be used qualitatively to validate the models that include I_1 in the threshold function.

5.1 Review of experiments

Plasticity experiments have been conducted on metals to study their yield and flow behavior. Volume expansion during inelastic deformation was the emphasis in many investigations. Both uniaxial and multiaxial loadings have been reported. Such experiments date back to Lode [1926] who tested thin walled metal tubes in tension and internal pressure. There was a discrepancy between experimental data and the Mises yield criterion, which led Taylor and Quinney [1931] to further investigate the effect of biaxial (axial and torsional) loadings on tubular specimens of copper, aluminum and steel. In general, their work showed good agreement with Mises yield criterion for these materials. They also performed large deformation uniaxial tensile tests on these materials and monitored the changes in internal volume of the specimens. They found large changes in internal volume that could not be accounted for by small density changes and attributed it to the anisotropy induced during inelastic deformation.

Most biaxial testing was done using proportional loading (Phillips et al [1957,1961], Findley et al [1962], Michno and Findley [1976]). Biaxial experiments on metals at high temperatures ($> 500°$C) were difficult to perform owing to the complexity in experimentation and the associated difficulty in accurate measurement of strains.

Dependence of inelastic deformation on hydrostatic pressure has been another topic of investigation for metals. Contrary to the experimental findings of Bridgman [1952], some metals have exhibited dependence of flow on hydrostatic pressure. Drucker [1973] pointed

out that the SD phenomenon can result as a consequence of pressure dependent yielding. Spitzig et al [1975] have shown that several high strength steels (tempered 4310 and 4330) that exhibited SD effect indeed showed pressure dependent yielding. The volume expansion observed in these materials was in accord with the expected increase in dislocation density during deformation, but did not agree with the normality rule predictions.

Another type of plasticity experiment is the determination of initial and subsequent yield surfaces. Comprehensive reviews of these experiments have been provided by Michno and Findley [1976] and Hecker [1976]. Most of these experiments involved axial torsional loading on thin walled tubular specimens. The pros and cons of using strain and stress controlled loadings were investigated by some researchers. Phillips and Lu [1984] used stress and strain controlled loadings to determine yield surfaces for pure aluminum and found no appreciable difference between the two. On the other hand, some researchers preferred strain controlled loading to stress controlled loading and argued that the former leads to more accurate results(Wu and Yeh [1971], Ellis et al [1983]). Dependence of yielding on texture was determined by Althoff and Wincierz [1972] by experiments on textured brass and aluminum. Subsequent yield surfaces were also a focal point in many experimental investigations (Nagdhi et al [1958], Phillips and Tang [1972], Williams and Svensson [1970,1971]). In general, the inelastic strain rate vector was found to be normal to the yield surface (Michno and Findley [1974], Phillips and Moon [1977], Khan and Wang [1993]). This suggests that an associated flow law is a good approximation for most metals.

The shape of flow surfaces is strongly dependent on the flow definition (chapter 3). There has been some effort in the determination of flow surfaces, both surfaces of constant inelastic power (SCIPs) (Clinard and Lacombe [1988]) and surfaces of constant inelastic strain rate (SCISRs)(Battiste and Ball [1986]). These flow surfaces are either determined directly during experiments or by using post experiment data reduction techniques. For direct determination, the inelastic strain rate must be calculated in real time (Ellis and Robinson [1985], Battiste and Ball [1986], Lissenden et al [1997a]).

Gil [1999b] established an experimental program to determine yield and flow surfaces for solutioned and aged Inconel 718. Using axial-torsional loading SCISRs and SCIPs in axial-shear stress plane were constructed (for temperatures between 23°C and 649°C). He found

that the initial yield surfaces for solutioned Inconel 718 at low temperatures fit the Mises criterion. However, the yield loci for solutioned Inconel 718 at high temperature ($> 350°C$) and the yield loci for aged alloy for all the temperatures investigated, showed an eccentricity toward compressive stress direction (see Figure 1.1(b)). This is the SD phenomenon in Inconel 718 and is the topic of present investigation.

In general, plasticity experiments on metals have dealt with determining yield surfaces (initial and subsequent) and finding the effect of loading (type of control, rate) on hardening behavior. The effect of hydrostatic pressure on yield and flow is another topic of interest. The present work involves loadings, both uniaxial and biaxial (axial-torsional), deep in the inelastic region for aged Inconel 718 at 650°C. Elevated temperature experiments involving multiaxial loading are difficult to perform for two reasons; (1) difficulty in accurate measurement of strains at elevated temperature and (2) the need for such experiments was not felt because no systematic effort was made to determine the individual effects of stress invariants on the inelastic flow of metals. Of course, in the present investigation there is such a requirement in order to capture the SD phenomenon. A comprehensive technique to capture the SD effect by investigating the effect of all the three stress invariants on inelastic deformation is not reported to date.

5.2 Test equipment and Specimen details

An MTS axial-torsional test system was used for the uniaxial and biaxial experiments. A gas based high pressure deformation apparatus was used for testing under hydrostatic pressure. The specimens used for testing have different geometries for each of these systems.

5.2.1 MTS Axial-Torsional test system

The MTS test system (at NASA-Glenn Research Center) is a servo-hydraulic test machine having an axial load capacity of 222500 N and a torque capacity of 2260 N-m. The specimens are gripped by hydraulically actuated grips. Shown in Figure 5.1 is the complete test system with all the required accessories. The top grip of the load frame is attached to an axial-torsional load cell that in turn is attached to the cross head, which remains fixed during

Figure 5.1: MTS Axial-Torsional test system at NASA Glenn Research Center

a test. The bottom grip is attached to an actuator capable of independent rotational and vertical translational motions. The rotation of the actuator can be controlled in a closed loop system by the angle of rotation, torque and shear strain while the vertical motion is controlled by either displacement, load or axial strain. Kalluri and Bonacuse [1990] provide additional details regarding the biaxial test machine.

The test machine is equipped with an adjustable coil (figure 5.2), 50 kW audio frequency, induction heating system capable of generating specimen temperatures up to 800°C. For this reason, the specimen grips are water cooled. The temperature control is done by one thermocouple spot welded to the the specimen at the gage section. The temperature distribution in the gage section is determined by thermocouples which are spot welded to the outer surface of the specimen in the gage section. The temperature variation is limited

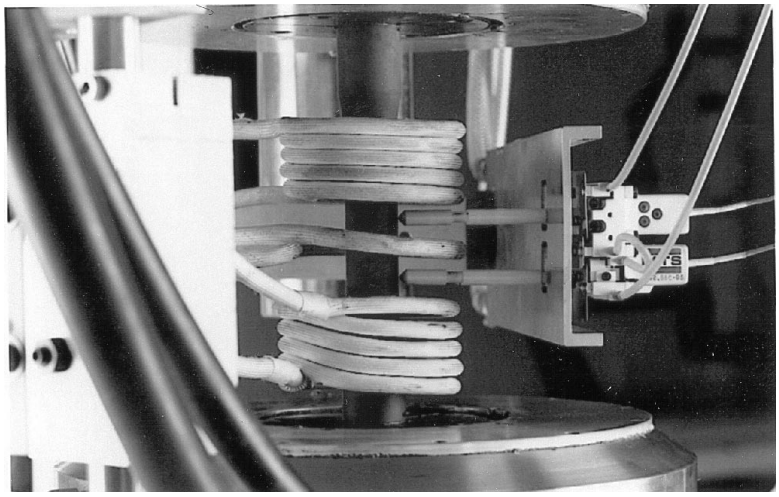

Figure 5.2: Close up showing the specimen, heating coil and extensometer

to ±1% of the target temperature. An enclosure around the test machine limits the effects of air currents. Axial and torsional stress and strain data are saved electronically.

Strain measurement

At high temperatures like 650°C it is not practical to use strain gages. On the other hand, strain measurement with good resolution is required to accurately determine the initiation of yield. At high temperatures extensometers are preferred to strain gages. The common factors that make accurate strain measurement (using extensometer) at high temperatures difficult are (1) presence of electronic noise and (2) coupling between axial and torsional strain components.

A multiaxial extensometer (figure 5.2) that is capable of axial and torsional strain measurements over a wide range of temperatures is used. The extensometer contains two alumina rods spaced 25 mm apart. These are in contact with the specimen by means of indentations on the specimen and spring loading provided by the mounting fixture. The top rod is free to move only in the axial direction while the bottom rod is free to move only in the circumferential direction. Axial displacement δ and angle of twist θ are output voltages. The axial strain is $\epsilon_{11} = \delta/l_o$ and the shear strain is $\gamma_{12} = r_o\theta/l_o$, where r_o is the outer radius of the specimen and l_o is the gage length (25 mm) of the extensometer.

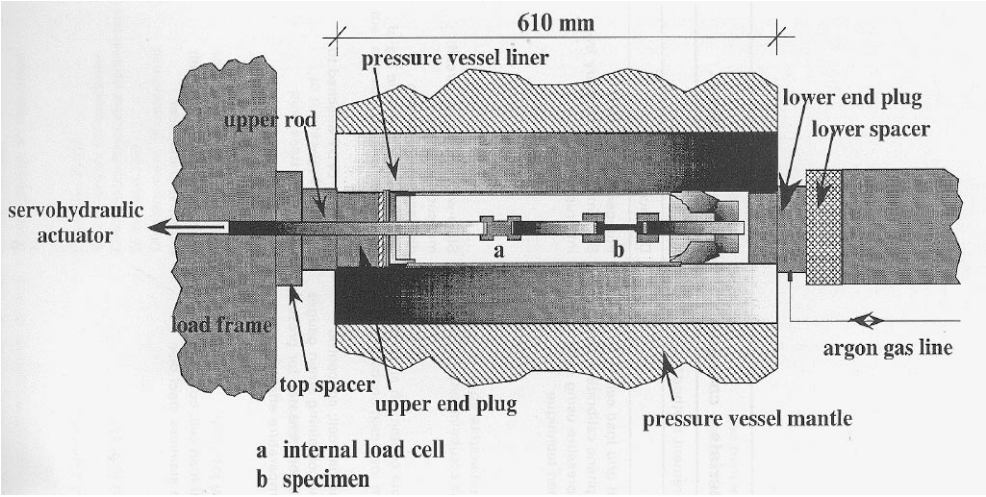

Figure 5.3: Gas based high pressure deformation apparatus

Test machine control

The MTS system is controlled by a microcomputer equipped with a digital-analog (D/A) converter that provides independent controls over the axial and rotational motions of the actuator. A 16-bit analog-digital (A/D) converter is used to acquire load, torque and extensometer (axial and torsional) data. The D/A and A/D hardware is commanded 100 times per second by software that is customized using a FORTRAN program. Two tests were performed using stress control. All other tests in this investigation were performed in strain control.

5.2.2 Pressure test equipment

A schematic diagram for the gas based high pressure deformation apparatus (at Case Western Reserve University (CWRU)) is shown in Figure 5.3. It utilizes a pressure intensifier to generate pressure that is contained within the multi-walled pressure vessel. The volume of the pressurized gas is kept as low as possible because of the danger associated with the stored energy. Pressure is monitored using manganin coil pressure gage that is exposed to the high pressure environment. These coils are used because of the highly reproducible and linear manner in which the coil resistance changes with applied pressure.

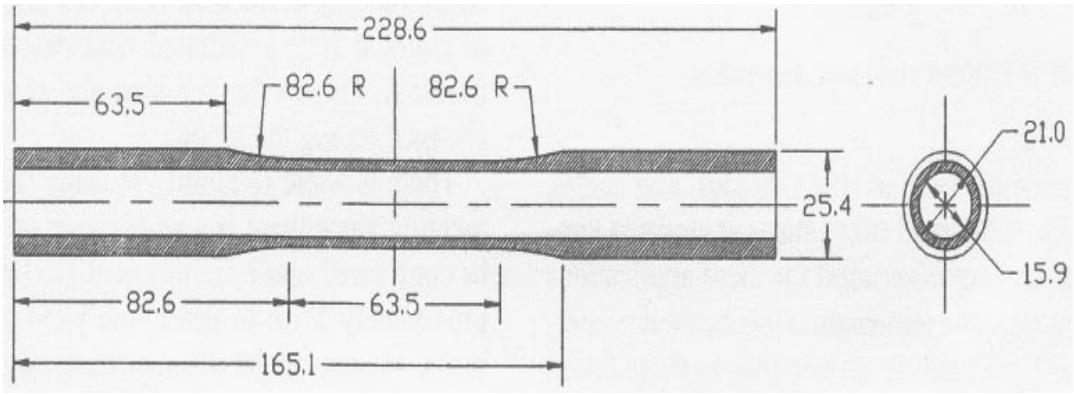

Figure 5.4: Dimensional details of tubular specimens (all dimensions in mm)

The specimen is first inserted in the load train assembly present in the pressure vessel before gas pressurization and then tension or compression is applied at a desired level of superimposed hydrostatic pressure. It is important to continuously monitor the pressure during testing. It is required to accurately monitor the load and displacement during deformation under pressure. For more details on the test system and test procedures, the reader is referred to Lewandowski et al [1998].

5.2.3 Specimen details

Specimens used in the MTS system were thin-walled tubes, designed to achieve a plane state of stress in the gage section. Also, the dimensions are such that loading the gripped ends of the specimen results in a uniform stress distribution in the gage section. The dimensional details of the specimen are given in Figure 5.4.

5.3 Design of Experiments

We have introduced the importance of stress invariants other than J_2 to represent yield and flow behavior for a class of materials that exhibit a SD effect. These invariants are brought into the formulation by simply including them in the threshold function and then deriving the flow and evolutionary laws based on it. Although the chosen form of the threshold function in equation 4.22 is justified for its simplicity and easy reducibility to well known

forms, it is only one of the many possibilities. The appropriate choice of the form may depend on the material under investigation.

A traditional approach for metals would be to conduct hydrostatic tests as suggested by Bridgman [1952]. For pure hydrostatic state of stress (σ), $I_1 = 3\sigma$ and $J_2 = J_3 = 0$. Hence, such a test will help determine whether I_1 affects flow behavior and causes permanent volume change during inelastic deformation. If no permanent deformation is observed under hydrostatic stress, the threshold function can be based on deviatoric invariants alone. Unlike the threshold function for a J_2 material, which can be quantified by pure tensile loading, a simple uniaxial test will be insufficient to quantify a general threshold function. This is because the general yield function has three unknown coefficients, the determination of which requires at least three experiments.

5.3.1 Isolating the effect of invariants

For a general case where I_1 and/or J_3 must be considered, a multiaxial test program needs to be adopted to quantify their relative importance in the definition of yield and flow. This can be accomplished by following stress trajectories that have only one stress invariant that is changing, or better yet, only one nonzero stress invariant. Some simple loadings (external) such as hydrostatic pressure ($I_1 \neq 0$, $J_2 = J_3 = 0$) and pure shear ($J_2 \neq 0$, $I_1 = J_3 = 0$) can help describe the initiation of inelasticity. The internal state of the material does not change during elastic deformation and hence $\tilde{I}_1 = I_1$, $\tilde{J}_2 = J_2$, and $\tilde{J}_3 = J_3$. During inelastic deformation, however, the external loading that causes pure shear or hydrostatic tension are not immediately known. This is because the invariants also depend on the internal stresses which are nonzero during inelastic deformation giving $\tilde{I}_1 \neq I_1$, $\tilde{J}_2 \neq J_2$, and $\tilde{J}_3 \neq J_3$.

For a general loading condition, stress paths having only one changing effective stress invariant can be obtained by following guiding vectors in the effective stress plane determined by the cross product of the gradient of the other two invariants. Mathematically, this can

be expressed as

$$\begin{aligned} \nabla\tilde{J}_2 \times \nabla\tilde{J}_3 &: \tilde{I}_1 \textit{ changing} \\ \nabla\tilde{J}_3 \times \nabla\tilde{I}_1 &: \tilde{J}_2 \textit{ changing} \\ \nabla\tilde{I}_1 \times \nabla\tilde{J}_2 &: \tilde{J}_3 \textit{ changing} \end{aligned} \tag{5.1}$$

where $\tilde{I}_1$, $\tilde{J}_2$ and $\tilde{J}_3$ are effective stress invariants defined previously.

Stress paths obtained by the above equations are greatly influenced by the starting point, which is not required to be the zero stress condition. Effective invariants also depend on the internal stresses, which are neither measurable nor controllable variables. Therefore, computer modeling is necessary to determine what loading to apply in order to follow the guiding vectors in equation 5.1. An additional complexity arises for non-proportional loading for which the applied stress and effective stress directions are generally not the same.

5.3.2 Stress trajectories in three dimensional stress space

Using equations 5.1, a number of stress trajectories can be derived depending on the starting point in the stress space. Figure 5.5(a) shows two stress paths in the principal effective stress space that have both $\tilde{J}_2$ and $\tilde{J}_3$ constant, while Figure 5.5(b) shows the change in $\tilde{I}_1$ along the same stress paths. Note that path AB is hydrostatic tension while path CD is not. However, both paths are straight and have the same direction. Similarly, the case for varying $\tilde{J}_2$ with constant $\tilde{I}_1$ and $\tilde{J}_3$ is shown in Figure 5.6. Again, the importance of the starting point is clearly seen, path AB starts very near the origin and is pure shear while path CD is not. Both AB and CD are straight and parallel but the increase of $\tilde{J}_2$ along CD is larger than that along AB.

Finally, paths for varying $\tilde{J}_3$ with constant $\tilde{I}_1$ and $\tilde{J}_2$ are shown in Figure 5.7. They are neither straight nor do they intersect the origin. Both paths have a local extreme which is expected to cause a distinct change in the inelastic response as the change from loading to unloading occurs.

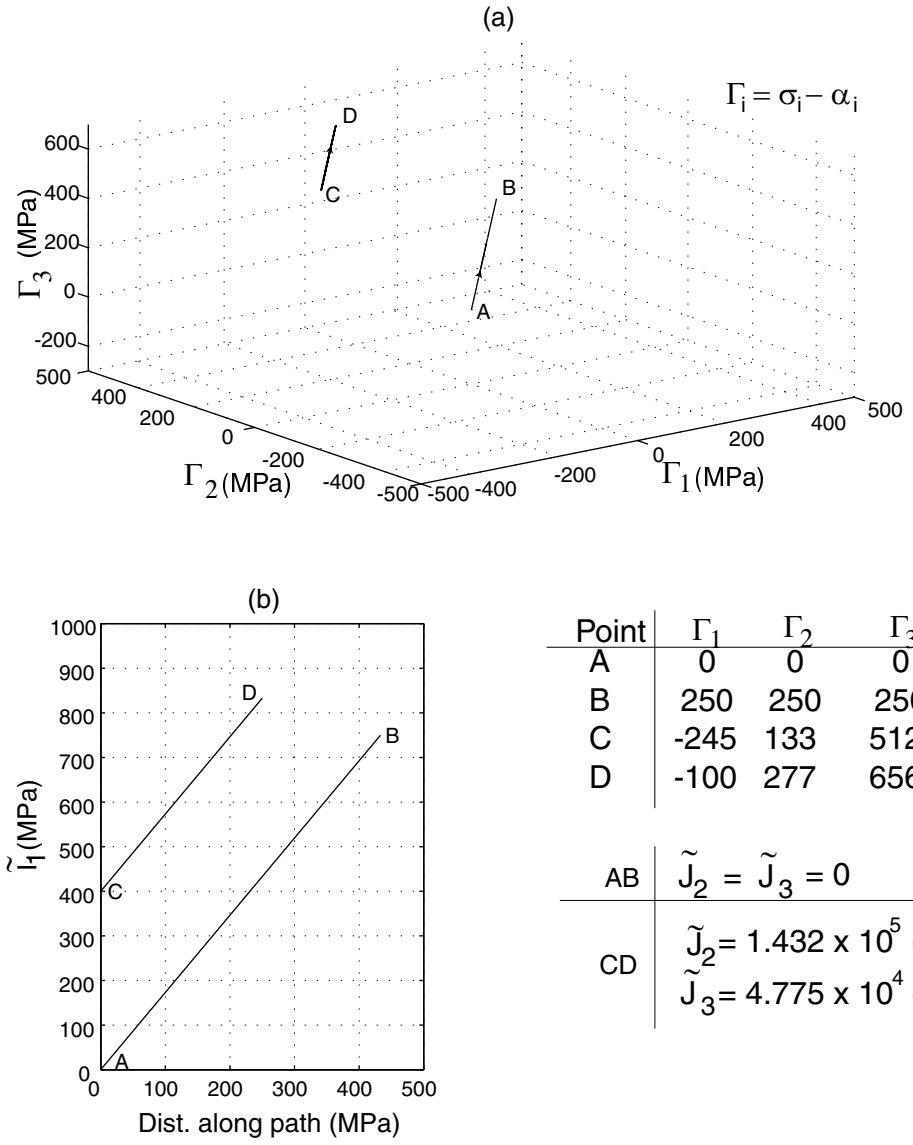

Point	Γ_1	Γ_2	Γ_3
A	0	0	0
B	250	250	250
C	-245	133	512
D	-100	277	656

AB	$\tilde{J}_2 = \tilde{J}_3 = 0$
CD	$\tilde{J}_2 = 1.432 \times 10^5$ (MPa)^2 $\tilde{J}_3 = 4.775 \times 10^4$ (MPa)^3

Figure 5.5: Effective stress paths with $\tilde{I}_1$ changing - $\tilde{J}_2$ and $\tilde{J}_3$ constant

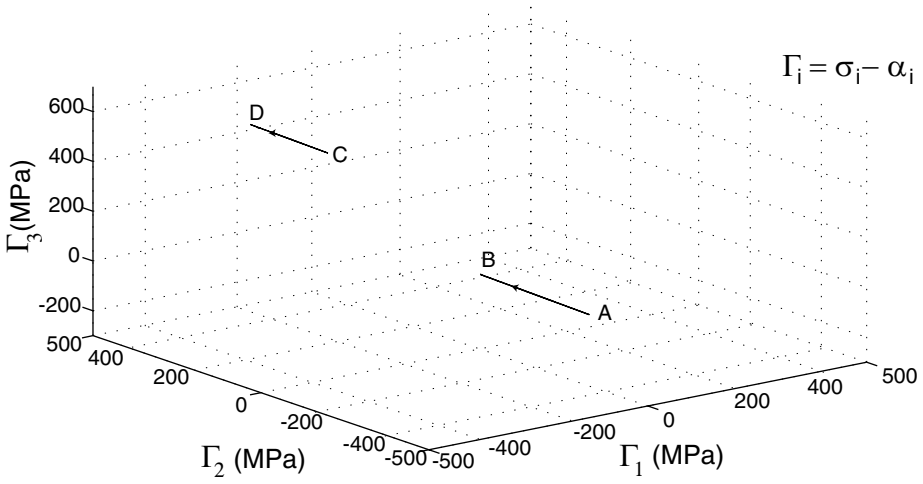

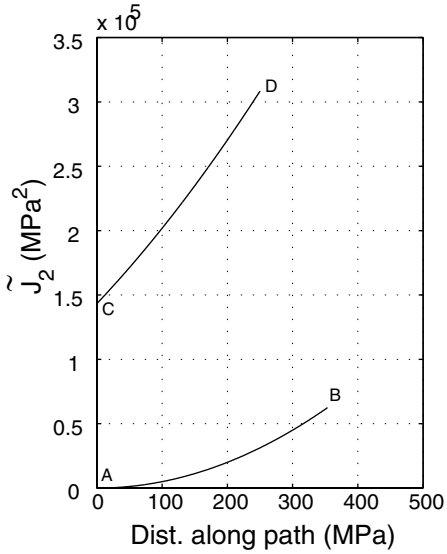

Point	Γ_1	Γ_2	Γ_3
A	1	0	-1
B	250	0	-250
C	-245	133	512
D	-422	133	689

AB	$\tilde{I}_1 = \tilde{J}_3 = 0$
CD	$\tilde{I}_1 = 400$ MPa
	$\tilde{J}_3 = 4.775 \times 10^4$ (MPa)^3

Figure 5.6: Effective stress paths with $\tilde{J}_2$ changing - $\tilde{I}_1$ and $\tilde{J}_3$ constant

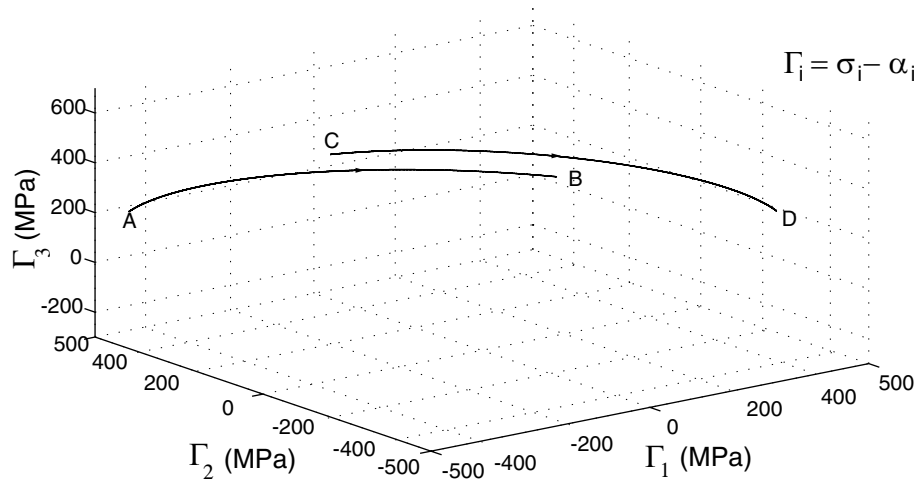

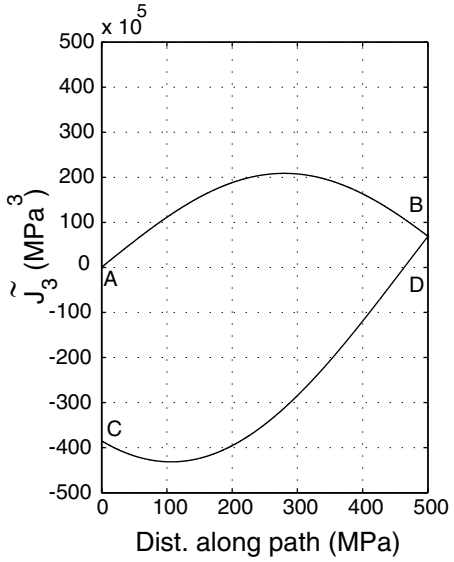

Point	Γ_1	Γ_2	Γ_3
A	-500	400	250
B	-94	-344	588
C	-245	133	512
D	453	-285	231

AB	$\tilde{I}_1 = 150$ MPa $\tilde{J}_2 = 2.325 \times 10^5$ (MPa)^2
CD	$\tilde{I}_1 = 400$ MPa $\tilde{J}_2 = 1.432 \times 10^5$ (MPa)^2

Figure 5.7: Effective stress paths with $\tilde{J}_3$ changing - $\tilde{I}_1$ and $\tilde{J}_2$ constant

Experimentation using three-dimensional stress states require complex laboratory equipment such as that developed by Calloch and Marquis [1999]. Hence, a simpler alternative approach would be to restrict the stress trajectory to a plane stress. Plane stress loading can be readily applied to a thin-walled tube by axial force, torque, and internal pressure. For a plane state of stress however, the invariants are related by

$$J_3 = \frac{I_1}{3}(J_2 - \frac{1}{9}I_1^2) \tag{5.2}$$

resulting in only two of the invariants being independent. Thus a different approach than that for three-dimensional space is needed.

5.3.3 Plane stress experiments

Since $\tilde{J}_2$ has the primary influence on the inelastic flow, it can be treated differently relative to the other two invariants. It is thus proposed that the change in $\tilde{J}_2$ be the same in each of the two tests, one test having a varying $\tilde{I}_1$ and a constant $\tilde{J}_3$ and the other test having a varying $\tilde{J}_3$ and a constant $\tilde{I}_1$. These types of tests appear to be possible using axial-torsional loading of a thin walled tubular specimen.

Simple load paths in the axial-torsional stress space that satisfy the above condition are shown in Figure 5.8 and Figure 5.9. If a pure tensile stress state is chosen as a starting point for shear loading as in Figure 5.8, the result is a constant $\tilde{I}_1$ and a changing $\tilde{J}_3$. If a combined compression-shear stress state is chosen as a starting point and the compressive stress is reduced while the shear stress is increased as in Figure 5.9, $\tilde{J}_3$ remains constant and $\tilde{I}_1$ increases. Though $\tilde{I}_1$ approaches zero, this load path corresponds to loading since the $\tilde{J}_2$ rate is positive in the sense of increasing inelasticity.

The intent of these tests is to facilitate comparison with pure shear tests conducted at an identical $\tilde{J}_2$ rate. Differences in the inelastic strain response could then be attributed to $\tilde{J}_3$ for loading in Figure 5.8 and to $\tilde{I}_1$ in Figure 5.9. This can be used to determine an appropriate weighting of the material parameters a and c in equation 4.22.

Since proportional loading is easier to apply than non-proportional loading, it is worthwhile to consider the proportional load paths shown in Figure 5.10. The loading rate can be adjusted so that the $\tilde{J}_2$ rate is the same for any loading direction, λ_1. For values of λ_1 of

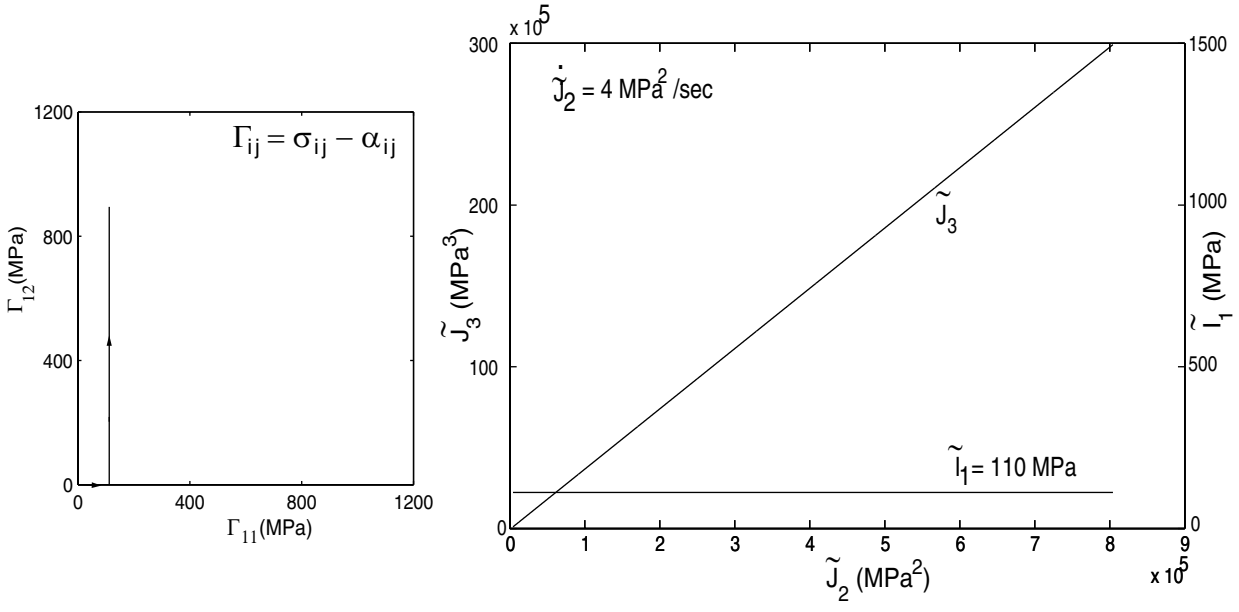

Figure 5.8: Stress path with $\tilde{I}_1$ constant, $\tilde{J}_2$ rate constant and $\tilde{J}_3$ changing

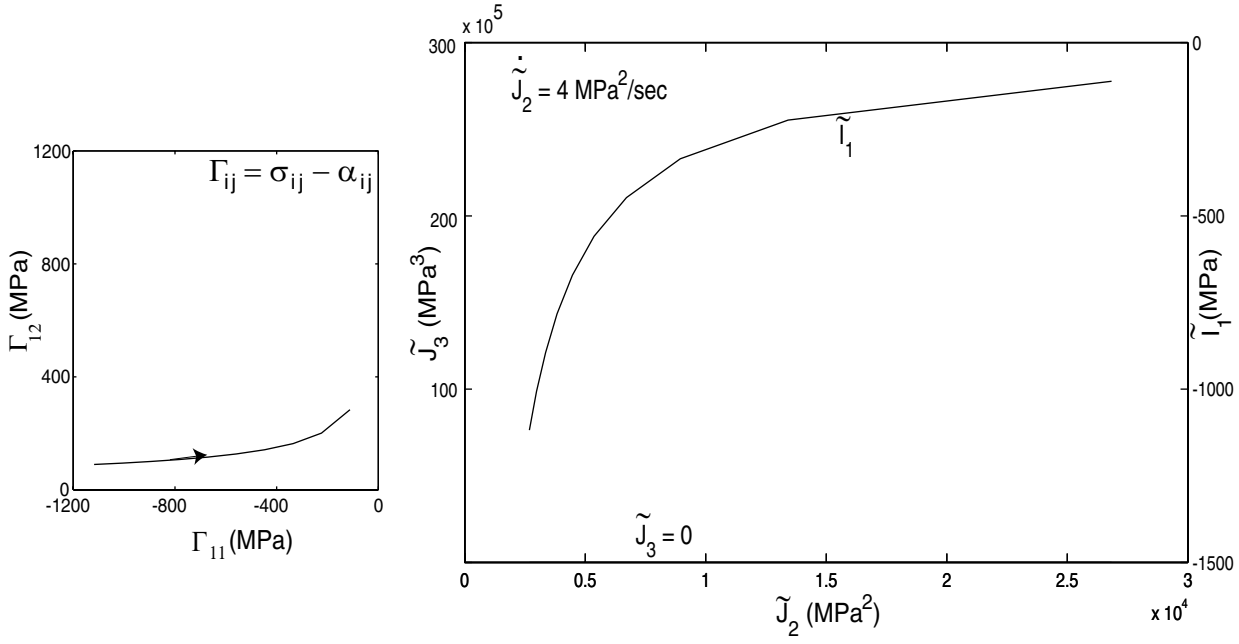

Figure 5.9: Stress path with $\tilde{J}_3$ constant, $\tilde{J}_2$ rate constant and $\tilde{I}_1$ changing

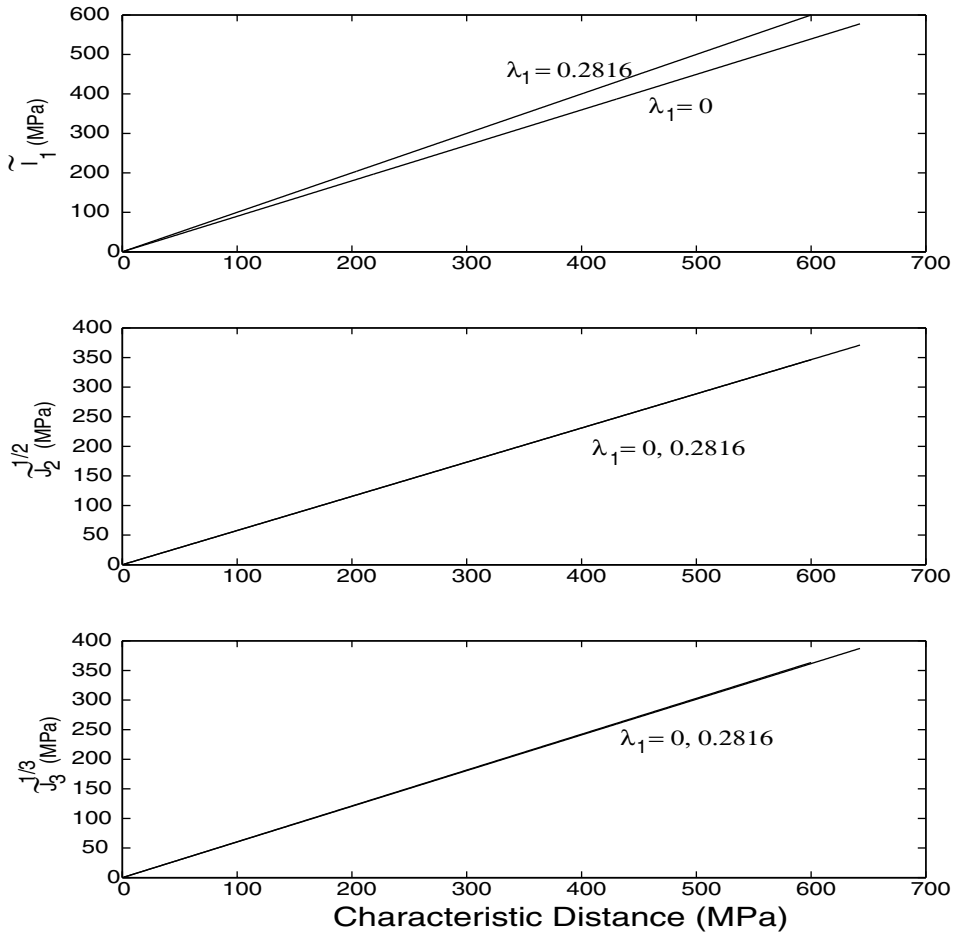

Figure 5.10: Effective stress invariants for two proportional load paths

0.0 and 0.2816, the changes in $\tilde{J}_3$ happen to be almost identical while the change in $\tilde{I}_1$ is not. Thus any difference in the inelastic response could be attributed to $\tilde{I}_1$.

The objective of the various experimental possibilities described above is to determine what effect each of the three stress invariants have on inelastic deformation. These paths can only be determined by using the viscoplastic model to predict inelastic strain and searching for paths that extremize the difference between these forms. It is probable that these paths will require non-proportional loading and creep or relaxation periods.

5.4 Proposed experiments for the current model

First, characterization is done using pure shear tests that are similar to load path AB in Figure 5.6(b). Next, axial test results are used to determine the threshold surface parameters a and c. The intention here is to follow load paths that result in varying $\tilde{I}_1$, $\tilde{J}_2$ and $\tilde{J}_3$, and hence are not similar to any of the paths in Figures 5.5 to 5.10, where the idea was to keep two invariants constant and vary the third.

Validation experiments are biaxial tests using, both proportional and non-proportional loading. The non-proportional loading is similar to the path in Figure 5.8 while the proportional loading is similar to the load paths in Figure 5.10. Tension and compression tests with superimposed hydrostatic pressure complement these validation experiments since they directly show the effect of $\tilde{I}_1$ on material inelasticity. Test matrices are developed for characterization and validation of the proposed viscoplastic model in the next section.

5.5 Test Matrices

The most important and often times the most difficult aspect of modeling at elevated temperature is obtaining the required material parameters. The associated difficulty stems not only from the variety in the mathematical forms of the threshold function, but also from the fact that multiple sets of material parameters can correlate experimental data equally well, for a given load path. In order to arrive at the proper set of material parameters, it is therefore crucial to choose an appropriate set of experiments that bracket a wide range of values for the variables under consideration (e.g. loading rate, load levels, control mode).

First, the test matrix for the pure shear characterization is developed. This is followed by tests in tension and compression. Finally, test matrix for axial testing under hydrostatic pressure is also given. All tests are conducted at 650°C except for the pressure tests, which are at room temperature.

Pure shear characterization

Since we are trying to determine seven material parameters, different types of experiments

Table 5.1: Pure shear characterization experiments

Name	Control	Loading rate	$t_s(sec)$	$t_f(sec)$	End level
IN7	Strain	1745 microstrain/s	10.8	43200	0.0188
IN20	Strain	17.4 microstrain/s	1500	44700	0.0261
IN21	Stress	25.1 MPa/s	22.9	1282	552 MPa
IN22	Stress	25.1 MPa/s	19.5	43200	482 MPa

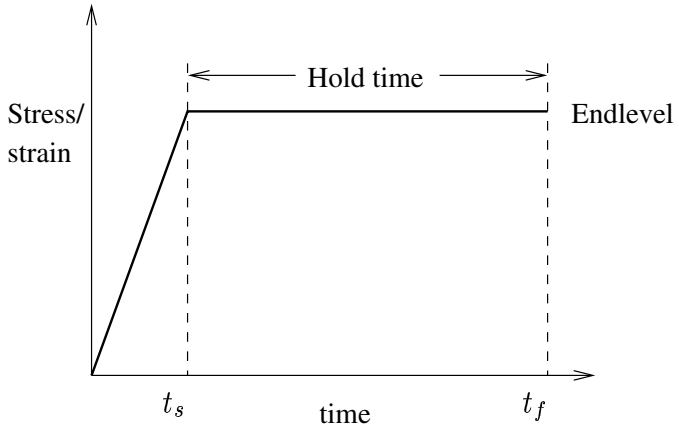

Figure 5.11: Schematic for shear characterization tests

are typically required for proper estimation of these parameters. On this basis, four tests (summarized in Table 5.1) were conducted.

The strain controlled tests were at different loading rates (two orders of magnitude) and have the same end strain level. On the other hand, the stress controlled tests were at the same loading rate but have different end stress levels. All the hold times except for IN21 were approximately 12 hours. A schematic diagram for these tests is shown in Figure 5.11.

Axial tests

Axial tests that will be used to characterize the material parameters a, c and m_1 are summarized in Table 5.2.

Testing under hydrostatic pressure

The intention of these tests is primarily to get a qualitative estimate of the contribution of

Table 5.2: Axial characterization experiments

Type	Control	End level	Time
Tension	Strain	0.02	100 s
Compression	Strain	-0.02	100 s

$\tilde{I}_1$ in the threshold function. Hence, only a few tests are planned which are either tensile or compressive tests under three different values of hydrostatic pressure. These tests are planned to be done at room temperature. The pressures are in the range; 0.1 to 420 MPa.

After obtaining the material parameters using shear and axial characterization, validation of the model is done using biaxial experiments, which are developed in the next chapter.

Chapter 6

Results and Discussion

We have now developed the formulation for a unified viscoplastic model using a generalized threshold function and identified experiments that are required to determine material parameters in the model. The results of the characterization and validation tests are presented in this chapter. The procedure for determination of the material parameters is explained. Once the parameters are determined, biaxial validation tests are compared with model predictions. Results from the tension and compression tests under hydrostatic pressure illustrate the importance of the first stress invariant in the description of inelasticity. Finally, the results are discussed in detail and their implications on the model are described.

6.1 Determination of material parameters

The need for a unified viscoplastic model capable of capturing the SD effect has been established and a generalized theory has been developed. Additionally, an experimental program to characterize the material parameters in the model was developed. In this section, the experimental results are presented starting with pure shear experiments. Using these data, the parameters associated with GVIPS are optimized using the program, Constitutive Material Parameter Estimator (*COMPARE*, Saleeb et al [1998]) and the correlated responses are presented. *COMPARE* optimizes the parameters associated with flow and evolution (κ, n, μ, m, β, R, H). Determination of threshold function parameters (a, b, c, m_1) is done using

axial (tensile and compressive) experimental data. Once all the parameters are determined, the models are put through a rigorous test to verify convexity of the threshold functions.

6.1.1 Experimental results

The pure shear experiments described in Table 5.1 were carried out on aged Inconel 718 at 650°C. A wide range of loading rates and end levels are used in the characterization experiments and hence we can expect to obtain a good estimate of the material parameters.

Results of the pure shear experiments are presented in Figure 6.1 to Figure 6.3. Stress-strain response for monotonic increasing shear strain at two different rates is shown in Figure 6.1. The loading rate for IN7 (1740 microstrain/sec) is two orders of magnitude higher than that for IN20 (17.4 microstrain/sec) resulting in less inelastic deformation in IN7. Hence, the maximum stress level for IN7, in spite of its lower strain level, is higher than IN20. Figure 6.2 shows stress relaxation over 12 hours after loading these two specimens. Stress relaxation is higher for IN7 due to the smaller amount of inelastic deformation that occured during loading relative to IN20. Creep test results are shown in Figure 6.3. Creep strains for IN21 are larger than IN22 because the constant shear stress was higher; 552 MPa compared to 482 MPa (for the same loading rate of 25.1 MPa/sec).

Strain controlled loading is chosen for further uniaxial and biaxial experiments. For this reason, only the strain controlled test results from IN7 and IN20 are used for characterizing the material.

6.1.2 Optimization using *COMPARE*

The size of the data set was reduced to about 12-15 points for each test in order to run the optimization program in a reasonable amount of time (less than approximately two hours). Care was taken in order not to lose essential information provided by these tests. The reduced test data points are shown by circles in Figures 6.4 and 6.5.

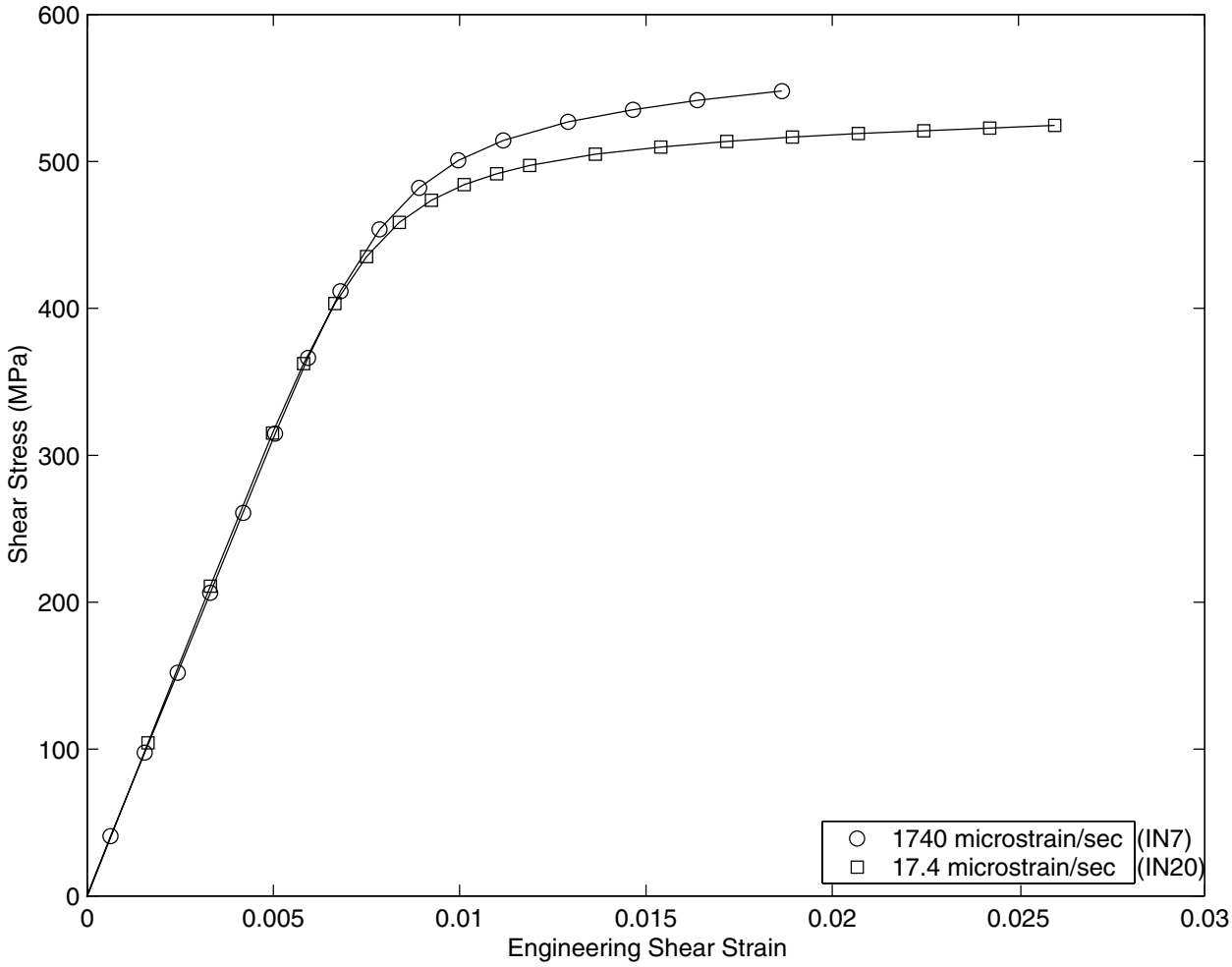

Figure 6.1: Shear stress-strain response

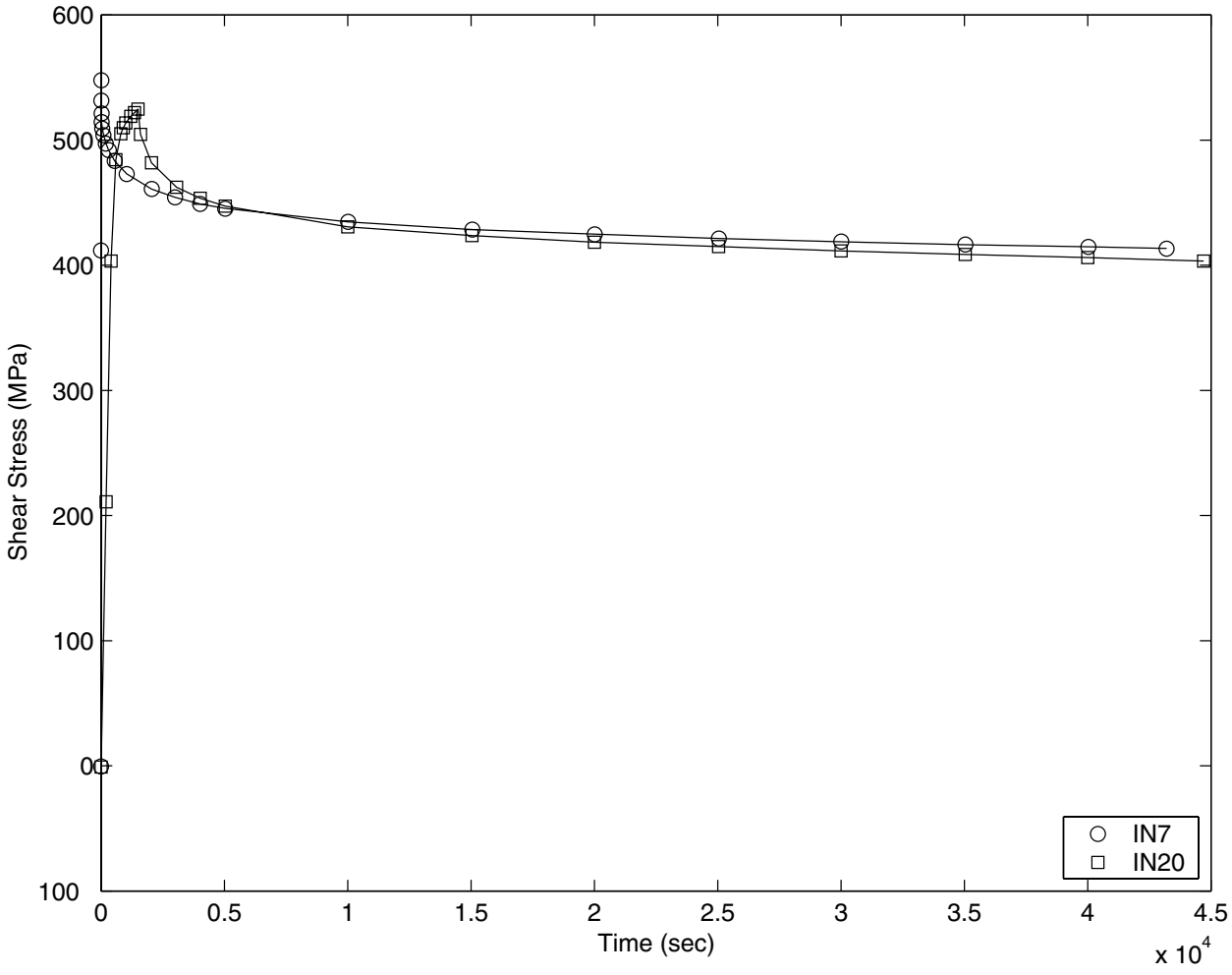

Figure 6.2: Shear stress relaxation

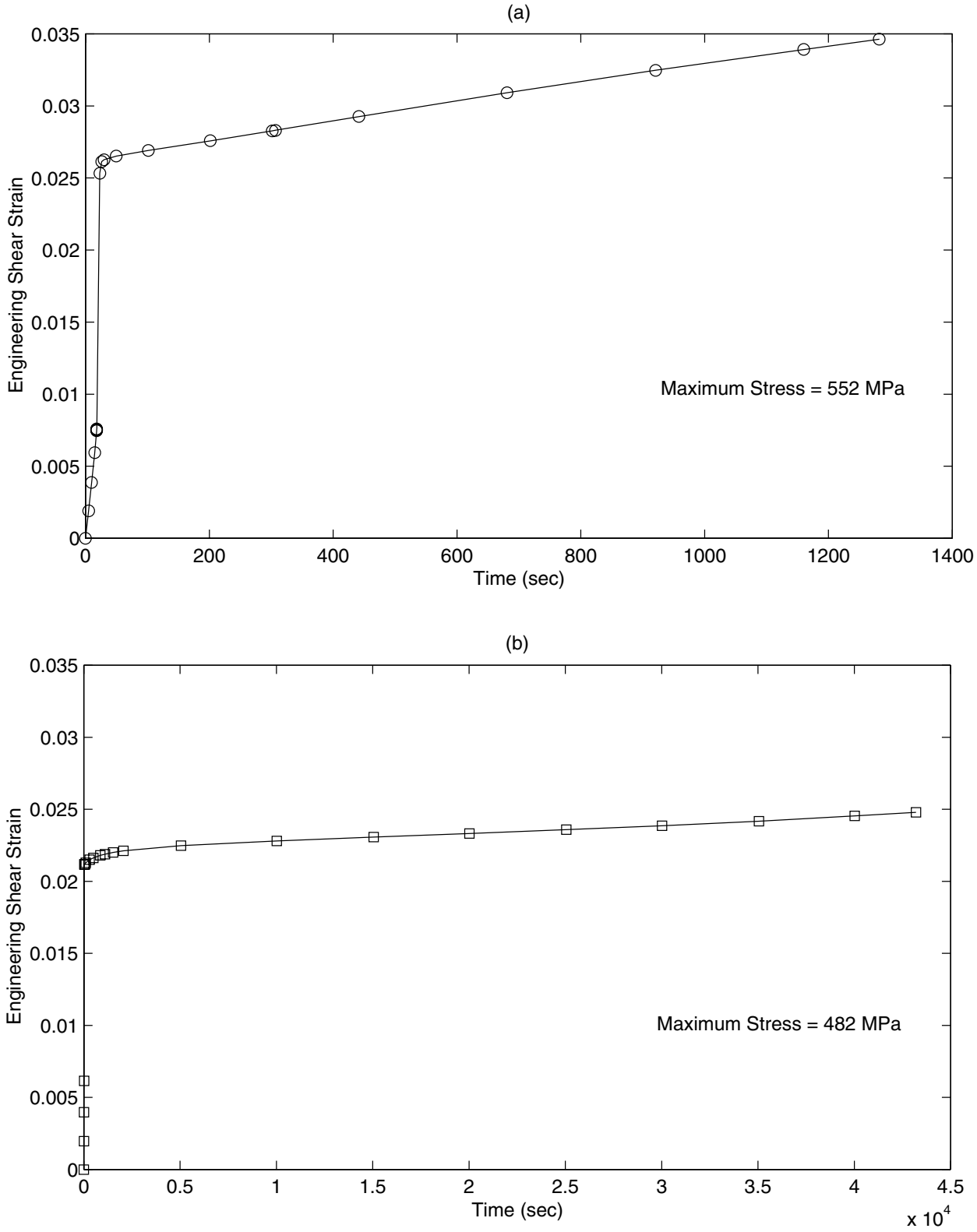

Figure 6.3: Shear loading at 25.1 MPa/sec and creep: (a)IN21 (b)IN22

Table 6.1: Experiments used for shear characterization

Name	Max. Strain	Time to max. strain (sec)	Hold time (sec)	Weights
IN7	0.0188	10.8	-	0.25
IN20	0.025985	1499.2	-	0.25
IN7	0.0188	10.8	43200	0.25
IN20	0.025985	1499.2	43200	0.25

Table 6.2: Elastic constants for aged Inconel 718 at 650°C

E	165360 MPa
ν	0.297
G	63732.5 MPa

The choice and the number of points used in the test data plays an important role in optimizing the material parameters to fit the data. As can be clearly seen, more points are used in the regions of changing slopes. These regions are typically transitions from elastic to inelastic regimes or from monotonic loading to hold.

COMPARE was used to fit the parameters associated with the flow law, hardening, and recovery parameters using these four sets of experimental data. The input data are summarized in Tables 6.1 and 6.2.

An intermediate step was adopted to facilitate optimization of the seven material parameters (κ, n, μ, m, β, R, H). First, only the loading portions of IN7 and IN20 were used with equal weights (0.5) to evaluate all of the parameters (set I, Table 6.3). Next, the complete data sets from IN7 and IN20 (including relaxation) were used to determine another set (set II) of parameters (Table 6.4). When all four tests are used together, the parameters associated with flow law (κ, μ, n) were kept close to set I and those associated with evolution (m, β, R, H) are kept close to set II. Parameters μ, R and H were kept within $\pm$ three decades and parameters κ, n, m and β were kept within $\pm 30\%$. The initial values and bounds in Table 6.5 reflect this approach.

COMPARE successively updated the objective function until it reached a value of 1.0 and

Table 6.3: Optimized values of material parameters (Set I)

Parameter	Final value
κ (MPa)	78.0
n	7.4
μ (MPa-s)	7.0×10^{6}
m	6.8
β	3.8
R (1/s)	3.0×10^{-13}
H (MPa)	4.2×10^{10}

Table 6.4: Optimized values of material parameters (Set II)

Parameter	Final value
κ (MPa)	270.0
n	10.2
μ (MPa-s)	8.0×10^{8}
m	12.0
β	3.05
R (1/s)	6.0×10^{-13}
H (MPa)	2.0×10^{9}

Table 6.5: Material parameters to be optimized

Parameter	Initial value	Lower bound	Optimized Value	Upper bound
κ(MPa)	78.0	60.0	93.447	100.0
n	7.4	5.0	9.445	10.0
μ (MPa-s)	7.0×10^{6}	7.0×10^{3}	6.544×10^{9}	7.0×10^{9}
m	12.0	8.0	9.9	16.0
β	3.05	2.0	3.445	4.0
R (1/s)	6.0×10^{-13}	6.0×10^{-16}	5.787×10^{-15}	6.0×10^{-10}
H (MPa)	2.0×10^{9}	2.0×10^{6}	9.332×10^{8}	2.0×10^{12}

the optimized material parameters are given in Table 6.5. To complete the optimization, *COMPARE* was required to be restarted a few times (typically 3 to 4). Each time the program is restarted, a new (updated) set of initial parameters is used which ensures that the optimization does not stop at a local minimum. The resulting correlation to the experimental data is shown by solid lines in Figure 6.4 and Figure 6.5. There is a good correlation between the model response and the experimental data. It should be noted that predictions from *COMPARE* using the parameters in Table 6.5 for axial loading results in identical stresses in tension (figure 6.6) and compression except for the sign. This is because the threshold function in the *COMPARE* (GVIPS formulation) depends only on J_2.

Figure 6.6 shows that the flow stresses predicted by *COMPARE* are higher than the experimental values for tension and compression. Positive values of either a or c or both result in a decrease in tensile flow stresses and an increase in compressive flow stresses relative to the J_2 model ($a = c = 0$). Hence, it is not possible to start with the optimized parameters in Table 6.5 and get good correlation with tensile and compressive experiments. In order to successfully capture the SD effect, it is required to obtain an axial prediction that is between the tensile and compressive experimental data. Starting with such a J_2 model ($a = c = 0$) we can then capture the SD effect by introducing positive values for a or c or both. To do this, we used an alternative approach to determine the material parameters.

One reason for the over-prediction of flow stresses in tension and compression could be a need for more variety in the experimental data. An attempt to use the stress controlled test data (IN21 and IN22) in addition to those in Table 6.1 did not result in any better correlation with experiments. Even differential weighting of the tests for optimization gave no improvement in prediction. One approach would be to add experiments with different loading rates, hold times, end levels, modes of control (stress or strain) and types of loading (single step or multi-step), in the characterization. However, we restrict additional shear experiments to only one (IN4) and choose an alternative way to characterize the GVIPS parameters.

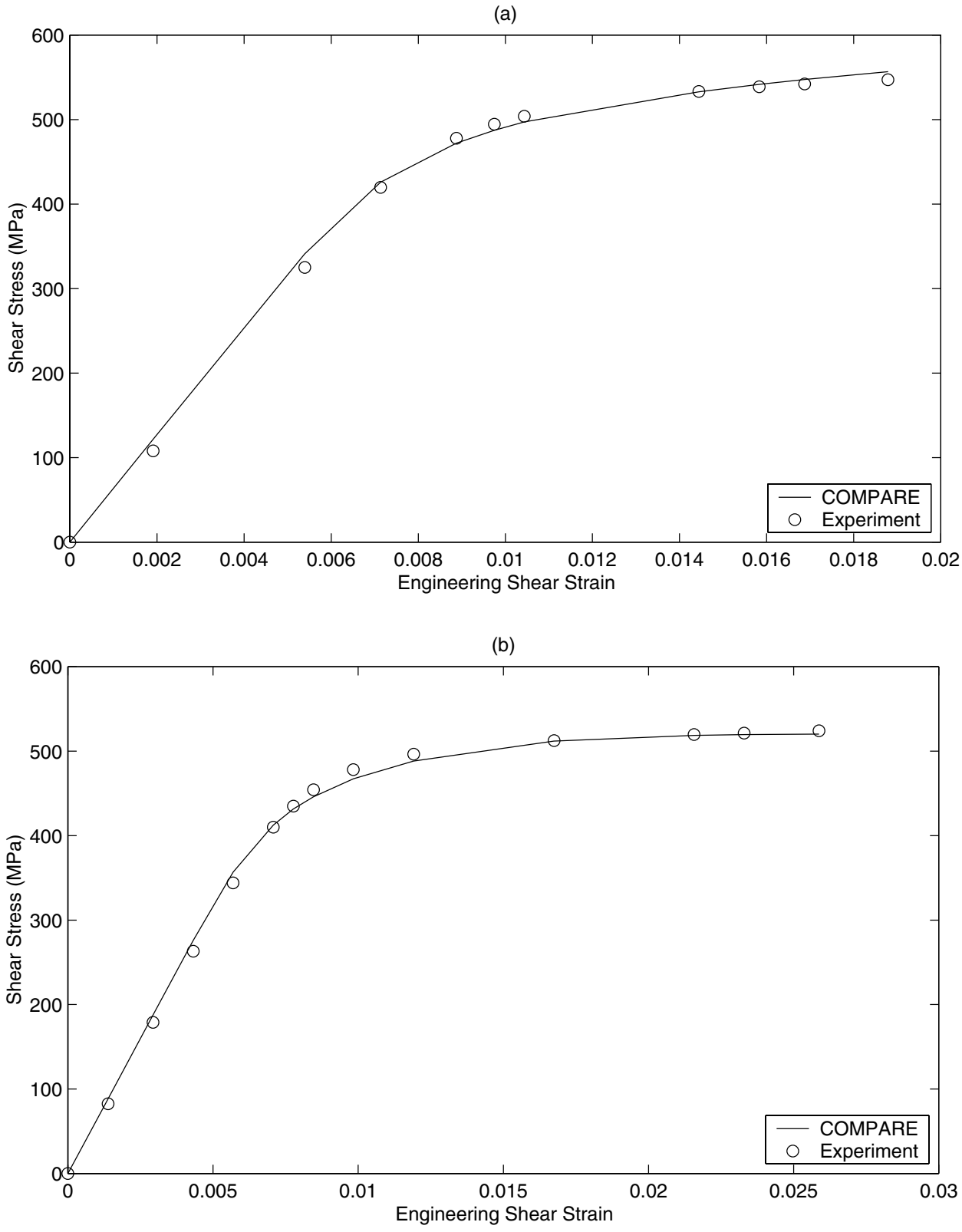

Figure 6.4: *COMPARE* fit for Shear loading: (a)IN7 (b)IN20

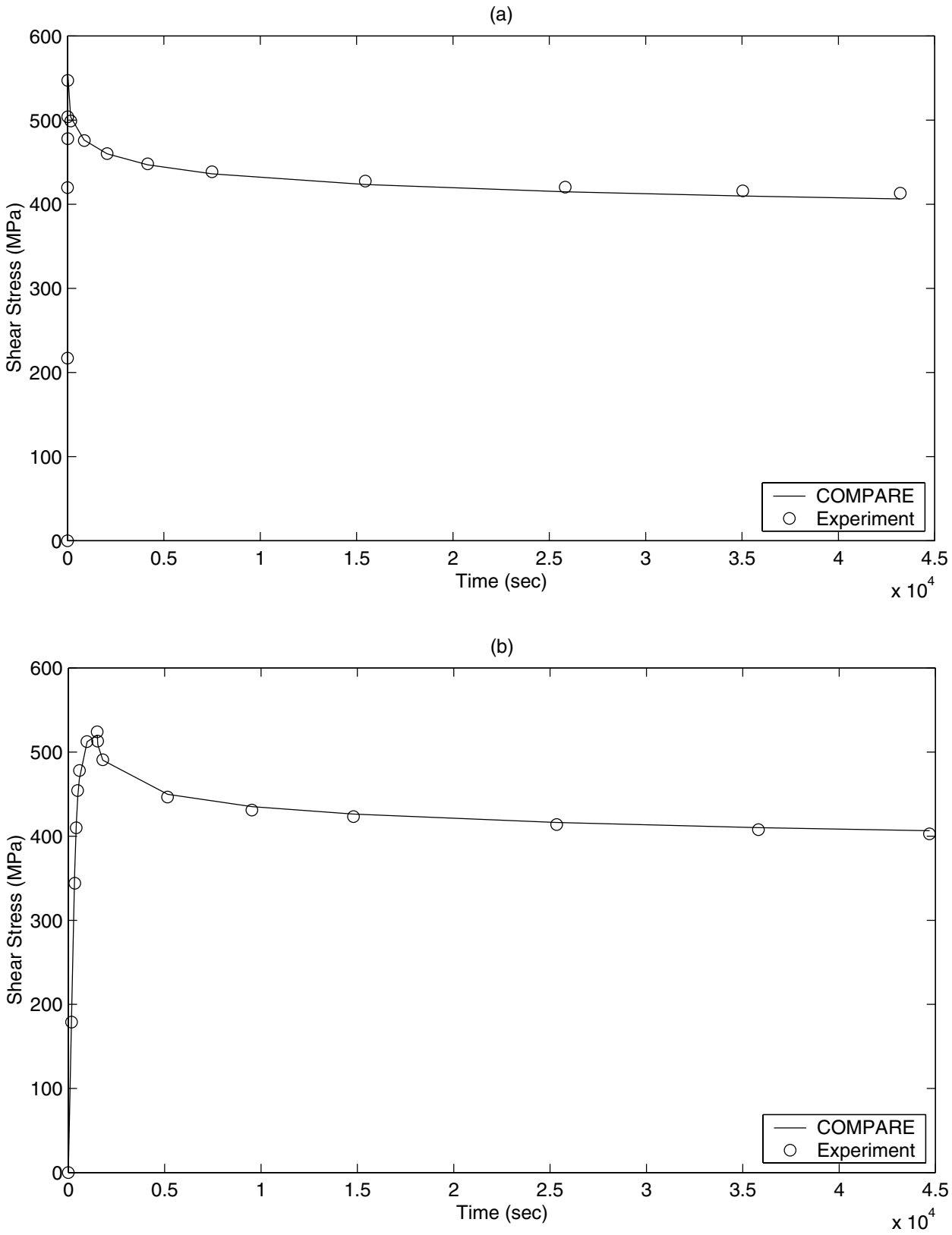

Figure 6.5: *COMPARE* fit for Shear loading and relaxation: (a)IN7 (b)IN20

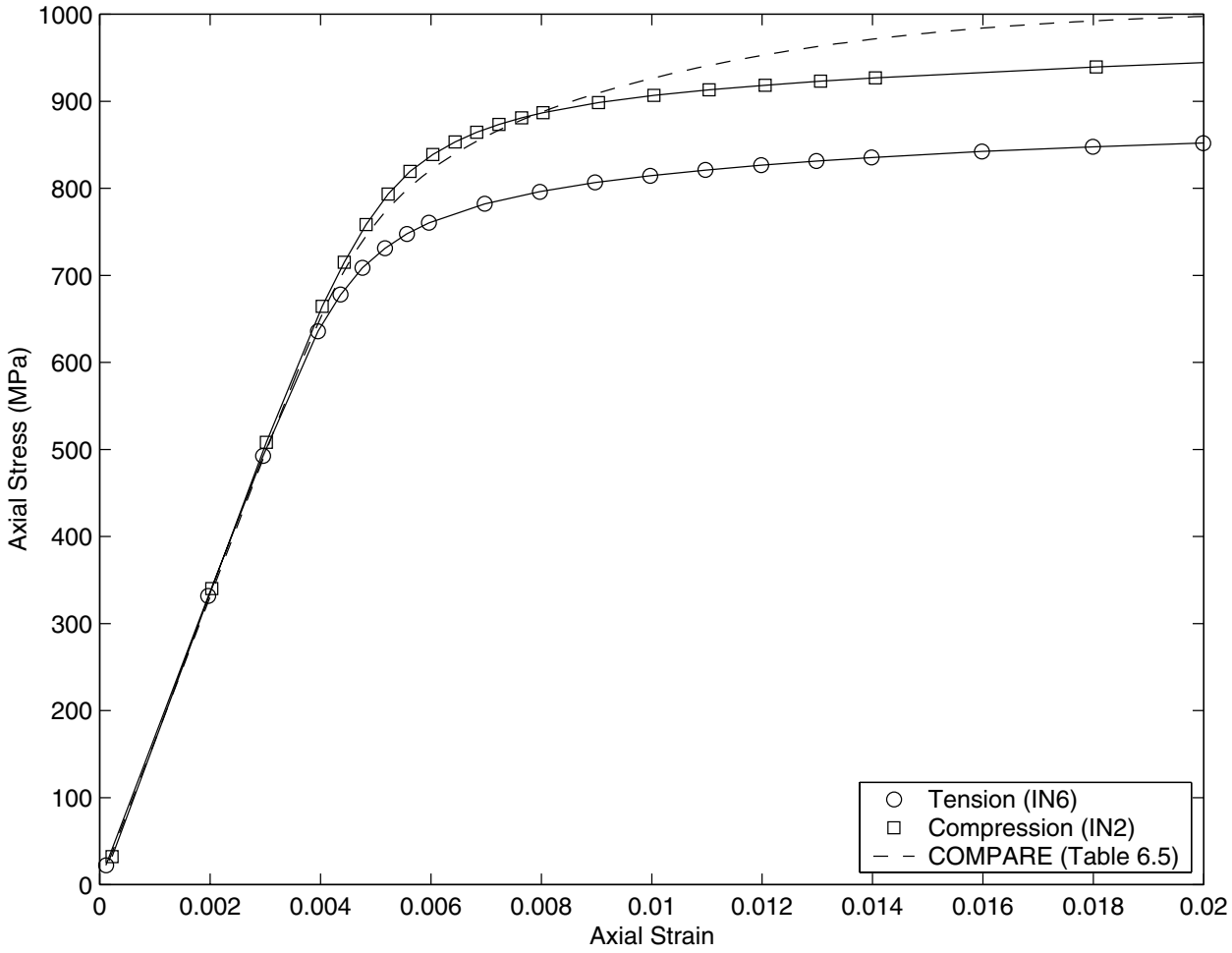

Figure 6.6: Prediction for axial loading: Comparison with IN6 and IN2

Table 6.6: Revised experiments used for characterization

Type	Name	Max. Engineering Strain	Loading time (sec)	Weights
Shear	IN7	0.0188	10.8	0.25
Shear	IN4	0.024	100.0	0.25
Axial	IN6	0.02	100.0	0.4
Axial	IN2	-0.02	100.0	0.1

6.1.3 Alternative approach

A good way to start is to look at the parameters, which had been fit to the experiments purely by a mathematical technique, from a physical viewpoint. The flow law parameters κ (93.447 MPa) and n (9.445) from Table 6.5 seem to be physically unrealistic. κ represents the initial shear yield strength (equation 4.15) and hence should be close to the experimentally determined value of 220 MPa. Parameter n represents rate sensitivity of the material. A large n (9.445) gives large rate-sensitivity, but this is not observed in the experiments. Also, the hardening parameter H (9.332×10^8 MPa), which represents the internal stiffness of the material, should be less than the external stiffness (165360 MPa).

More reasonable values of κ, n and H, used in the optimization, resulted in better comparison with axial test data. However, the predicted axial stress was still not between the tension and compression test data. At this point, it was felt that using different experimental data for the characterization would give better axial response predictions. First, test IN20 was removed from the characterization because its loading rate (17 microstrain/s) was much slower than what is planned for the present investigation (200-300 microstrain/s). Also, since we are not looking at long term relaxation behavior at this point, only the loading part of IN7 was considered. Another strain controlled shear loading test (IN4 shown in Figure 6.7) was added to the data because its loading rate (240 microstrain/sec) is in the 200-300 microstrain/s range. Further, tensile and compressive test data (IN6 and IN2, respectively) are incorporated in the characterization with appropriate weighting. The tests used in the revised *COMPARE* optimization are summarized in Table 6.6. The weights for IN6 and IN2 were developed after a few iterations.

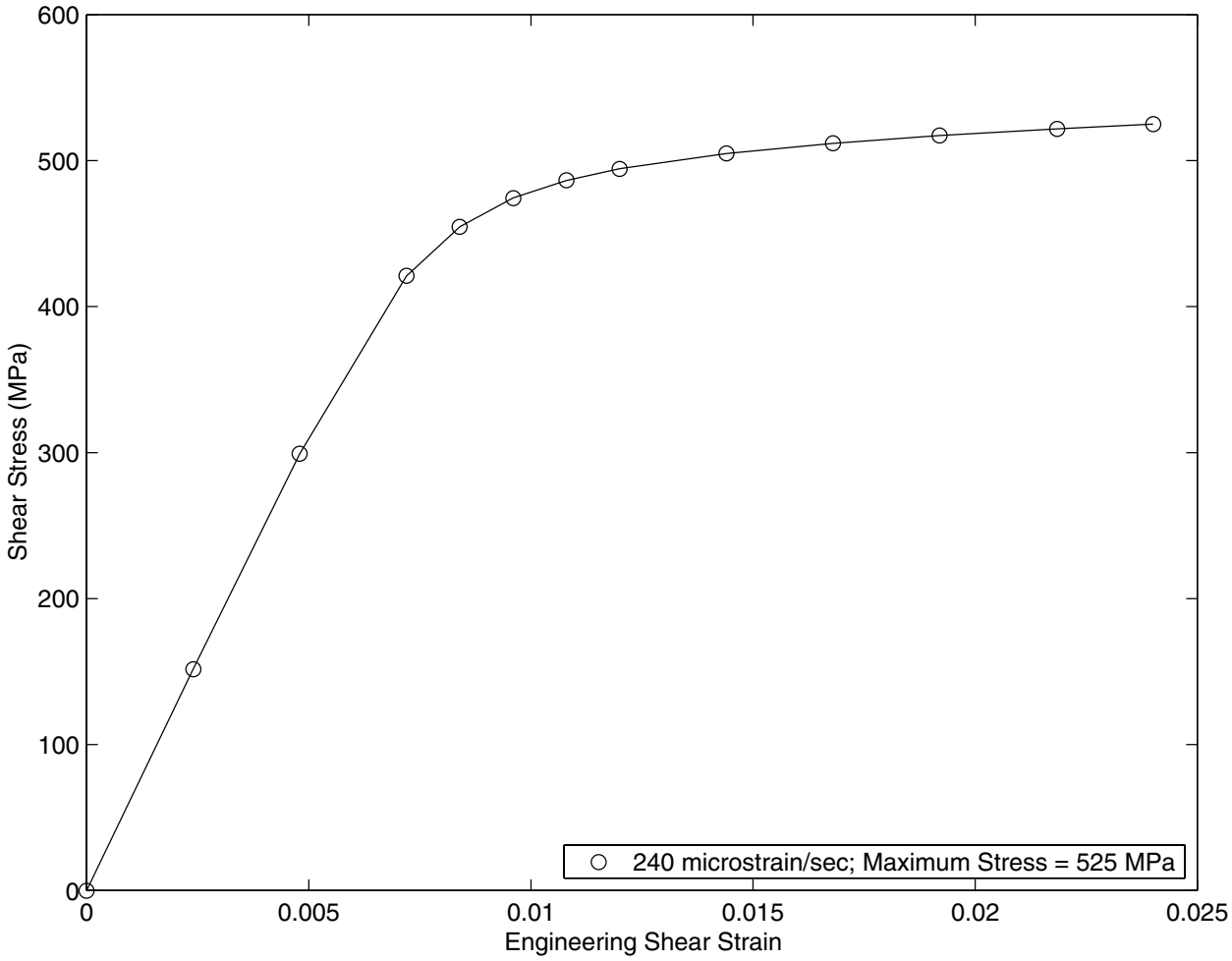

Figure 6.7: Shear stress-strain response (IN4)

Table 6.7: Optimized values using revised tests

Parameter	Final value
κ (MPa)	234.7
n	2.0
μ (MPa-s)	1.7681×10^{5}
m	7.0
β	3.652
R (1/s)	1.0×10^{-12}
H (MPa)	1.966×10^{4}

The corresponding optimized material parameters are given in Table 6.7 and the correlated shear responses are shown in Figure 6.8. The correlation for IN7 is excellent and that for IN4 is reasonable. In addition, the presence of data for IN6 and IN2 in the characterization helped to obtain an axial response that is between the experimental tensile and compressive data (Figure 6.9).

Such a correlation is acceptable because of the following:

1. The value of κ is reasonably close to the shear strength (220 MPa).
2. The lower rate sensitivity observed in experiments is obtained with a lower value of the exponent n (2.0).
3. The internal stiffness parameter H is less than the elastic modulus.

Incorporation of I_1 and J_3 through positive values of a and c will result in more accurate predictions in tension and compression and thus will represent the SD effect. Of course, from this point onwards it is required to use the formulation developed in Chapter 4, which uses a general yield function (we cannot use *COMPARE* anymore). The detailed formulation of the constitutive equations and simplifications for various cases are presented in Appendix A. A FORTRAN program was written to calculate the material response using this generalized formulation and is listed in Appendix B.

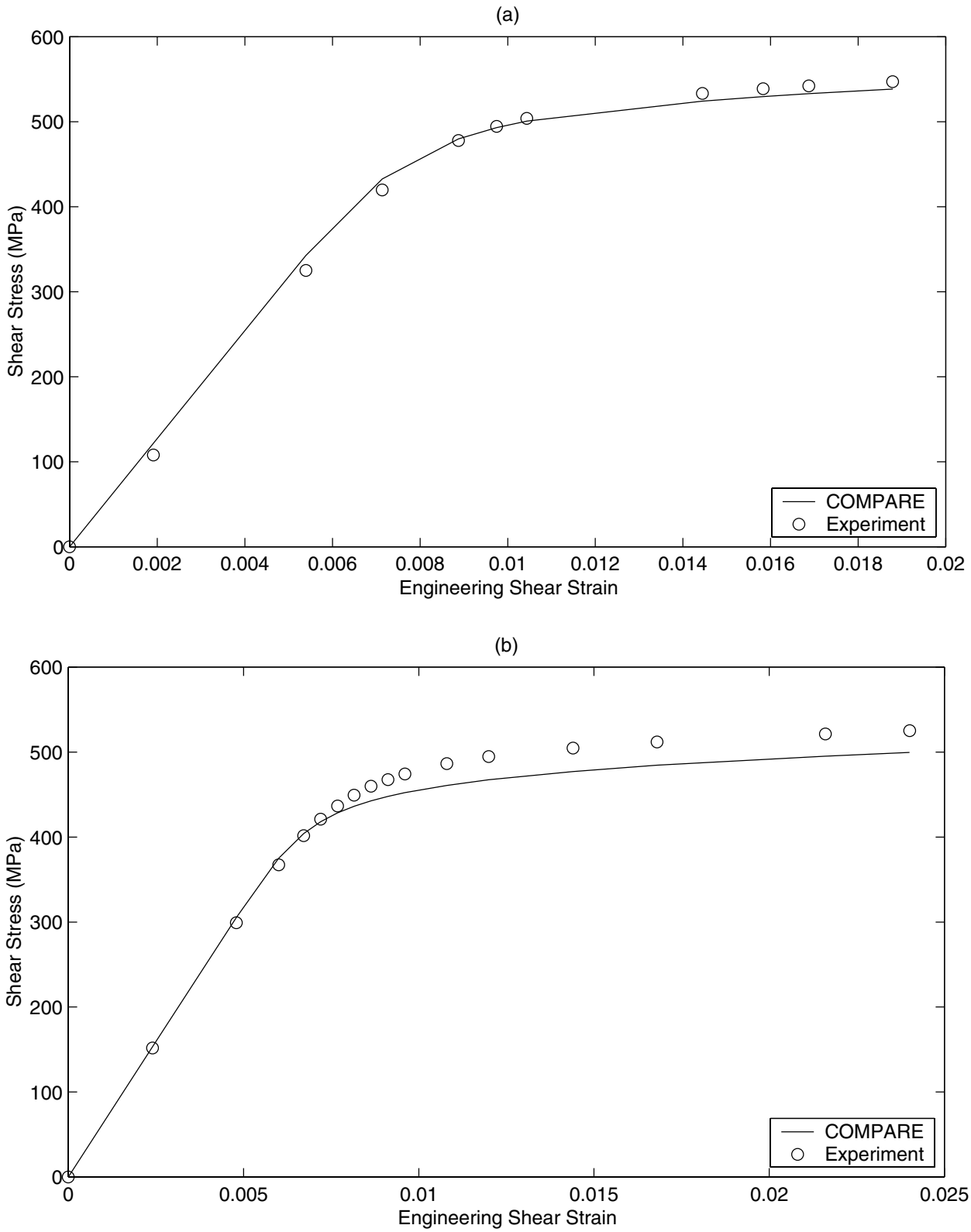

Figure 6.8: Revised predictions for shear loading: (a)IN7 (b)IN4

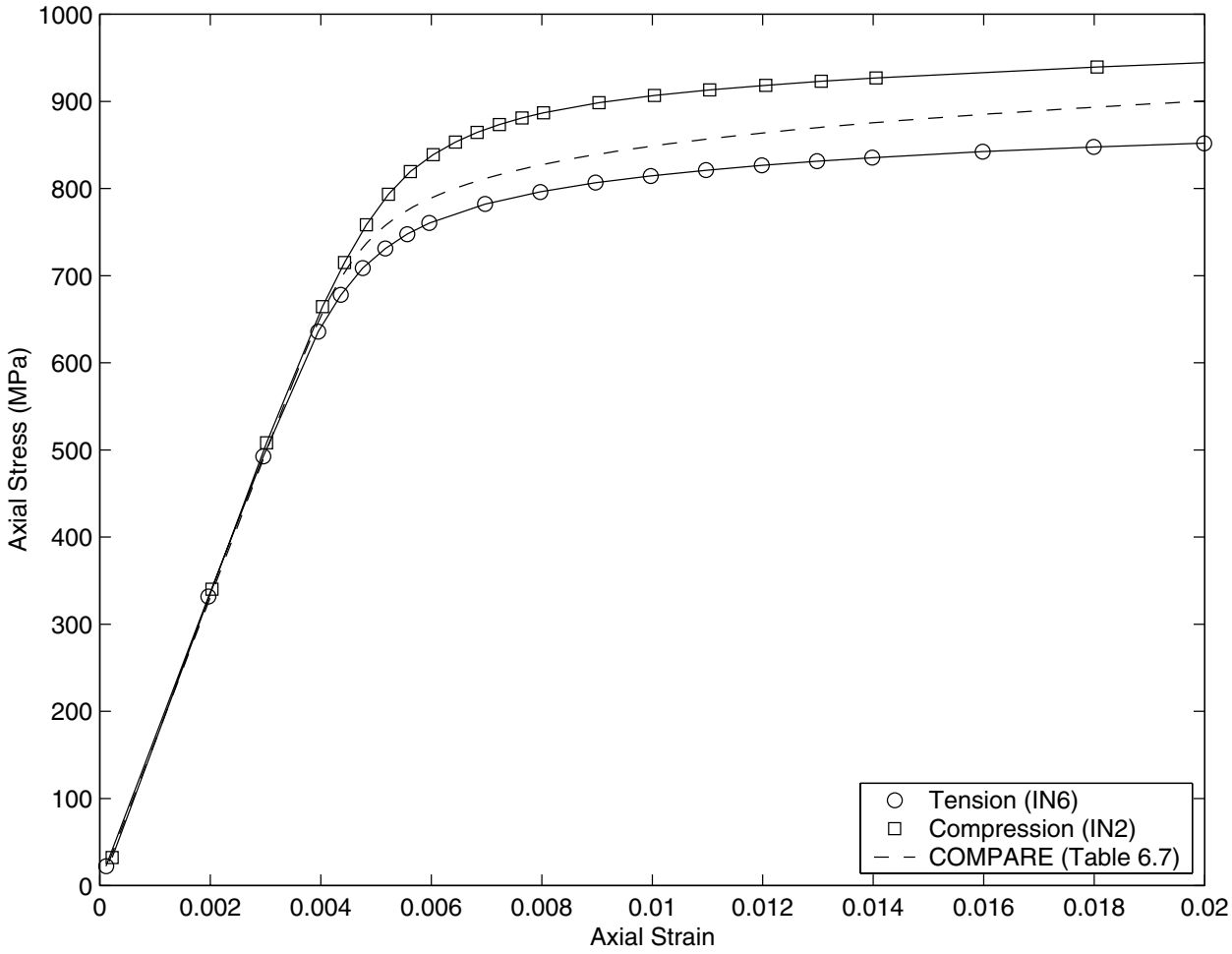

Figure 6.9: Revised correlation for axial loading: Comparison with IN6 and IN2

6.1.4 Axial Characterization

The aim of the axial characterization is to determine the threshold surface parameters a, b, c and m_1, which along with the parameters in Table 6.7 will form the complete parameter set required for the model. First, a value of m_1 is arbitrarily chosen. The parameter b is equivalent to $1/\kappa^{2m_1}$. By doing so, the general threshold function (equation 4.23) reduces to equation 4.15 of the baseline GVIPS model for pure shear loading (I_1=J_3=0). This correspondence is necessary because the parameters in Table 6.7 are based on the GVIPS model (equation 4.15) but are also used in the general formulation. Two values for m_1 (1.0 and 0.6) are investigated. Values of m_1 higher than 1.0 do not significantly improve the axial predictions. Moreover, they result in very small numbers for a and c, which cause numerical difficulties. The values of a and c are varied iteratively until the tensile and compressive flow stresses predicted by the program given in Appendix B correlate well with the experimental data.

For each value of m_1, three combinations of invariants were investigated. These three sets can be classified as

1. I_1J_2 model; c = 0 and a $\neq$ 0
2. J_2J_3 model; a = 0 and c $\neq$ 0
3. $I_1J_2J_3$ model; a $\neq$ 0 and c $\neq$ 0.

The idea of choosing I_1J_2, J_2J_3, and $I_1J_2J_3$ models is to clearly identify the influence of each invariant on the inelastic behavior of the material. The threshold surface parameters are summarized in Table 6.8.

The correlation of the models in Table 6.8 with experimental data is shown in Figure 6.10 and Figure 6.11. Each of these models gives a fairly good correlation of the flow stresses in tension and compression. The point to note here is that all of these models do an excellent job in the prediction of SD especially in the regions of high inelasticity (>1% strain). This was our primary objective.

Before proceeding on to the validation of the models in Table 6.8, we will compare the

Table 6.8: Threshold surface parameters

Name	m_1	$b(1/\text{MPa}^{2m_1})$	$a(1/\text{MPa}^{2m_1})$	$c(1/\text{MPa}^{2m_1})$
J_2	1.0	1.8154×10^{-5}	0	0
I_1J_2	1.0	1.8154×10^{-5}	5.3×10^{-7}	0
J_2J_3	1.0	1.8154×10^{-5}	0	4.5×10^{-6}
$I_1J_2J_3$	1.0	1.8154×10^{-5}	2.6×10^{-7}	2.2×10^{-6}
J_2	0.6	1.43×10^{-3}	0	0
I_1J_2	0.6	1.43×10^{-3}	4.5×10^{-5}	0
J_2J_3	0.6	1.43×10^{-3}	0	1.5×10^{-4}
$I_1J_2J_3$	0.6	1.43×10^{-3}	2.2×10^{-5}	7.0×10^{-5}

initial threshold surfaces with experiment and verify their convexity.

6.1.5 Comparison with experimental threshold surface

The initial threshold surface for aged Inconel 718 at 650°C in the axial-shear plane was determined experimentally by Gil [1999b] using an offset strain definition of 30 microstrain. This is shown by circles in Figure 6.12. The initial threshold surface data is regressed (Miller et al [1990]) to a I_1J_2 function to get the experimental threshold surface shown by + symbols ($m_1 = 1.0$, a = 3.838×10^{-6}, b = 1.8263×10^{-5}). Also plotted are the threshold surfaces predicted by the model using the parameters shown in Table 6.8 for m_1=1.0. Comparison between the predicted and experimental surfaces clearly shows that the models under-predict the tension-compression yield asymmetry.

In aged Inconel 718, the SD starts with a high value, then rapidly decreases and attains a constant value as inelasticity occurs (Iyer and Lissenden [2000b]). We are interested in material behavior as it evolves during inelastic deformation. Thus, we ignore the under-prediction of the SD at flow-initiation as long as the prediction is good at moderate to large inelastic strains. With this in mind, we choose the threshold parameter values in Table 6.8 and ignore the parameter set obtained by regression to the experimental yield surface data. Moreover, use of parameter set obtained by regression under-predicted the flow stresses in both tension and compression.

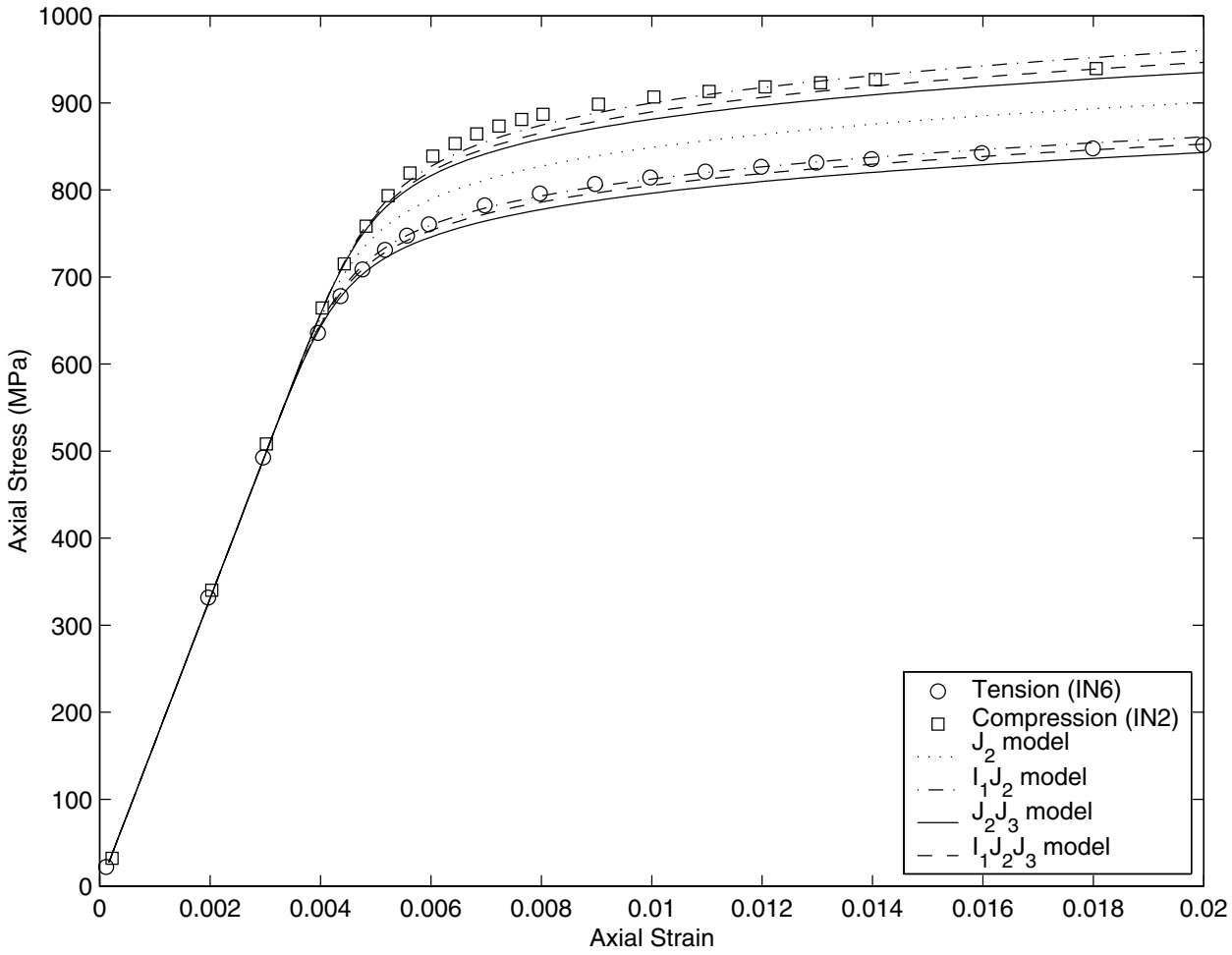

Figure 6.10: Tensile and Compressive loading: Models J_2, I_1J_2, J_2J_3, $I_1J_2J_3$ (m_1=1.0) and Experiments (IN6, IN2)

6.2 Convexity of initial threshold surface

Convexity of the initial threshold surface is a requirement that is a consequence of Drucker's stability postulate. Figure 6.12 shows the initial threshold surfaces for the parameters corresponding to m_1=1.0 in Table 6.8. For m_1=0.6 the surfaces are identical. As the contribution of J_3 increases (value of c relative to a) there appear to be non-convexities appearing at the regions of pure shear. It is difficult to check the convexity of these functions visually. Hence, it needs further attention and a rigorous check of convexity for each parameter set in Table 6.8 is provided in this section.

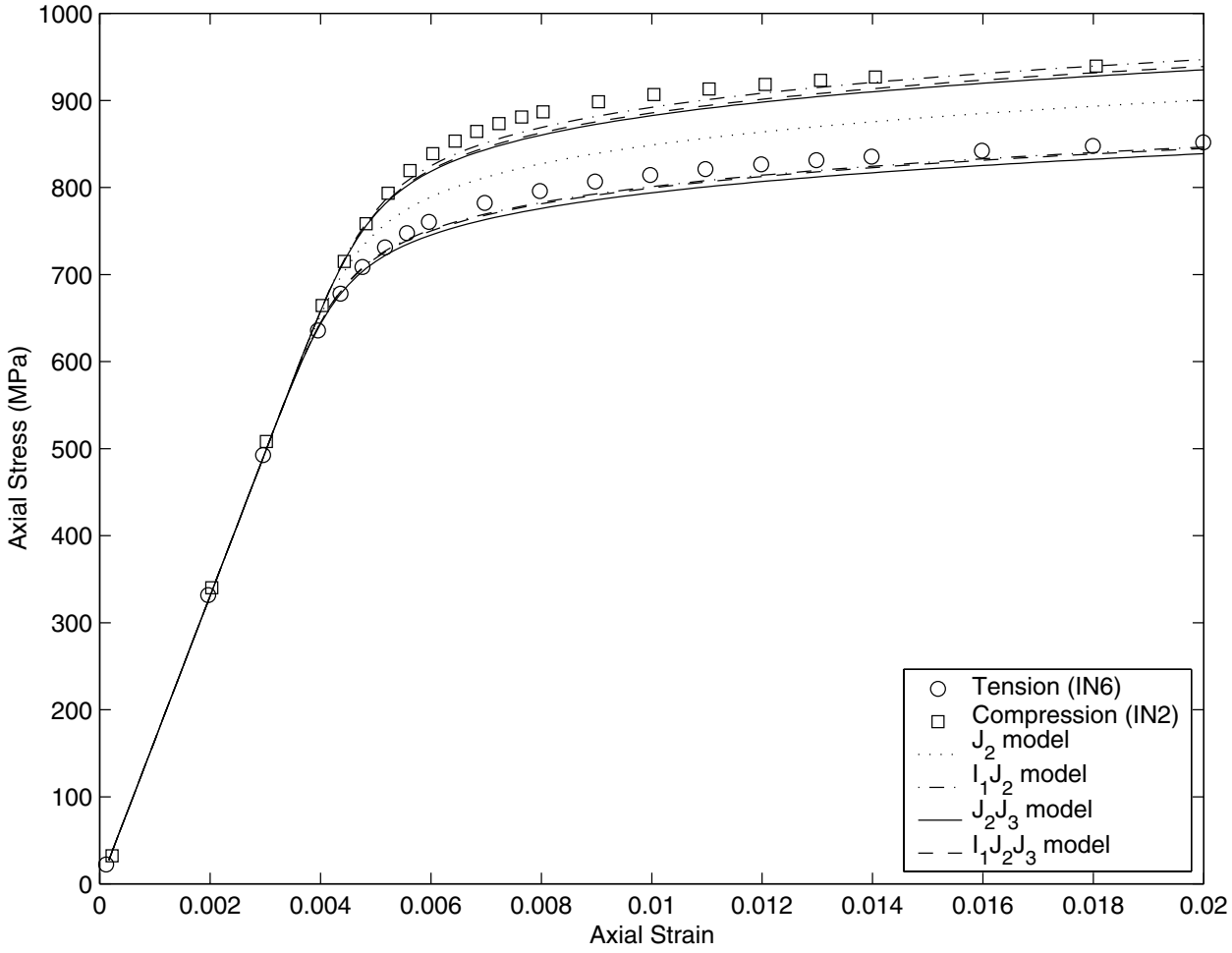

Figure 6.11: Tensile and Compressive loading : Models J_2, I_1J_2, J_2J_3, $I_1J_2J_3$ (m_1=0.6) and Experiments (IN6, IN2)

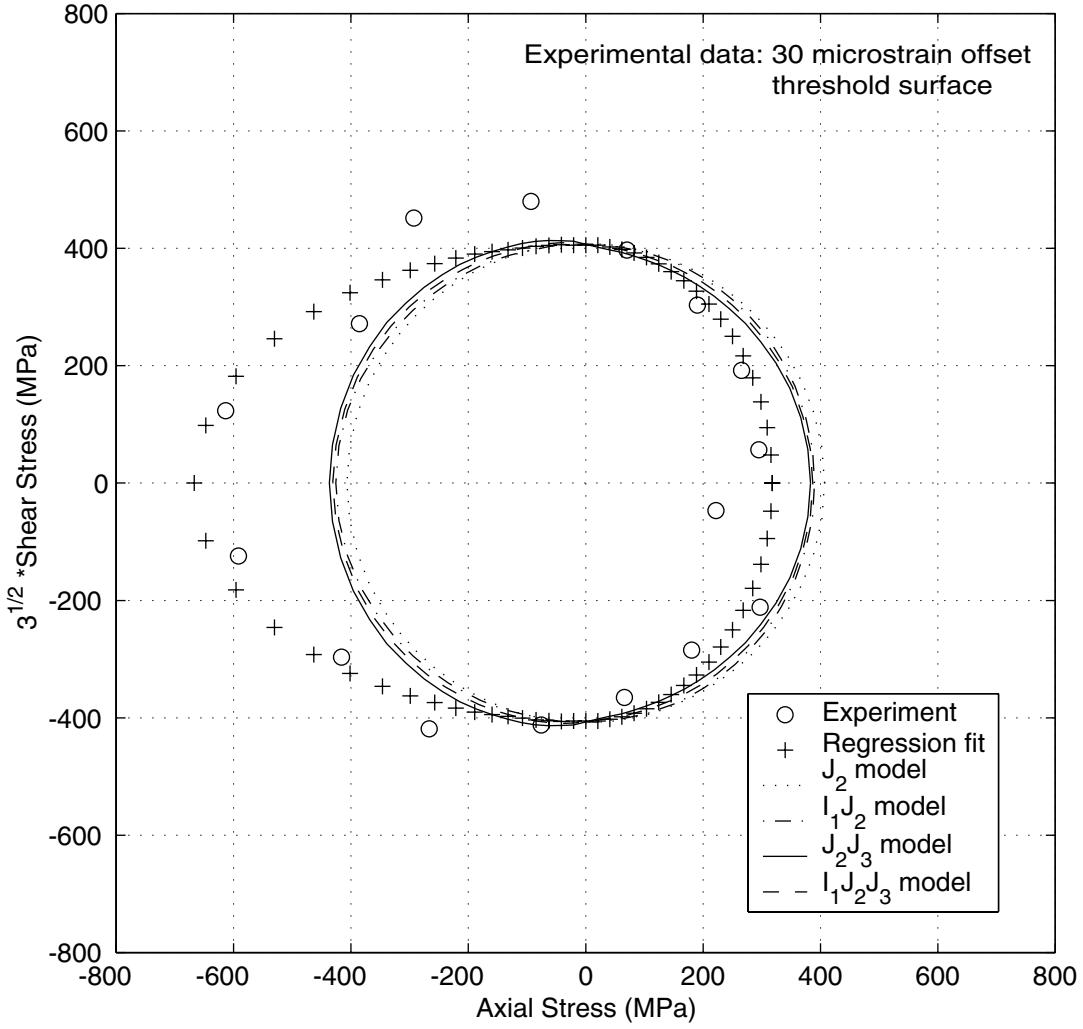

Figure 6.12: Yield surfaces : Models J_2, I_1J_2, J_2J_3, $I_1J_2J_3$ and Experiment

6.2.1 Mathematical Implementation

The objective here is to verify the convexity of the threshold function in three dimensional stress space. We start with the function

$$F = aI_1^{2m_1} + bJ_2^{m_1} + cJ_3^{2m_1/3} - 1 \tag{6.1}$$

and follow the general methodology to check convexity, outlined in chapter 4. For ease of computation the principal stresses (σ_1, σ_2, σ_3) are expressed in terms of the octahedral normal stress (σ_{oct}) and the angle of similarity (θ).

$$\begin{Bmatrix} \sigma_1 \\ \sigma_2 \\ \sigma_3 \end{Bmatrix} = \begin{Bmatrix} \sigma_{oct} \\ \sigma_{oct} \\ \sigma_{oct} \end{Bmatrix} + \frac{2\sqrt{J_2}}{\sqrt{3}} \begin{Bmatrix} \cos\theta \\ \cos(\theta - 2\pi/3) \\ \cos(\theta + 2\pi/3) \end{Bmatrix} \tag{6.2}$$

where

$$\sigma_{oct} = \frac{I_1}{3} \tag{6.3}$$

and

$$\cos 3\theta = \frac{3\sqrt{3}}{2} \frac{J_3}{J_2^{3/2}} \; ; \; 0 \le \theta \le \frac{\pi}{3}. \tag{6.4}$$

J_2 can be expressed in terms of σ_{oct} and θ using equations 6.1, 6.3 and 6.4.

$$J_2 = \left[\frac{1 - a(3\sigma_{oct})^{2m_1}}{b + c(\frac{2}{3\sqrt{3}} \cos 3\theta)^{2m_1/3}} \right]^{1/m_1} . \tag{6.5}$$

Now, substituting equation 6.5 into equation 6.2 we can express principal stresses in terms of just σ_{oct} and θ.

$$\begin{Bmatrix} \sigma_1 \\ \sigma_2 \\ \sigma_3 \end{Bmatrix} = \begin{Bmatrix} \sigma_{oct} \\ \sigma_{oct} \\ \sigma_{oct} \end{Bmatrix} + \frac{2}{\sqrt{3}} \left[\frac{1 - a(3\sigma_{oct})^{2m_1}}{b + c(\frac{2}{3\sqrt{3}} \cos 3\theta)^{2m_1/3}} \right]^{1/2m_1} \begin{Bmatrix} \cos\theta \\ \cos(\theta - 2\pi/3) \\ \cos(\theta + 2\pi/3) \end{Bmatrix}. \tag{6.6}$$

The limits for σ_{oct} can be determined by considering pure hydrostatic tension ($I_1 = 3\sigma, J_2 = J_3 = 0$) and compression ($I_1 = -3\sigma, J_2 = J_3 = 0$). Substituting in equation 6.1 gives the range as

$$\frac{-1}{3a^{1/2m_1}} \le \sigma \le \frac{1}{3a^{1/2m_1}}. \tag{6.7}$$

Now the whole threshold surface is defined by equation 6.1 with σ_{oct} in the range given by equation 6.7 and θ in the range [0,$\pi/3$]. The convexity of F needs to be verified in this range.

The Hessian of F in three dimensional space in matrix form is given by equation 4.32. The first and second partial derivatives of F with respect to the invariants can be expressed as

$$\begin{aligned}
\frac{\partial F}{\partial I_1} &= 2aI_1 \\
\frac{\partial F}{\partial J_2} &= b \\
\frac{\partial F}{\partial J_3} &= \frac{2c}{3} J_3^{-1/3} \\
\frac{\partial^2 F}{\partial {I_1}^2} &= 2a \\
\frac{\partial^2 F}{\partial {J_2}^2} &= 0 \\
\frac{\partial^2 F}{\partial {J_3}^2} &= \frac{-2c}{9} J_3^{-4/3}.
\end{aligned}$$

The derivatives of the stress invariants with respect to the principal stresses can be easily found because the invariants are explicitly expressed in terms of the principal stresses (equations 3.4).

The second partial derivatives of F required for the Hessian can now be computed using

$$\begin{aligned}
\frac{\partial^2 F}{\partial \sigma_i \partial \sigma_j} = \frac{\partial^2 F}{\partial {I_1}^2} \frac{\partial I_1}{\partial \sigma_i} \frac{\partial I_1}{\partial \sigma_j} + \frac{\partial F}{\partial I_1} \frac{\partial^2 I_1}{\partial \sigma_i \partial \sigma_j} + \frac{\partial^2 F}{\partial {J_2}^2} \frac{\partial J_2}{\partial \sigma_i} \frac{\partial J_2}{\partial \sigma_j} \\
+ \frac{\partial F}{\partial J_2} \frac{\partial^2 J_2}{\partial \sigma_i \partial \sigma_j} + \frac{\partial^2 F}{\partial {J_3}^2} \frac{\partial J_3}{\partial \sigma_i} \frac{\partial J_3}{\partial \sigma_j} + \frac{\partial F}{\partial J_3} \frac{\partial^2 J_3}{\partial \sigma_i \partial \sigma_j}
\end{aligned} \tag{6.8}$$

where i and j vary from 1 to 3.

The unit normal vector at any point (σ_1,σ_2,σ_3) on the threshold surface is

$$\hat{n} = \frac{1}{\sqrt{|\frac{\partial F}{\partial \sigma_1}|^2 + |\frac{\partial F}{\partial \sigma_2}|^2 + |\frac{\partial F}{\partial \sigma_3}|^2}} \left[\frac{\partial F}{\partial \sigma_1} \hat{i} + \frac{\partial F}{\partial \sigma_2} \hat{j} + \frac{\partial F}{\partial \sigma_3} \hat{k} \right]. \tag{6.9}$$

As described in Chapter 4, we need to find two basis vectors in the tangent plane by orthonormalizing the unit vectors B, where $B = (\delta_{ij}\text{-}n_i n_j)$. U_{ij} in equation 4.31 is the matrix containing the two basis vectors in the tangent plane. For convexity, the curvature tensor $\aleph_{ij}$ (equation 4.31) must be positive definite at all points on the threshold surface,

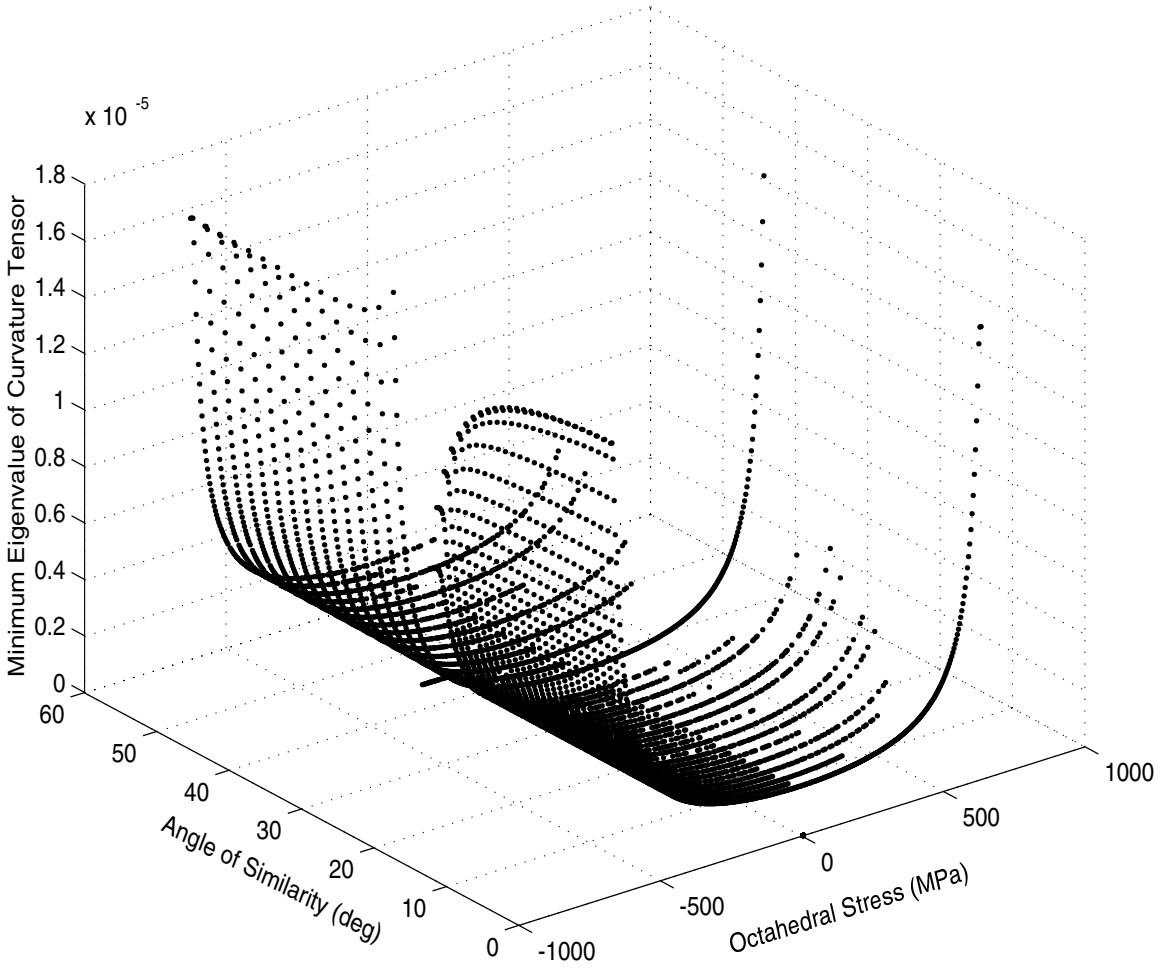

Figure 6.13: Eigenvalues of the curvature tensor ($I_1 J_2 J_3$ model)

which means that the eigenvalues of $\aleph_{ij}$ must be positive. A MATLAB program was written to compute these eigenvalues (Appendix C).

Using the above formulation, a convexity check was performed for all the parameter sets in Table 6.8. Very small increments of angle θ and mean stress σ_{oct} were used in the program to exhaustively probe all the threshold surfaces in three dimensional principal stress space. Resulting eigenvalues corresponding to each point on the threshold surface were positive thereby confirming the positive definiteness of the curvature tensor. Threshold functions for parameters corresponding to m_1=1.0 in Table 6.8 are convex. The minimum eigenvalues of the curvature tensor (for $I_1 J_2 J_3$ model) at discrete points (using intervals of σ_{oct}=4 MPa and θ=2°) are plotted in Figure 6.13.

The convexity of the function in equation 6.1 was first confirmed for the values of a, b and

c (corresponding to m_1=0.6) in Table 6.8. The surface defined by equation 6.1 is observed to be identical to that represented by equation 4.23 and hence convexity of the latter is established.

6.3 Biaxial experiments for validation

The material parameters associated with the flow and evolution (κ, n, μ, m, β, R, H) are given in Table 6.7. At this point, we have six sets of threshold surface parameters (a, b, c, m_1) given in Table 6.8. The focus of this section is the biaxial tests that were used to distinguish between these models and thereby choose the proper set of threshold surface parameters.

Generally, in viscoplastic model development, all material parameters are determined using uniaxial characterization experiments. Then the model is validated by tests which are very different from those used in characterization. These are validation tests that are complicated enough to rigorously test the model.

At this point, we have not conclusively determined the threshold surface parameters. Hence, the intent of the biaxial tests is really two fold; (1) to choose the best set of threshold surface parameters from Table 6.8 and (2) to validate the model.

Biaxial tests were chosen for the following reasons:

1. These tests are very different from the tensile, compressive and shear tests used in characterization.
2. For non-proportional load paths, the inelastic strain rate vector is not always aligned with the loading direction. Hence, such load paths are good tests for the models and are expected to differentiate between their predictive capability.

6.3.1 Test Matrix

Six biaxial tests (IN4, IN5, IN6, IN2, IN11, IN28), schematically shown in Figure 6.14, were performed using strain-controlled axial-torsional loading of aged Inconel 718 tubes at 650°C

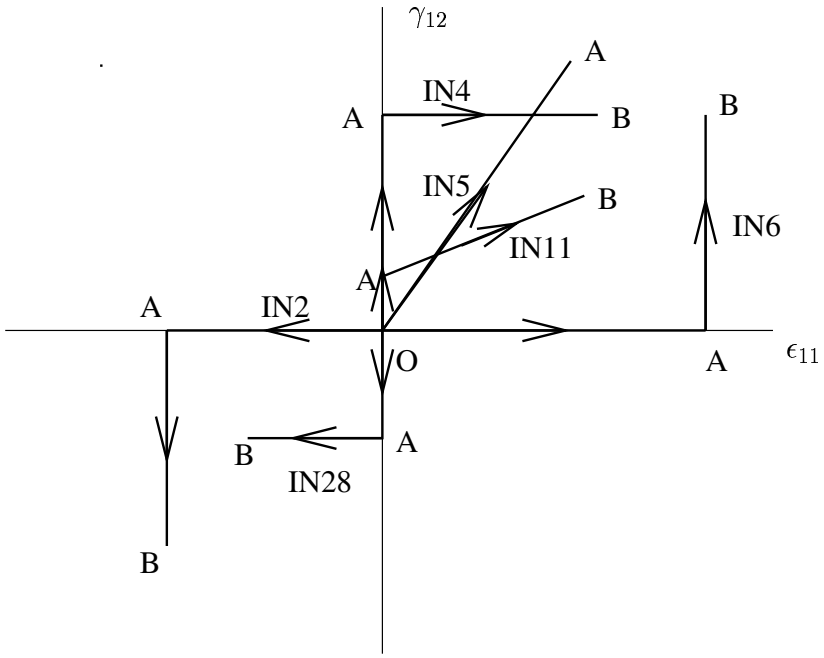

Figure 6.14: Biaxial Experiments

Table 6.9: Test matrix for biaxial experiments

Name	Strain at A (Axial,Shear)	Time (OA) (sec)	Strain at B (Axial,Shear)	Time (AB) (sec)	Type
IN4	(0.0,0.024)	100	(0.02,0.024)	60	shear-tensile
IN5	(0.018,0.03)	94	-	-	proportional
IN6	(0.03,0.0)	150	(0.03,0.024)	60	axial-shear
IN2	(-0.02,0.0)	100	(-0.02,-0.024)	60	compressive-shear
IN11	(0.0,0.0042)	50	(0.02,0.0125)	100	shear-proportional
IN28	(0.0,-0.0109)	130	(-0.015,-0.0109)	75	shear-compressive

(experiments performed by C.J. Lissenden at NASA Glenn Research Center). These tests were chosen such that they have significantly different load paths in the axial-shear stress plane. The loading rates were kept close to the rates used in the characterization tests. The strain levels and corresponding times are shown in Table 6.9. The experimental data points are shown by circles and squares in Figure 6.15 through 6.28. Though many data points were collected only a few are shown to be able to clearly see the comparison with predictions of models in Table 6.8. Both stress-time and stress-strain curves are presented.

6.3.2 Comparison with model predictions

First, models with m_1=1.0 are used to predict stress histories for IN4, IN5, IN6, and IN2 (Figures 6.15 to 6.24). This section presents and discusses the comparison between model predictions and experimental results.

Shear-tensile loading (IN4)

Figures 6.15 and 6.16 show the comparison between experiments and model predictions. The shear stress predictions during shear loading are identical for I_1J_2, J_2J_3, and $I_1J_2J_3$ models. This is expected because I_1 and J_3 remain zero for shear loading. For the subsequent axial loading there is a significant difference in axial stresses predicted by these models. Experimental data for axial stress is best predicted by the J_2J_3 and $I_1J_2J_3$ models. The J_2 model over-predicts the axial stresses and so does the I_1J_2 model. The drop in shear stress during axial loading is slightly overestimated by all of the models.

Proportional loading (IN5)

Axial and shear stresses for the proportional loading are shown in Figures 6.17 and 6.18. The J_2 model over-predicts both the axial and shear stresses. Axial stresses are under-predicted by I_1J_2, J_2J_3, and $I_1J_2J_3$ models and there is no significant difference between the predictions. Shear stresses show a moderate difference in model predictions. The I_1J_2 model predicts even higher shear stresses than the J_2 model. The $I_1J_2J_3$ model predicts marginally better than J_2 model. The J_2J_3 model gives the best prediction of shear stresses.

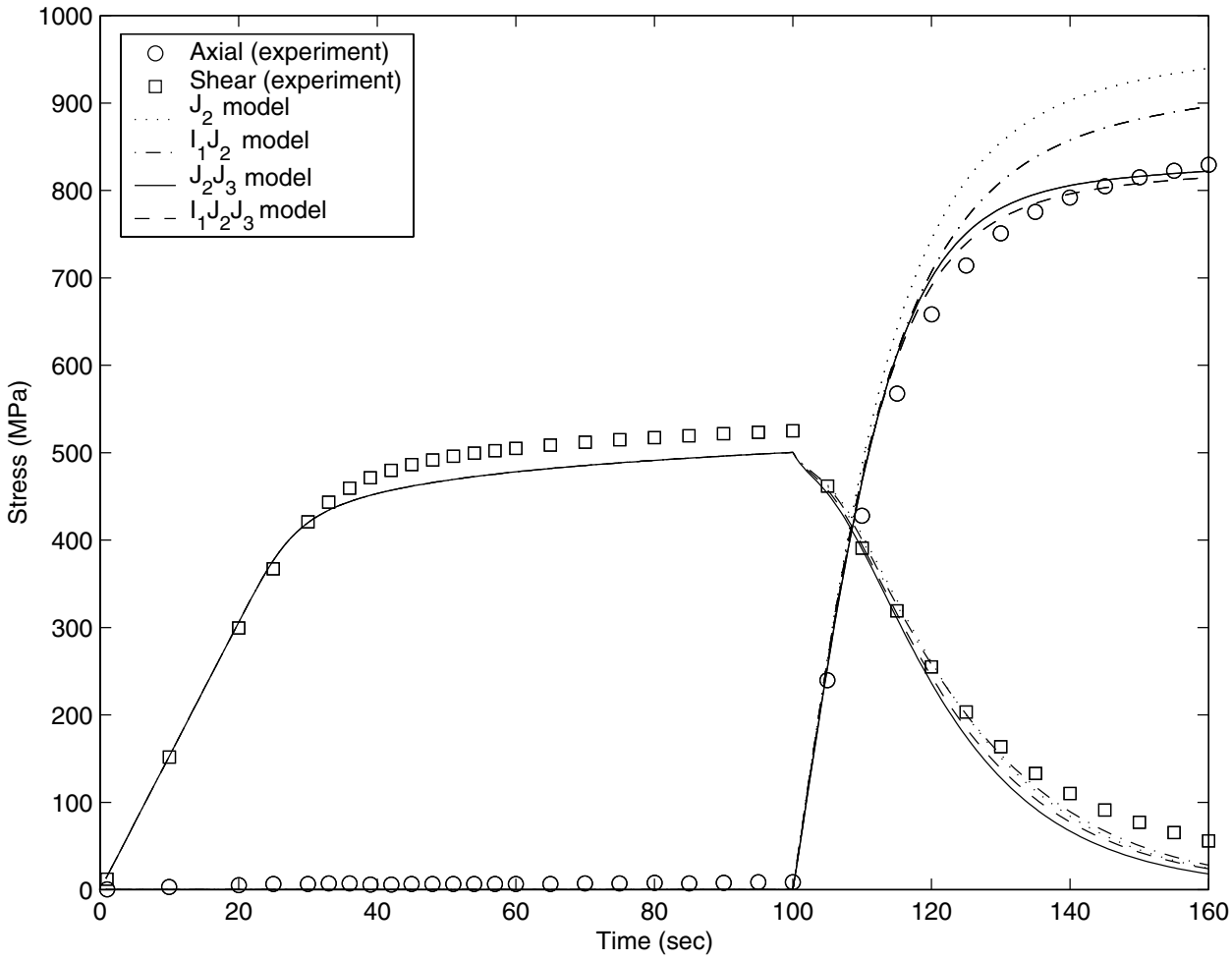

Figure 6.15: Shear-tensile loading (IN4): Stress-time response ($m_1 = 1.0$)

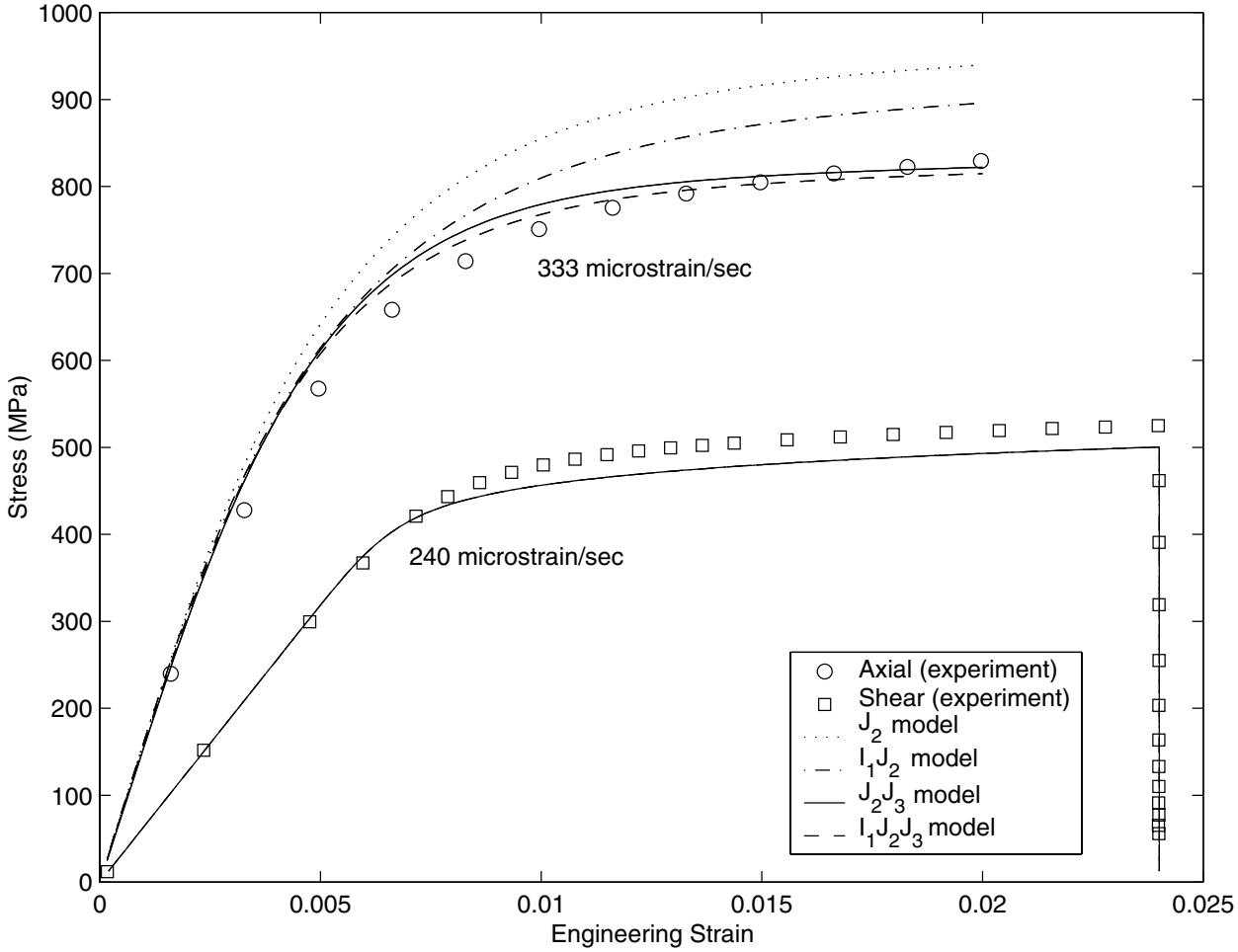

Figure 6.16: Shear-tensile loading (IN4): Stress-strain response ($m_1 = 1.0$)

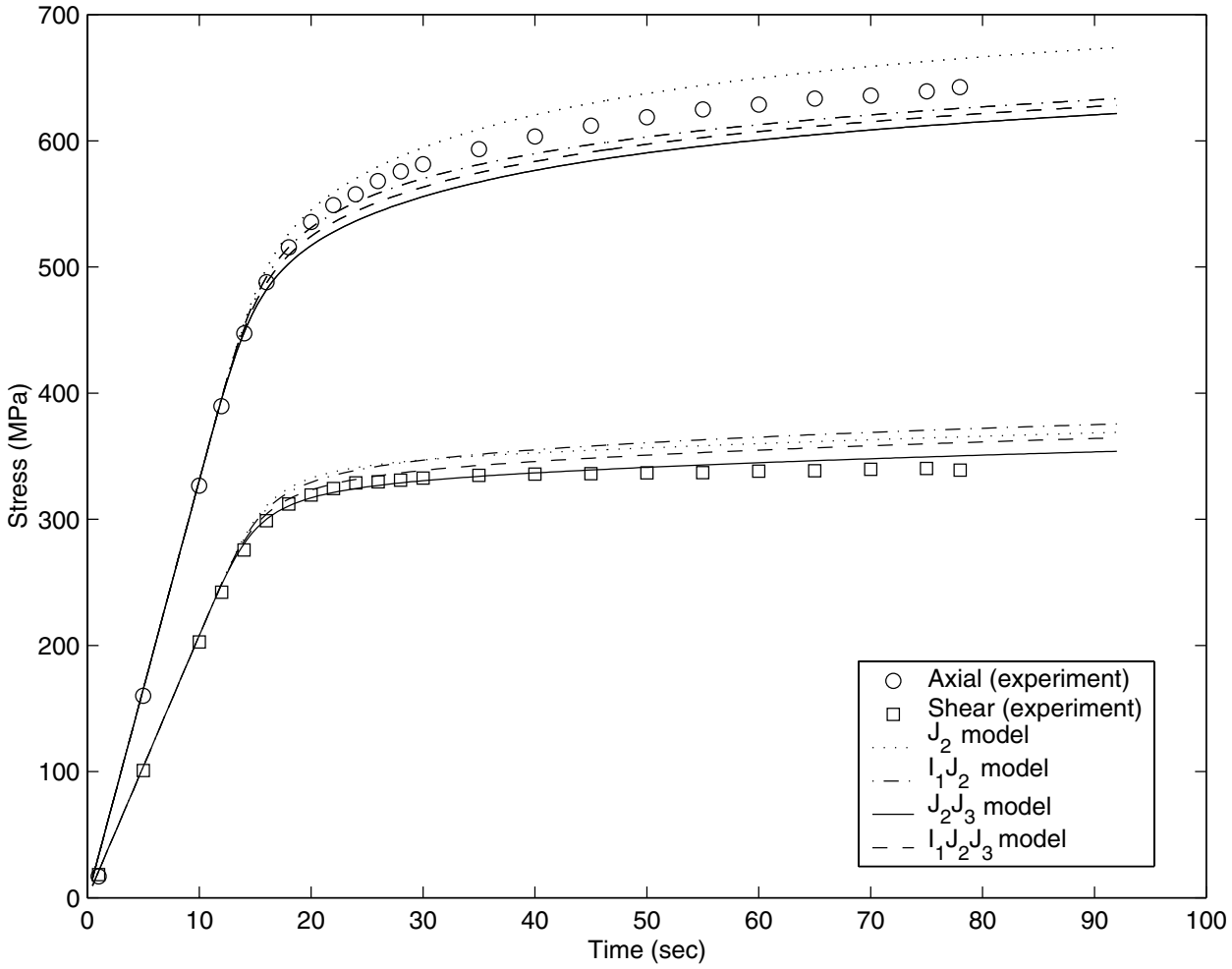

Figure 6.17: Proportional loading (IN5): Stress-time response ($m_1 = 1.0$)

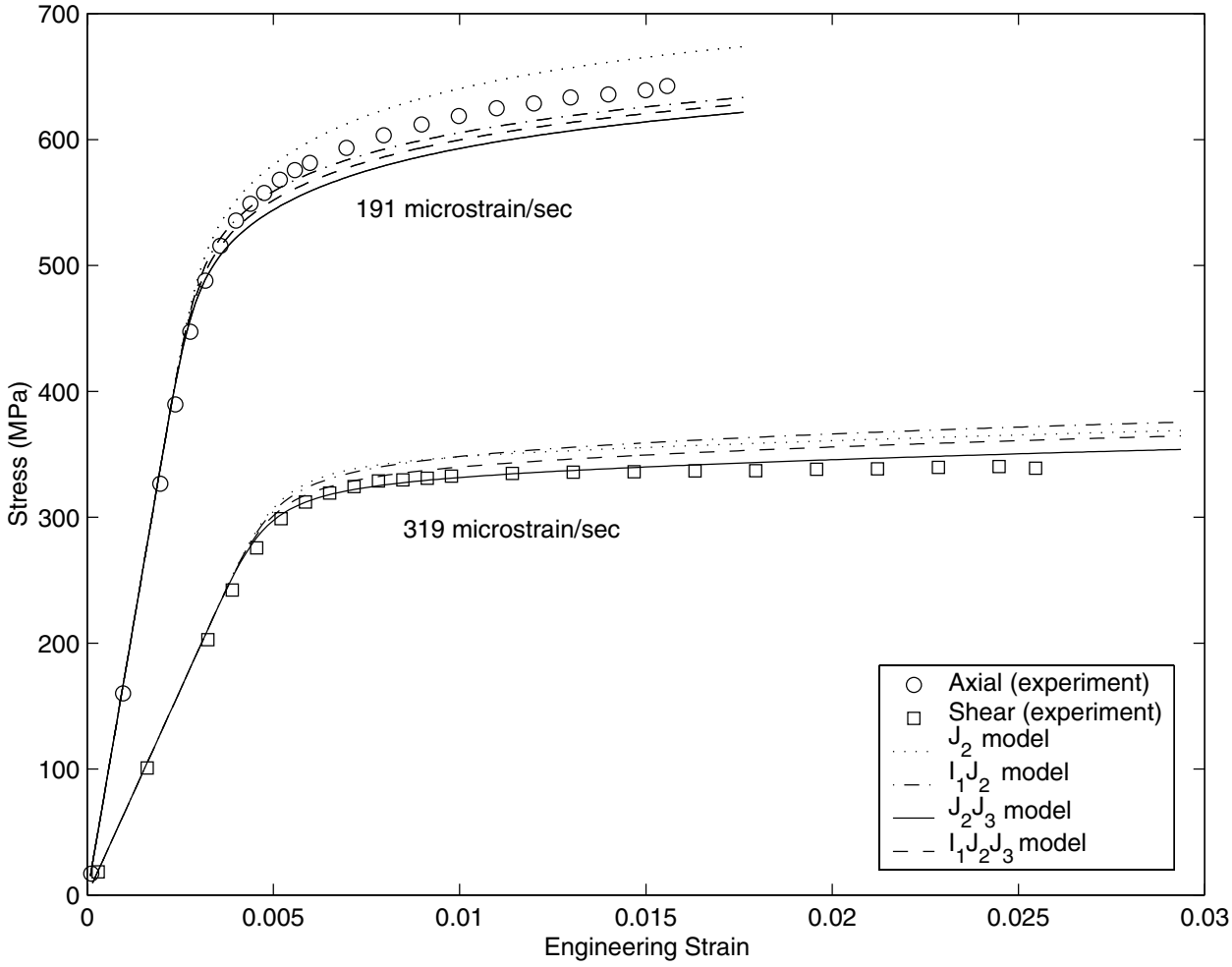

Figure 6.18: Proportional loading (IN5): Stress-strain response ($m_1 = 1.0$)

Tensile-shear loading (IN6)

Axial and shear stresses for tensile-shear loading are shown in Figures 6.19 and 6.20. All three models ($I_1 J_2$, $J_2 J_3$, and $I_1 J_2 J_3$) predict almost the same axial and shear stresses. Comparison with the experimental data is reasonable but the differentiation between the models in terms of their predictive capability is not achieved. Thus, it is difficult to say which model gives the best prediction for this experiment.

There are two possible explanations for the model predictions being almost identical.

1. Consider variations in the stress invariants $\tilde{I}_1$, $\tilde{J}_2$ and $\tilde{J}_3$ predicted by the $\tilde{J}_2$ model as shown in figure 6.21. Axial loading causes all of the invariants $\tilde{I}_1$, $\tilde{J}_2$ and $\tilde{J}_3$ to increase and attain a constant value. The subsequent shear loading causes only a marginal increase in $\tilde{J}_2$, while both $\tilde{I}_1$ and $\tilde{J}_3$ drop rapidly. This makes the coefficients a and c of the threshold function, which scale $\tilde{I}_1$ and $\tilde{J}_3$ respectively, ineffective. Thus, none of the model predictions are significantly different from that of the J_2 model.

2. During shear loading, $\tilde{J}_3$ drops rapidly for all the models and so does $\tilde{I}_1$ for $I_1 J_2$ and $I_1 J_2 J_3$ models. $\tilde{I}_1$ and $\tilde{J}_3$ become zero approximately at the same time (about 180 sec) giving a pure shear state (figure 6.21). Thereafter, the material remains in pure shear ($\tilde{J}_2 \neq 0$, $\tilde{I}_1 = \tilde{J}_3 = 0$) and the difference between model predictions vanish.

Compressive-shear loading (IN2)

Results of the compressive-shear loading are shown in Figures 6.22 and 6.23. Again, all models predict nearly the same axial and shear stresses for the same reasons as above for IN6.

During the compressive loading segment of the experiment, the shear stress did not remain zero as it should have. A closer look at the data reveals that the shear strains are negligibly small (< 10 microstrain). Hence, it is difficult to find a reason for the drift in shear stress.

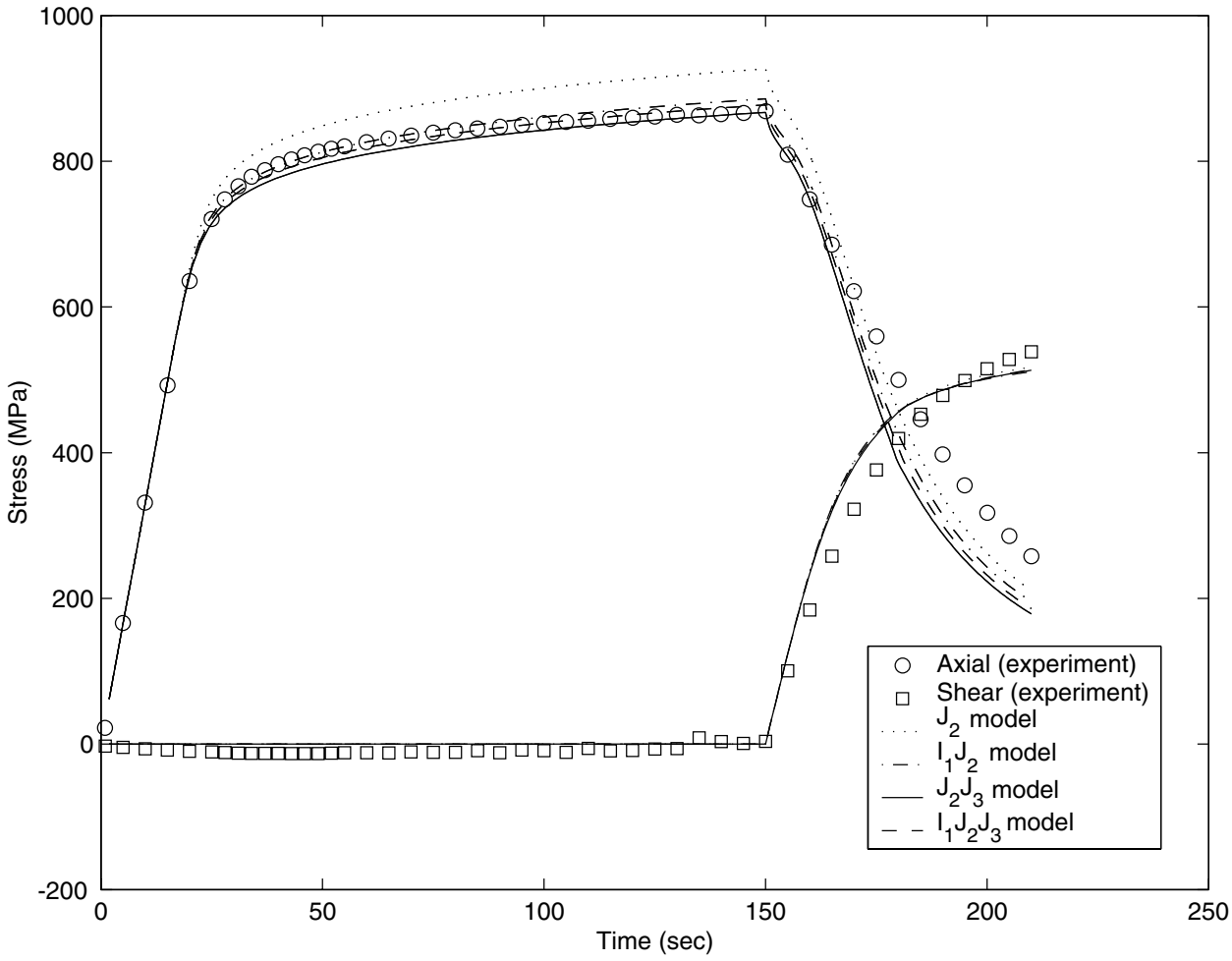

Figure 6.19: Tensile-shear loading (IN6): Stress-time response ($m_1 = 1.0$)

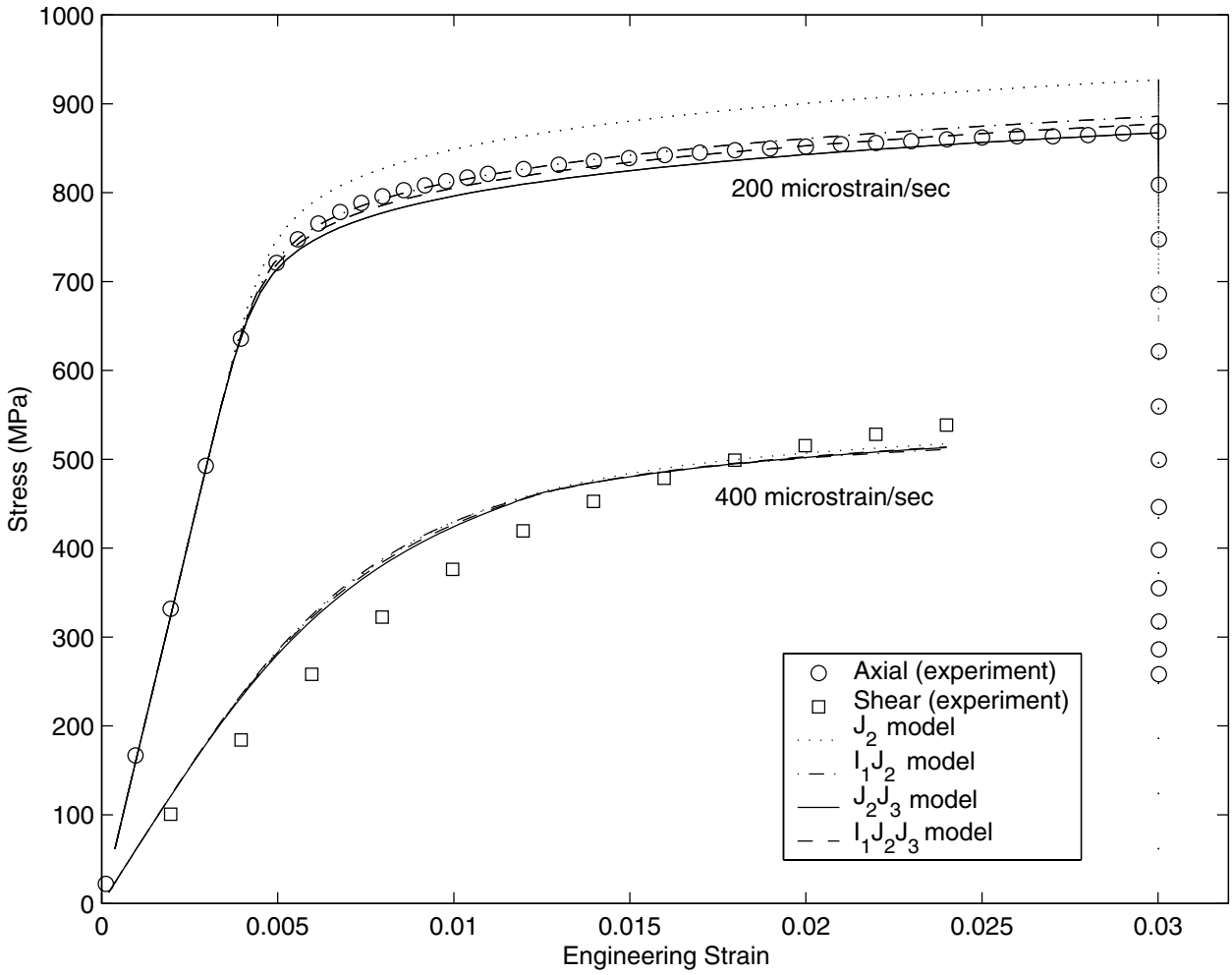

Figure 6.20: Tensile-shear loading (IN6): Stress-strain response ($m_1 = 1.0$)

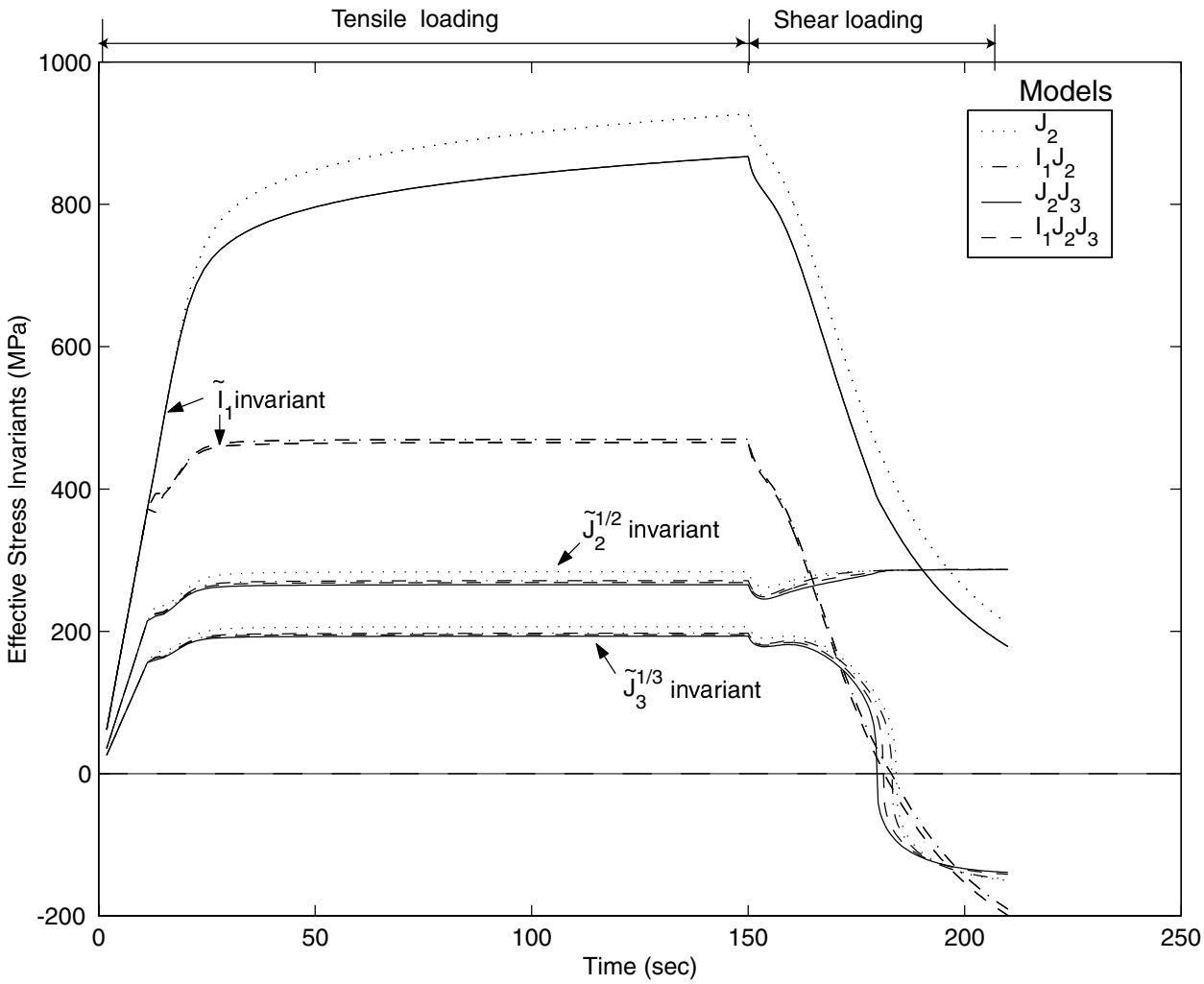

Figure 6.21: Model predictions for Stress Invariants: Tensile-shear loading (IN6)

This error results in unsatisfactory comparison between predictions and experiment. In the event of no experimental error, the model predictions might come close to experiments. However, the fact still remains that a good differentiation between the predictive capability of the models is not achieved.

Predictions from the models with m_1=0.6 are shown in Appendix D. There it is observed that changing the exponent m_1 to 0.6 does not change the predictions appreciably. Also, assigning different values to m_1 (other than 1.0 and 0.6) did not change the predictions significantly. Thus, further predictions are restricted to models with $m_1 = 1.0$.

6.3.3 Differentiating between models

Comparing the four biaxial experiments (IN4,IN5,IN6,IN2) it is clear that shear-axial loading (IN4) is most successful in differentiating between the models and points to a better predictive capability of the J_2J_3 and $I_1J_2J_3$ models. While proportional loading (IN5) moderately differentiates between the models, the load cases starting with axial load (IN6 and IN2) are unable to differentiate between the models.

Figure 6.24 tracks the variations of $\tilde{I}_1$, $\tilde{J}_2$, and $\tilde{J}_3$ for shear-axial loading (IN4). A clear difference between this and Figure 6.21 is that the invariants $\tilde{I}_1$ and $\tilde{J}_3$ increase substantially in the second segment (axial) of loading. This makes the coefficients a and c more effective and hence we see a large difference in the model predictions.

A simple way to achieve a substantial increase in $\tilde{I}_1$ and $\tilde{J}_3$ is to start with a shear loading and then apply other loading. Based on this idea, two more biaxial experiments (IN11 and IN28) were conducted. The load paths for these additional experiments are also shown in Figure 6.14. The corresponding test matrix is given in Table 6.9.

Shear-proportional loading (IN11)

Shear stresses predicted by all models are identical and are in good agreement with the experimental data as shown in Figures 6.25 and 6.26 . There is a clear difference between the model predictions for axial stress. The J_2J_3 and $I_1J_2J_3$ model predictions follow the

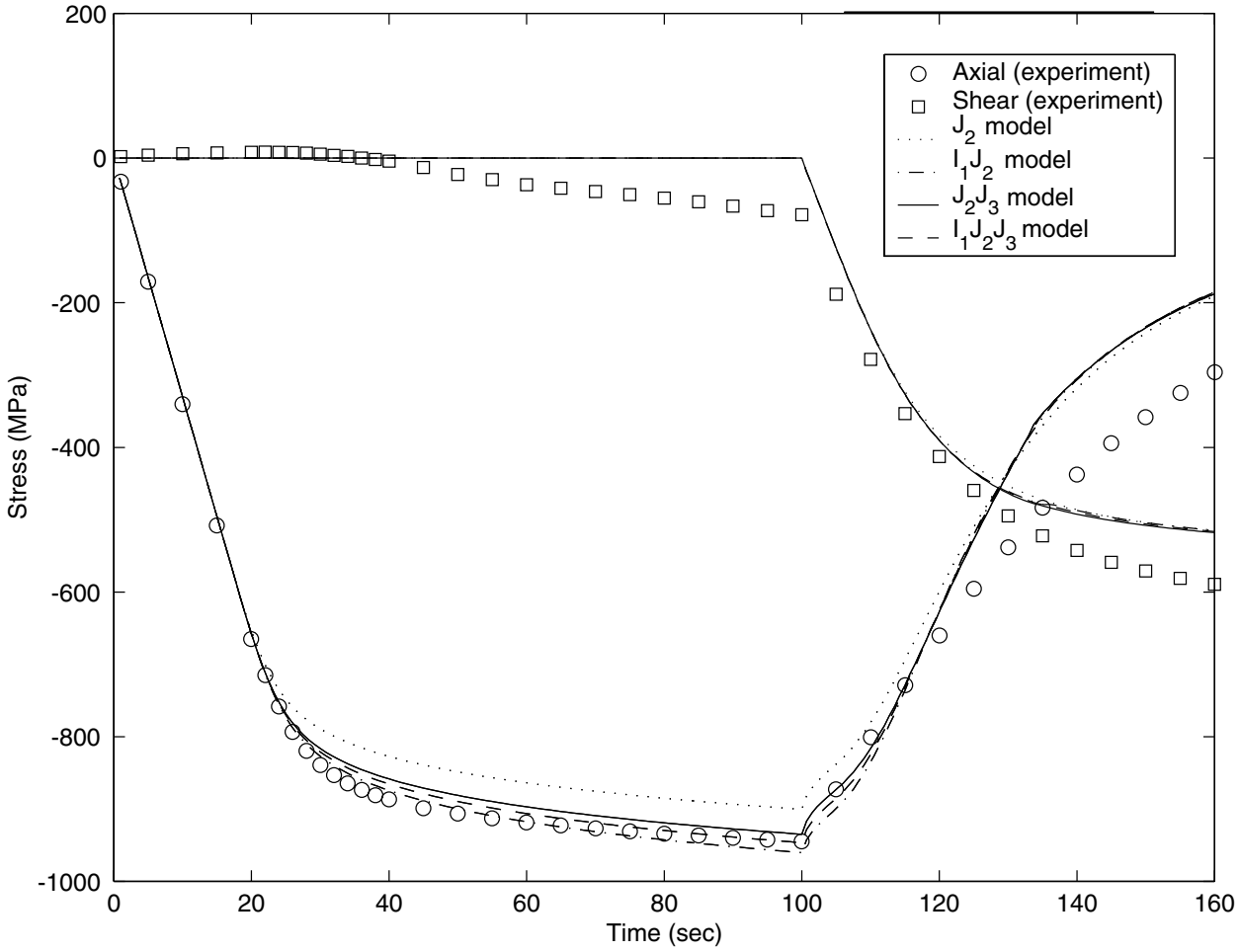

Figure 6.22: Compressive-shear loading (IN2): Stress-time response ($m_1 = 1.0$)

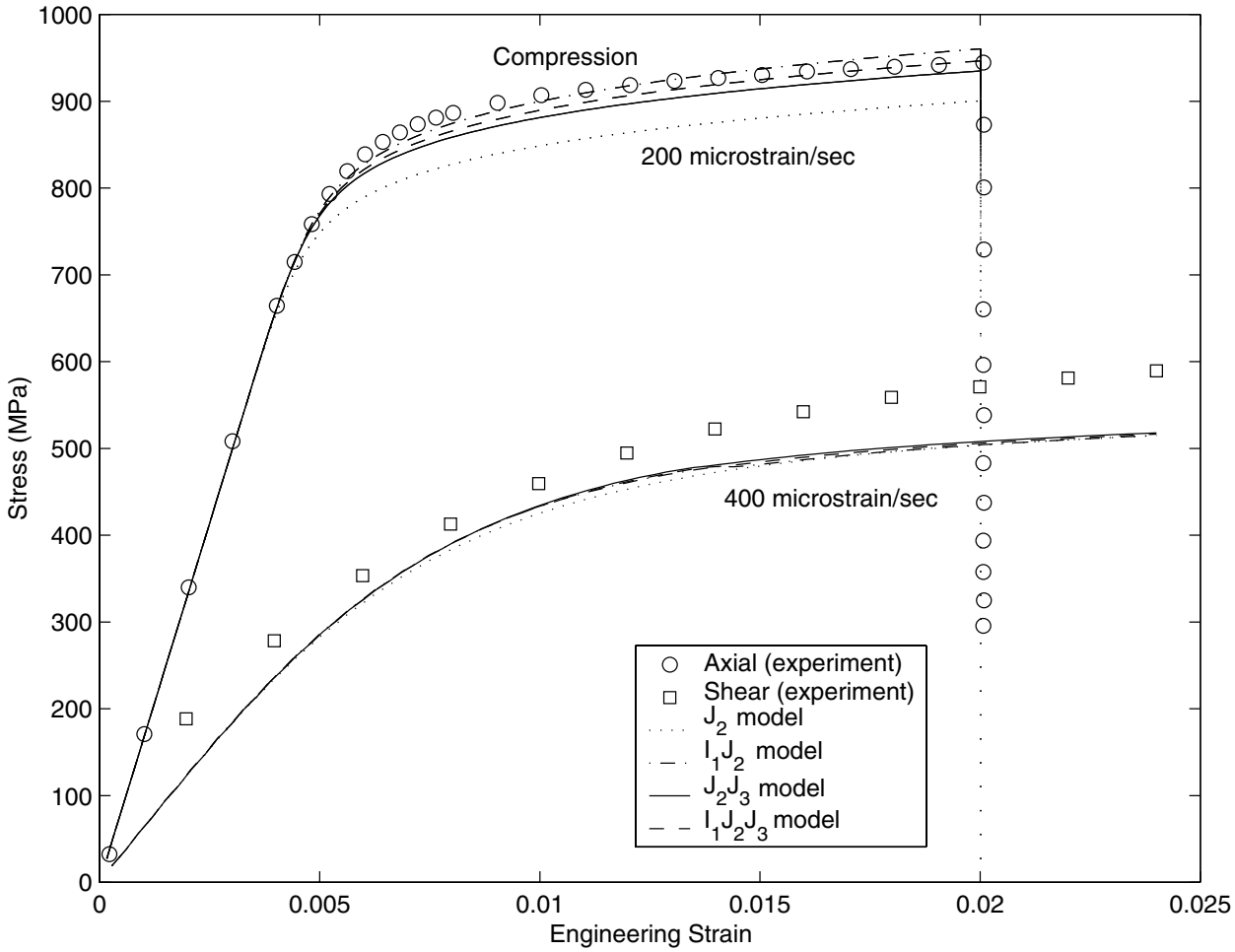

Figure 6.23: Compressive-shear loading (IN2): Stress-strain response ($m_1 = 1.0$)

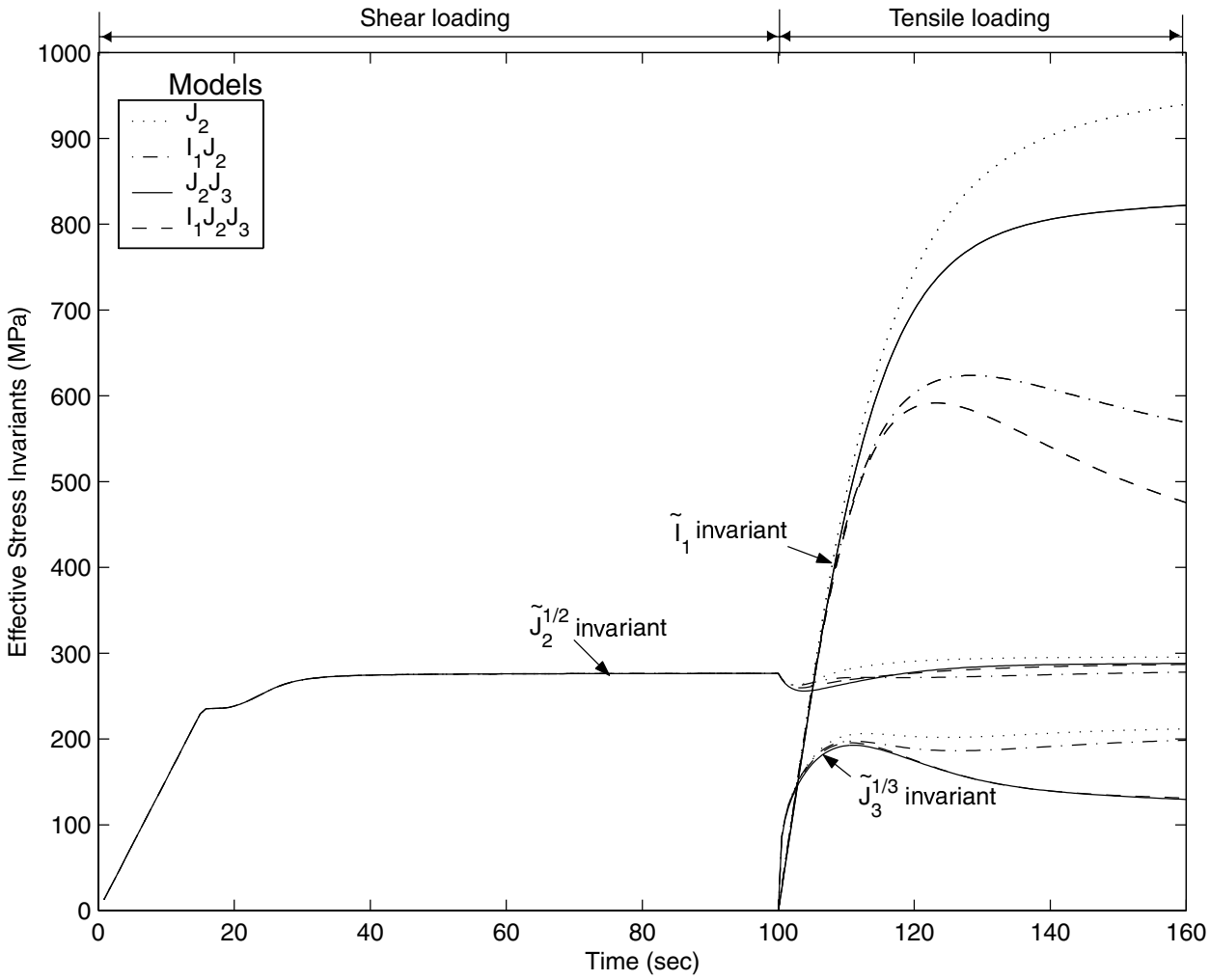

Figure 6.24: Model Predictions: Shear-tensile loading (IN4)

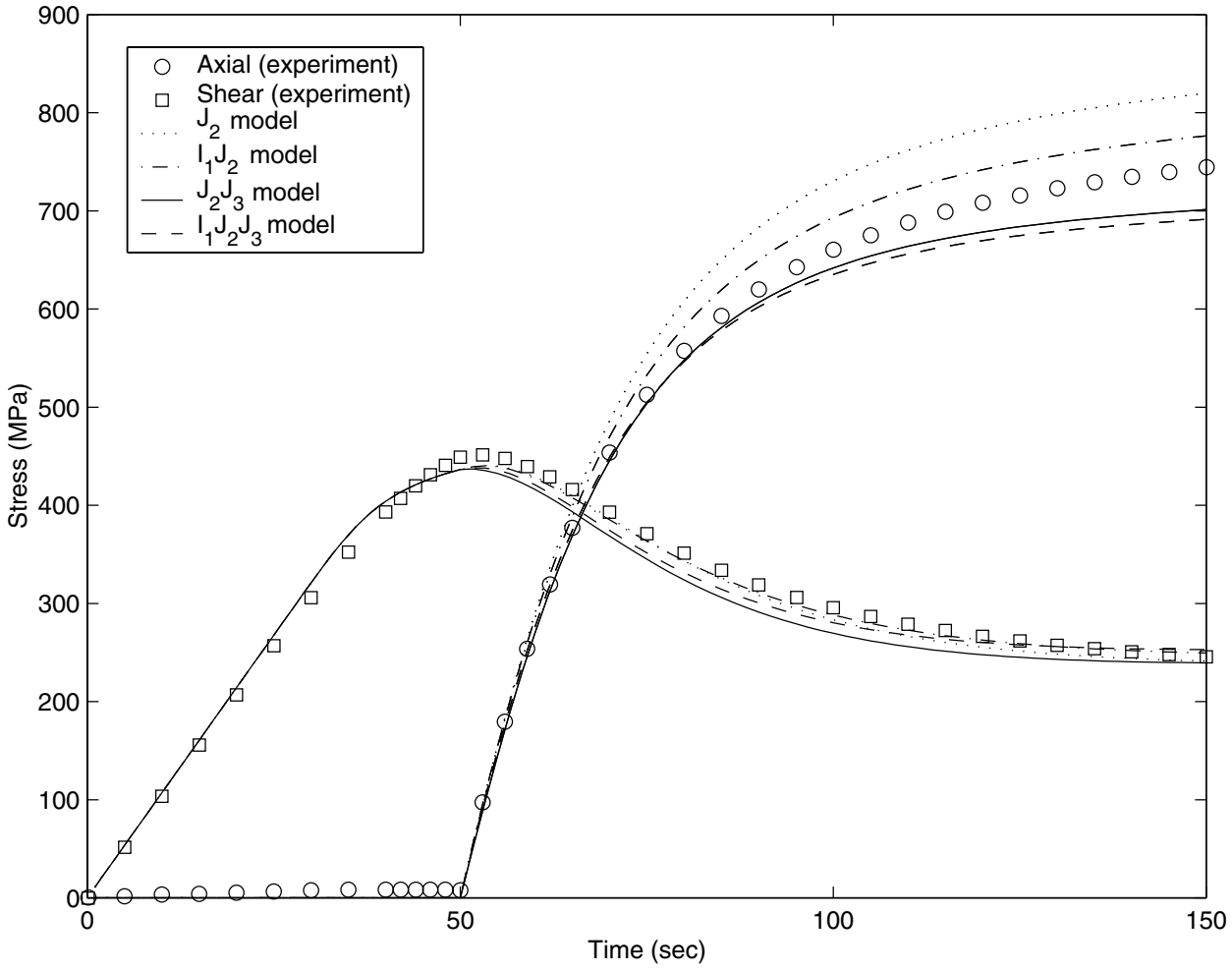

Figure 6.25: Shear-proportional loading (IN11): Stress-time response

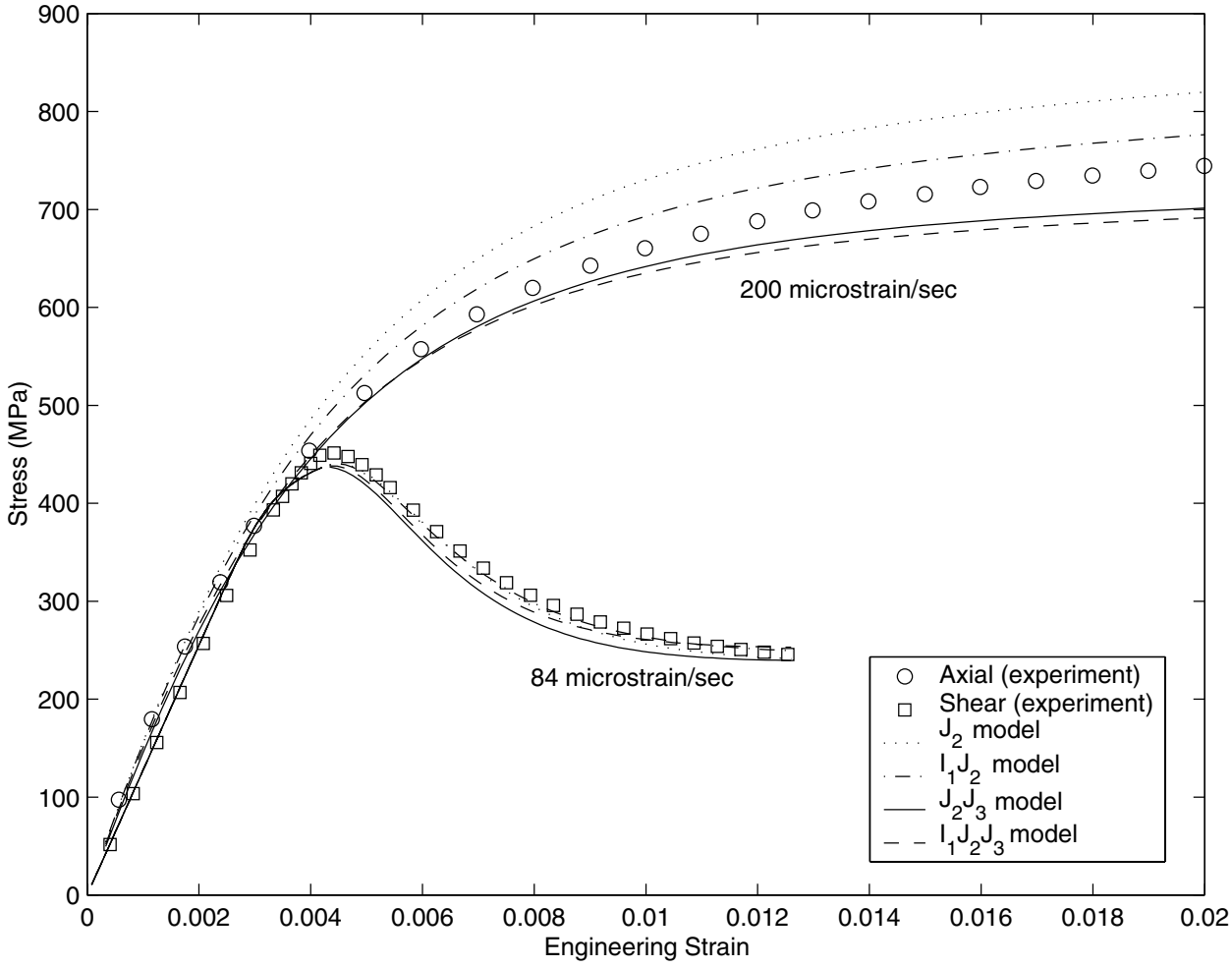

Figure 6.26: Shear-proportional loading (IN11): Stress-strain response

experimental data closely for most of proportional loading. The I_1J_2 model over-predicts the stress throughout the proportional loading. This further reassurance in the predictive capability of the J_2J_3 and the $I_1J_2J_3$ models.

Shear-compressive loading (IN28)

Stress predictions for shear-compressive loading are shown in Figures 6.27 and 6.28. Shear stresses predicted by all models are not substantially different. The difference in predictions is clearly seen for axial stresses. The J_2 model over-predicts the compressive stresses and the I_1J_2 model predicts an even higher compressive stress. Predictions using J_2J_3 and $I_1J_2J_3$ models show good agreement with the compressive experimental data.

There is a discrepancy between the experimental values of the shear stress and the model predictions during the second loading segment (AB). The shear stress did not drop to almost zero as it did in the other experiments (Figure 6.15). There were no errors noted during the experiment and the strain history (shear and axial) is correct. This makes it difficult to say why the shear stress did not drop as much as it was expected to. Also, there was a slight drift in axial stress in the first loading segment for reasons similar to IN2. However, our primary interest is in the axial stress during the second loading segment and we disregard these discrepancies. This experiment points to the fact that the predictive capability of the J_2J_3 model is better than that of the I_1J_2 model. In this case, the $I_1J_2J_3$ model also shows a good correlation with experimental data.

6.4 Summary of model predictions

Introduction of hydrostatic pressure dependence (through I_1) in the baseline (J_2) model did not improve the model predictions. In the shear-compressive loading (IN28), the I_1J_2 model does not predict the axial stress well, even compared to the baseline model. Hence, the I_1J_2 model can be ruled out for Inconel 718. The J_2J_3 and $I_1J_2J_3$ models have consistently shown good predictive capability.

Experiments are in progress at Case Western Reserve University to study the effect of

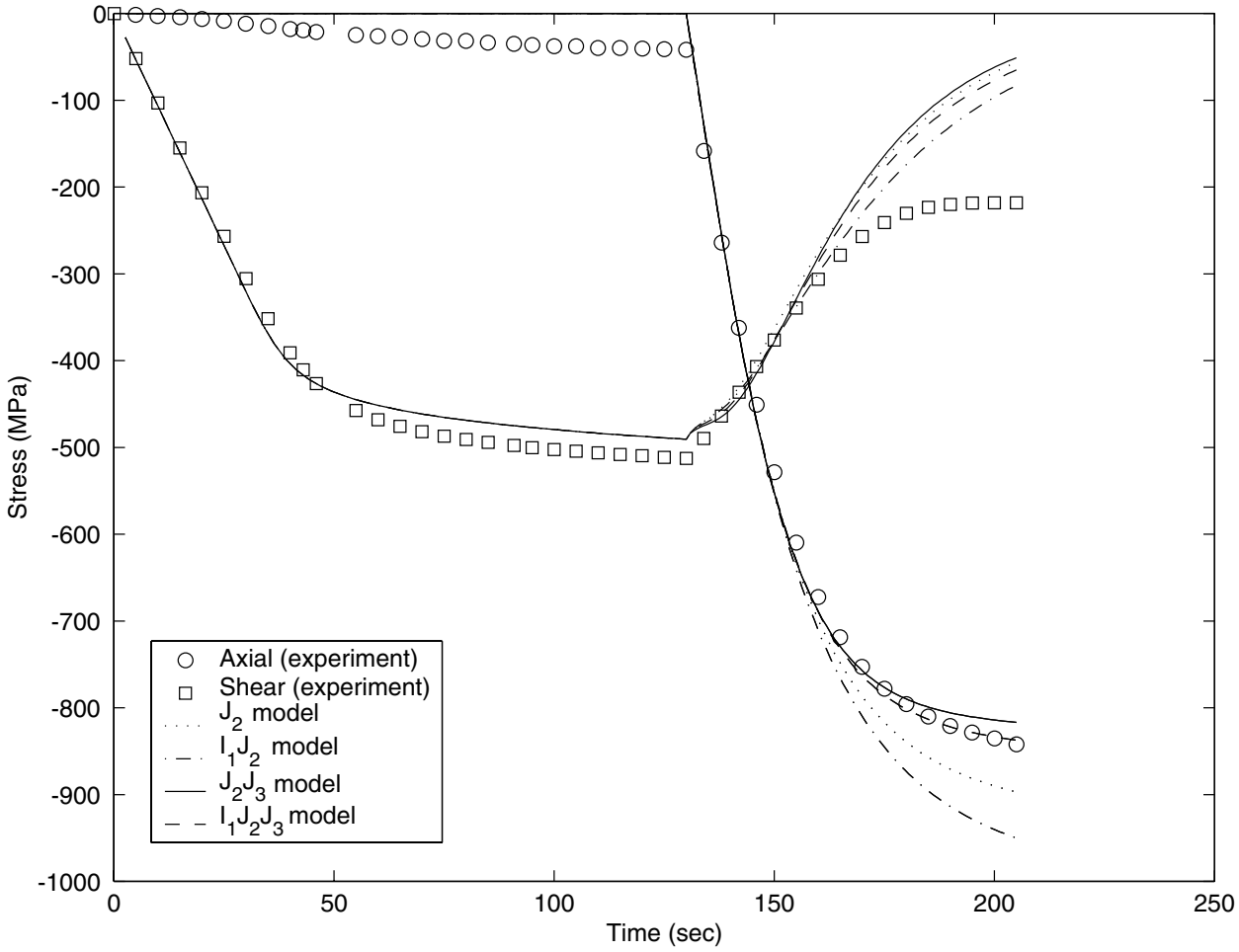

Figure 6.27: Shear-compressive loading (IN28): Stress-time response

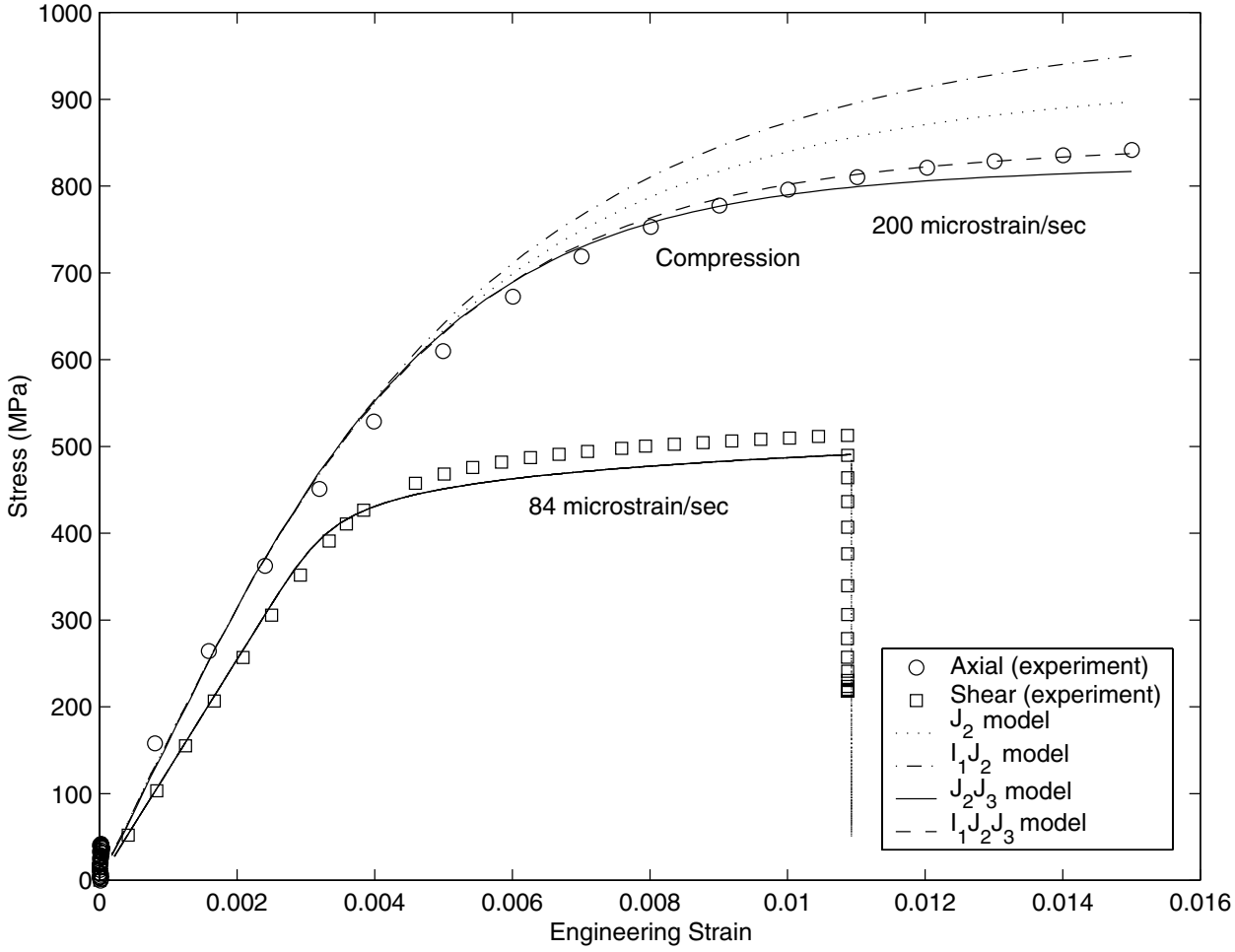

Figure 6.28: Shear-compressive loading (IN28): Stress-strain response

Table 6.10: Material parameters for Inconel 718 at 650°C

Parameter	Value
κ (MPa)	234.7
n	2.0
μ (MPa-s)	1.7681×10^{5}
m	7.0
β	3.652
R (1/s)	1.0×10^{-12}
H (MPa)	1.966×10^{4}
a ($1/MPa^2$)	0.0
b ($1/MPa^2$)	1.8154×10^{-5}
c ($1/MPa^2$)	4.5×10^{-6}
m_1	1.0

hydrostatic pressure on the flow behavior of aged Inconel 718 at room temperature. Initial experiments show that the yield and flow in the material is not affected by pressure. These experiments suggest that inelastic deformation in Inconel 718 is relatively independent of I_1 and hence we can choose the J_2J_3 model over the $I_1J_2J_3$ model.

All the material parameters for the model are now determined and their values are given in Table 6.10.

6.5 Comments on the method

Some aspects of the formulation and experimental procedure need to be put in perspective.

6.5.1 Load Paths

In three dimensional principal stress space, load paths can be found along which only one of the effective invariants changes while the other two remain constant (equation 5.1). Owing to the complexity involved with three dimensional testing, two dimensions load paths in

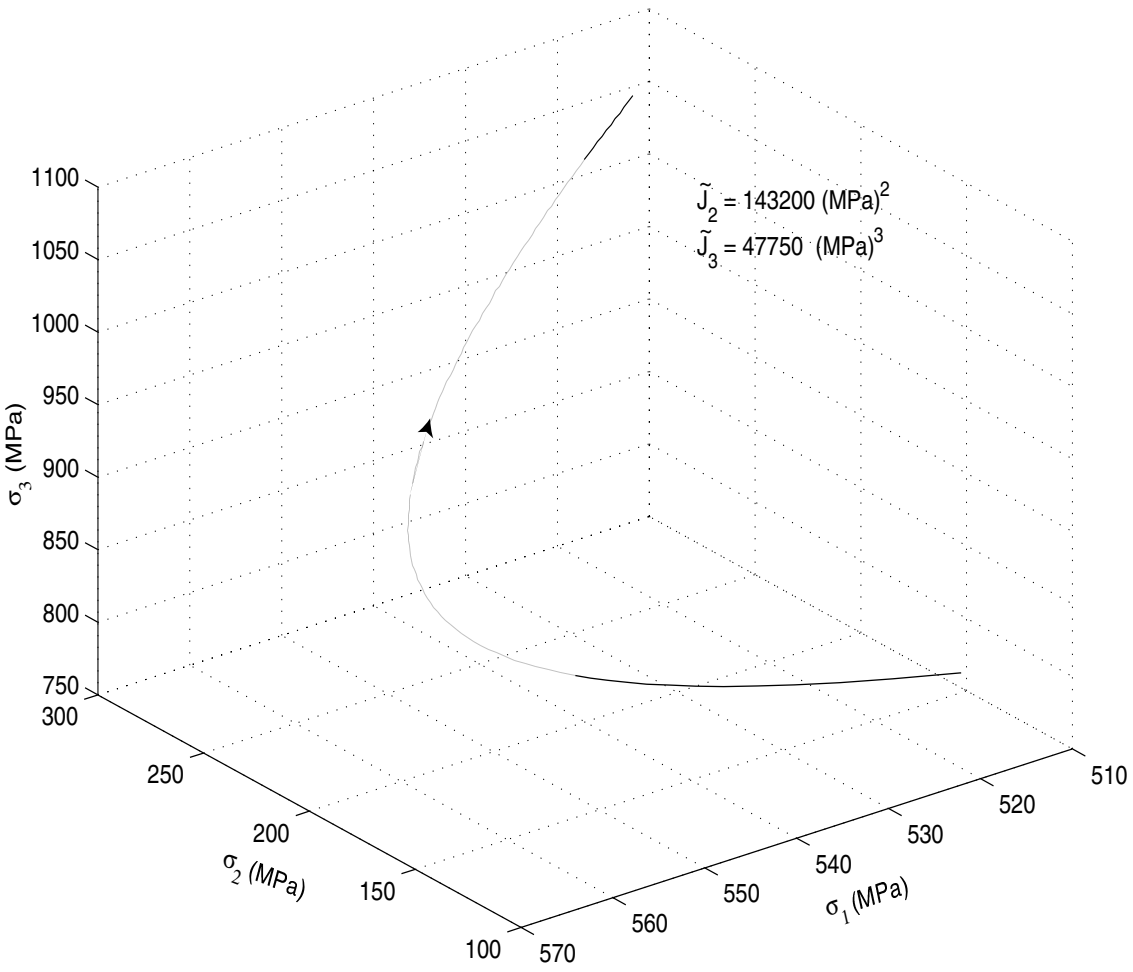

Figure 6.29: Principal stress paths with $\tilde{I}_1$ changing - $\tilde{J}_2$ and $\tilde{J}_3$ constant

axial-shear plane were found along which $\dot{\tilde{J}}_2$ is constant and $\tilde{I}_1$ changes (keeping $\tilde{J}_3$ constant) or $\tilde{J}_3$ changes (keeping $\tilde{I}_1$ constant). Some illustrations of such load paths in effective axial-shear stress space were given. However, in the external stress space the corresponding load paths are more complicated. This is because the internal stresses evolve during inelastic deformation and do not necessarily follow the external stresses. Two load paths in principal stress space are shown in Figure 6.29 and Figure 6.30, which correspond to paths CD in Figure 5.5 and path AB Figure 5.7 respectively. It may be possible to follow these load paths but these tests involve three dimensional loading, which requires complex experimental set up.

In order to avoid the above complexity, an alternative approach was adopted which involves simpler experiments. Simple shear experiments helped to determine all of the parameters

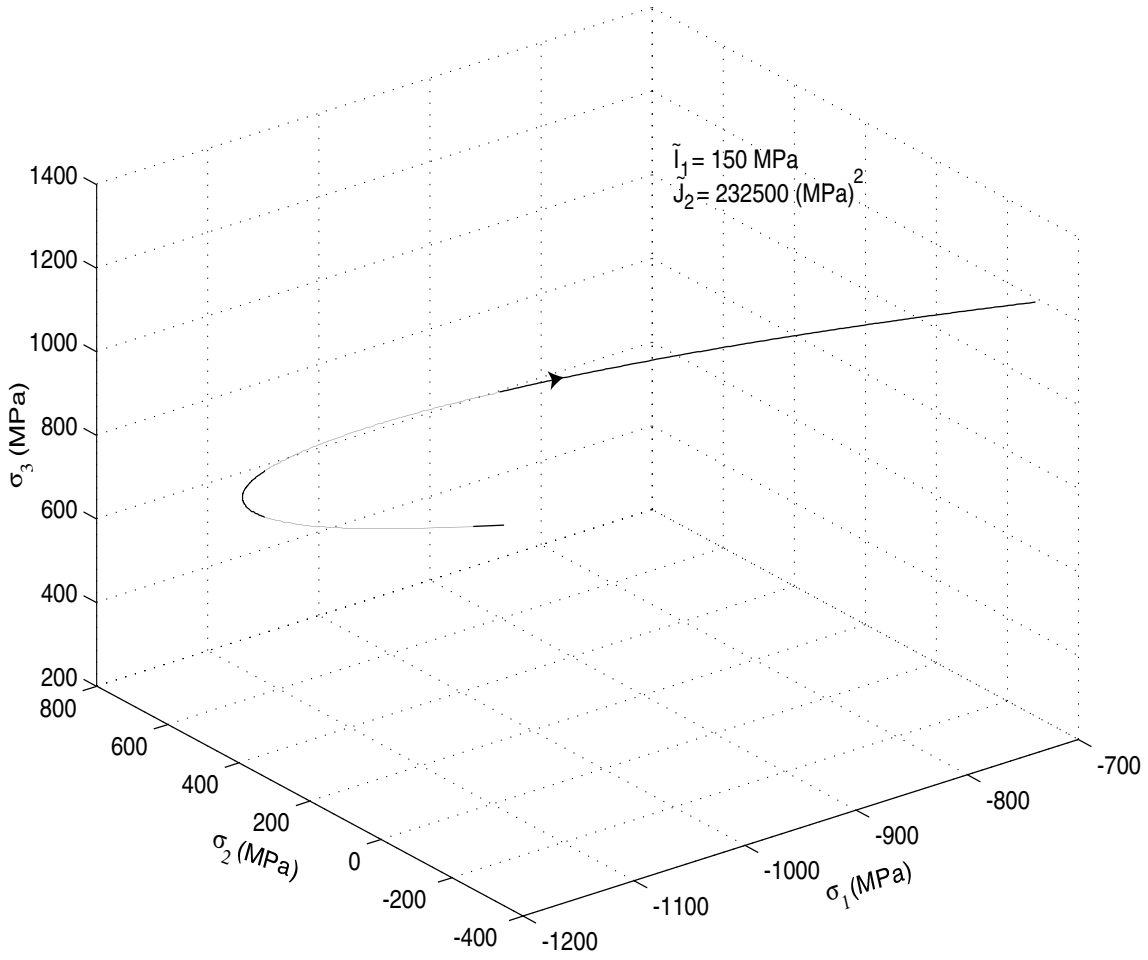

Figure 6.30: Principal stress paths with $\tilde{J}_3$ changing - $\tilde{I}_1$ and $\tilde{J}_2$ constant

associated with the baseline GVIPS model. The difference is in the determination of the additional contribution of $\tilde{I}_1$ (through a), $\tilde{J}_3$ (through c) and exponent m_1. Instead of trying to determine the contribution of these invariants directly through complicated load paths, an indirect procedure involving simple uniaxial and biaxial tests was adopted. A few combinations of threshold surface parameters (a, b, c, m_1) were obtained that fit the axial test data (tensile and compressive) well. The biaxial tests helped to differentiate between the models with respect to their predictive capability. Hence, biaxial experiments were useful in identifying the right combination of invariants and also in validating the model.

The design of experiments in Chapter 5 was helpful in two ways; (1) it established an experimental procedure to effectively isolate the effect of each invariant on inelastic deformation and (2) it provided a methodology for differentiating between the models using biaxial

experiments.

6.5.2 Threshold function

The choice of the threshold function was the key in formulation. The main advantages of this form are addressed below.

Current form

There are several advantages of using the generalized polynomial form (equations 4.22 and 4.23) for the threshold function.

1. The function in equation 4.22 is easily reducible to well known models like Mises and Drucker-Prager.

2. Both functions reduce to the baseline model (equation 4.15) for pure shear loading which allows the use of *COMPARE* for estimation of GVIPS parameters.

3. The effect of each stress invariant on inelastic deformation can be determined separately due to the chosen form of the threshold function. Also, the resulting flow and evolutionary laws are mathematically separable into terms associated with each invariant. This is a definite numerical advantage in that it allows easy inclusion or exclusion of a given invariant in the formulation by simply choosing a zero or a nonzero value for the corresponding coefficient.

4. The effectiveness of using the form in equation 4.23 (instead of equation 4.22) was not seen in this investigation. This is because the value of the threshold function is not significantly different for the two values of m_1 (1.0 and 0.6) and the corresponding parameters (a, b, c) in Table 6.8.

   Let us consider an example of axial loading and a $I_1 J_2$ model. The values of the threshold function are plotted as a function of the ratio a/b (significance of I_1 relative to J_2) for m_1=1.0 and m_1=0.6 (Figure 6.31). For low values of the ratio ($\cong$ 0.01 for Inconel 718) there is no difference between the threshold value for m_1=1.0 and that for m_1=0.6. However, as the ratio increases, there is a significant difference between

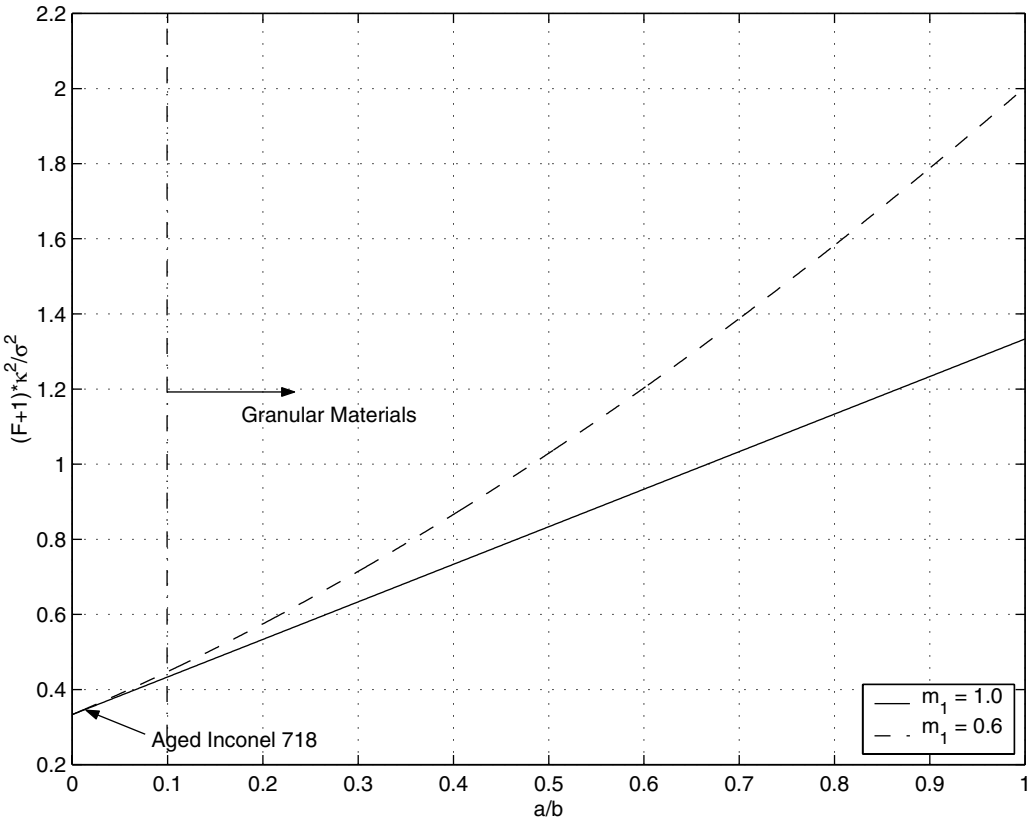

Figure 6.31: Variation of threshold function for axial loading

the two. Thus, for materials with high a/b ratio (granular or frictional materials), changing m_1 is more effective. For this reason, we retain the form in equation 4.23 and not revert to equation 4.22 in the formulation.

Alternative functions

Some alternative functional forms such as exponential or implicit forms can be considered for the threshold function. But these forms will result in flow and evolution equations where the invariants are not easily separable. This makes the objective of studying the effect that each invariant has on the SD effect more difficult.

Another possibility is to use a polynomial form with different exponent (equation 4.22 with $m_1 \neq 1$) for better data fitting capability. Such a function will not reduce to the form in the baseline model (equation 4.15) for pure shear loading. Hence the baseline model would have

to be altered and the whole optimization software reworked to determine the parameters associated with the baseline model.

6.5.3 Flow law

Hydrostatic pressure-dependence is represented by the use of I_1 in the threshold function. An associated flow law for pressure-dependent materials often over-predicts the volume expansion during deformation (e.g. Spitzig et al [1975]). However, based on the initial experiments on aged Inconel 718 at the Case Western Reserve University, the effect of hydrostatic pressure on inelastic deformation appears to be relatively low, resulting in a I_1-independent material. Hence, the volume expansion is not expected to be over-predicted by the associated flow law. Also, the predictions using an associated flow law compare well with experiments. Thus, the need for use of a non-associated flow law does not arise for Inconel 718.

6.5.4 Mechanism for SD

Various deformation mechanisms in Inconel 718 were discussed in Chapter 2. It appears that the particle-dislocation interaction is a more probable cause for the SD than is volume expansion. Volume expansion is caused by the retarding effect of hydrostatic pressure on the mobile dislocations, with an associated increase in dislocation density. But, since the inelastic deformation in Inconel 718 appears to be relatively independent of hydrostatic pressure, the volume expansion hypothesis can be ruled out as a cause of SD. Thus, the main cause of SD appears to be the interaction between coherency strain fields around γ'' precipitates and dislocations.

Chapter 7

Conclusions and Future Work

This chapter starts by summarizing the steps that were involved in the development of the unified viscoplastic model to account for the SD effect. Conclusions that can be drawn from this work are presented next. Finally, future work that could be undertaken for the betterment of the model is suggested.

7.1 Summary

A potential based viscoplasticity model (GVIPS), based on J_2, was the starting point of the model development. In order to account for the SD effect, the threshold function was generalized by including the other two stress invariants (I_1 and J_3) in its definition. A polynomial form was used for the threshold function. Flow and evolution laws to describe the material behavior during inelastic deformation were derived from the proposed threshold function.

Experiments were performed on aged Inconel 718 at 650°C to quantify the material parameters in the model. Shear loading was chosen to estimate all the parameters associated with the GVIPS model because, for this loading $I_1 = J_3 = 0$ and the proposed model reduces to the GVIPS model. The parameters associated with I_1 and J_3 do not affect the determination of the other parameters for this loading. Shear tests involved monotonic loading (strain and stress control), relaxation, and creep tests with different loading rates and load levels.

GVIPS parameters were optimized to fit the experimental data in shear. The experimental data sets were chosen judiciously and the weighting of test data was changed iteratively to arrive at the final GVIPS parameters. The goal was to obtain an axial stress-strain response intermediate between tension and compression test data.

Tension and compression tests were conducted up to strains of 2%. By introducing positive values for the parameters a (which scales I_1) or c (which scales J_3) or both, three combinations of invariants were developed. Values of the coefficients were converged upon by comparing model predictions with the tension and compression test data. The resulting threshold functions had $I_1 J_2$, $J_2 J_3$ and $I_1 J_2 J_3$ forms. Convexity of these threshold functions in the three dimensional principal stress space was confirmed by checking the resulting curvature tensor for positive definiteness.

An experimental procedure for studying the effect of each stress invariant on the inelastic deformation was established in three dimensional principal stress space. This requires following complicated paths in three dimensional stress space. Simple biaxial tests were chosen instead of three dimensional paths for experimental simplicity. Six axial-torsional experiments were conducted on tubular specimens of aged Inconel 718 at 650°C. Comparison of the test data with model predictions indicated that the use of J_3 in the threshold function significantly improved the predictive capability of the model especially for non-proportional load paths. However, using I_1 in the formulation did not improve model predictions. In some load cases, introduction of I_1 widened the gap between experiments and model prediction. Also, preliminary results from tension and compression tests conducted under hydrostatic pressure indicate that inelastic deformation is relatively independent of pressure, indicating I_1-independence. It was therefore established that aged Inconel 718 is a $J_2 J_3$ material.

7.2 Conclusions

The following conclusions can be drawn from the investigation of inelastic behavior of aged Inconel 718.

- A unified viscoplastic model was developed that effectively predicts a strength differential effect.

- The ability of the model to represent the strength differential effect was demonstrated for aged Inconel 718 at 650°C.

- A general form of the threshold function in terms of the stress invariants I_1, J_2, and J_3 was proposed and specialized into four trial functions: J_2, $I_1 J_2$, $J_2 J_3$, and $I_1 J_2 J_3$. The $J_2 J_3$ threshold function appears to best represent the inelastic response of Inconel 718, indicating no pressure dependence of flow.

- The model with a $J_2 J_3$ threshold function exhibited excellent predictive capability under non-proportional axial-torsional loading applied at elevated temperature.

- A general method to determine the effect that each stress invariant has on inelastic deformation was established. A current limitation of this method is that three dimensional stress paths must be applied.

- A procedure to determine the convexity of any function in three dimensional stress space was implemented to verify convexity of the threshold function. It was established that the model developed for aged Inconel 718 satisfies Drucker's stability criterion.

- The physical mechanism responsible for the strength differential in Inconel 718 appears to be the interaction between coherency strain fields around γ'' precipitates and the dislocations.

- The viscoplastic model is very general in that it can be applied to many materials, including the ones that do not exhibit a strength differential. The suggested experimental procedure for characterizing and validating the model is simple and hence can be applied to a wide range of materials.

7.3 Future work

The viscoplastic model developed in this investigation opens the door for research in related areas.

- More variety of tests can be conducted for model characterization. A test matrix can be derived which is best for optimization of the material parameters.

- Direct effect of individual stress invariants on the inelastic deformation can be obtained by following three dimensional stress paths developed using the proposed threshold function. To this end, complicated two dimensional stress paths in the axial-torsional stress space with constant J_2 rate, that seem more feasible, can also be attempted.

- The threshold surface parameters that fit the axial test data well did not fit the initial threshold surface data. One way to effectively account for this is to make the coefficients of I_1 and J_3 (a and c) a function of inelastic deformation. This way, the parameters can have initial values that fit the initial threshold surface data, and then can evolve such that a good correlation is also obtained with the uniaxial test data.

- Experimental data for different strain rates can be used in characterizing the model so that its predictive capability is improved for a range of loading rates. Similarly, if the capability of the baseline model to account for variation in temperature can be exploited, a non-isothermal model can be built using this procedure. This would additionally involve experiments at different temperature levels.

- It will be interesting to evaluate the performance of the model using a different class of material, e.g. granular materials. The effectiveness of the model would be established if it is able to predict the hydrostatic pressure-dependence that is prevalent in these materials.

- Alternative ways of microstructural evaluation of samples deformed under tension and compression can be explored to determine the exact mechanism causing SD.

References

Althoff, J. and Wincierz, P.[1972]. "The Influence of Texture on the Yield Loci of Copper and Aluminum," *Zeitechrift Für Metallkunde*, Vol. 63, p. 623.

Arnold, S.M.[1987]. "Effects of State Recovery on Creep Buckling Induced by Thermomechanical Loading," *Ph.D Thesis*, University of Akron, Akron, OH.

Arnold, S.M. and Saleeb, A.F.[1994], "On the Thermodynamic Framework of Generalized Coupled Thermoelastic-Viscoplastic Damage Modeling," *International Journal of Plasticity*, Vol. 10, p. 263.

Arnold, S.M., Saleeb, A.F., and Castelli, M.G.[1996]. "A fully associative, non-isothermal, nonlinear kinematic, unified viscoplastic model for titanium alloys," in Verrilli, M.J., and Castelli, M.G. (eds.) *Thermomechanical fatigue behavior of materials: Second Volume*, ASTM STP-1263, American Society for Testing and Materials, Philadelphia, p. 146.

Battiste, R.L. and Ball, S.J.[1986]. "Determination of Surfaces of Constant Inelastic Strain Rate at Elevated Temperature," *NASA Conference Publication 2444: Turbine Engine Hot Section Technology*, p. 307.

Bodner, S.R.[1968]. Mechanical Behavior of Materials Under Dynamic Loads. U.S. Lindholm (ed.), Springer-Verlag, New York, p. 176.

Bodner, S.R. and Partom, Y. [1972]. "Large Deformation Elastic-Viscoplastic Analysis of a Thick-Walled Spherical Shell," *Journal of Applied Mechanics, Trans. ASME*, Vol. 39, no. 3, p. 751.

Bodner, S.R. and Partom, Y.[1975]. "Constitutive Equations for Elastic-Viscoplastic Strain

Hardening Materials," *Journal of Applied Mechanics*, Vol. 24, p. 283.

Bodner, S.R.[1990]. "Review of a unified elastic-viscoplastic theory," in Miller, A.K. (ed.) *Unified constitutive equations for creep and plasticity*, Elsevier, Amsterdam, p. 273.

Bridgman, P.W.[1952]. Studies in large plastic flow and fracture. McGraw-Hill, New York.

Calloch, S. and Marquis, D.[1999]. "Triaxial Tension-Compression Tests for Multiaxial Cyclic Plasticity," *International Journal of Plasticity*, Vol. 15, p. 521.

Chaboche, J.L.[1977]. "Viscoplastic Constitutive Equations for the Description of Cyclic and Anisotropic Behavior of Materials," *Bull. Acad. Pol. Ser. Sci. Tech.*, Vol. 25, p. 33.

Chait, R.[1973]. "The strength differential effect of steel and Ti alloys as influenced by test temperature and microstructure," *Scripta Metallurgica*, Vol. 7, no. 4, p. 351.

Chen, W.F.[1994]. Constitutive equations for engineering materials. Elsevier, Amsterdam.

Clinard, J.A. and Lacombe, C.[1988]. "Determination of Multiaxial Flow Surfaces at Elevated Temperatures Using the Concept of Dissipation Potential," *ORNL-TM-10787*, Oak Ridge National Laboratory, Oak Ridge, TN.

Coleman, B.D. and Gurtin, M.E.[1967]. "Thermodynamics with Internal State Variables," *J. Chem. Phys.*, Vol. 47, p 597.

Desai, C.S. and Zhang, D.[1987]. "Viscoplastic Model for Geologic Materials with Generalized Flow Rule," *International Journal for Numerical and Analytical Methods in Geomechanics*, Vol. 11, p. 603.

Drucker, D.C.[1949]. "Relation of experiments to mathematical theories of plasticity," *Journal of Applied Mechanics*, Vol. 16, p. A349.

Drucker, D.C.[1951]. "A More Fundamental Approach to Plastic Stress-Strain Relations ," *Proc. 1st US Nat. Congr. Appl. Mech. (ASME)*, pp.487.

Drucker, D.C., and Prager, W.[1952]. "Soil Mechanics and Plastic Analysis or Limit Design," *Quarterly of Applied Mathematics*, Vol. 10, p. 157.

Drucker, D.C.[1959]. "A Definition of Stable Inelastic Material," *Journal of Applied Mechanics*, Vol. 26, p. 101.

Drucker, D.C.[1960]. Plasticity. J.N. Goodier and N.J. Hoff (eds.), Structural Mechanics, Pergamon Press, London, p. 407.

Drucker, D.C.[1973]. "Plasticity theory, strength differential (SD] phenomenon and volume expansion in metals and plastics," *Metallurgical Transactions*, Vol. 4, p. 667.

Ellis, J.R., Robinson, D.N., and Pugh, C.E.[1983]. "Time Dependence in Biaxial Yield of Type 316 Stainless Steel at Room Temperature," *Journal of Engineering Materials and Technology*, Vol. 105, p. 250.

Ellis, J.R. and Robinson, D.N.[1985], "Experimental Determination of Flow Potential Surfaces Supporting a Multiaxial Formulation of Viscoplasticity," *NASA Conference Publication 2405: Turbine Engine Hot Section Technology*, p. 259.

Eshelby, J.B.[1951]. "The Force on an Elastic Singularity," *Philosophical Transactions of the Royal Society*, London, Vol. 87, p. 12.

Eshelby, J.B.[1956]. "The Continuum Theory of Lattice Defects," F. Seitz and D. Turnbull (eds.), Solid State Physics., Academic Press, New York, p. 3.

Frantziskonis, G., Desai, C.S., and Somasundaram, S.[1986]. "Constitutive Model for Non-Associative Behavior," *Journal of Engineering Mechanics*, Vol. 112, no. 9, p. 932.

Freed, A.D., Chaboche, J.L., and Walker, K.P.[1991]. "A Viscoplastic Theory with Thermodynamic Considerations," *Acta Mechanica*, Vol. 90, p. 155.

Freed, A.D. and Walker, K.P.[1995]. "Viscoplastic model development with an eye toward characterization," *Journal of Engineering Materials and Technology*, Vol. 117, p. 8.

Gil, C.M., Lissenden, C.J., and Lerch, B.A.[1999a]. "Unusual nonlinear response of some metallic materials," *Mechanics of Materials* , Vol. 31, no. 9, p. 565.

Gil, C.M., Lissenden, C.J. Lerch, B.A.[1999b]. "Yield of Inconel 718 by axial-torsional loading at temperatures up to 649°C," *Journal of Testing and Evaluation*, Vol. 27, no. 5,

p. 327.

Hecker, S.S.[1971]. "Yield Surfaces in Prestrained Aluminum and Copper," *Metallurgical Transactions*, Vol. 2, p. 2077.

Hecker, S.S.[1976]. "Experimental Studies of Yield Phenomenon in Biaxially Loaded Metals," *Constitutive Equations in Viscoplasticity, Computational and Engineering Aspects*, ASME, pp.1.

Helling, D.E. and Miller, A.K.[1987]. "The incorporation of yield surface distortion into a unified constitutive model, Part 1: Equation development," *Acta Mechanica*, Vol. 69, p. 9.

Hill, R.[1950]. The mathematical theory of plasticity. Oxford University Press, New York.

Hirth, J.P. and Cohen, M.[1970]. "On the strength differential phenomenon in hardened steel," *Metallurgical Transactions*, Vol. 1, p. 3.

Hopkins, S.E.[1990]. "A Unified Multiaxial J_2, J_3 Theory of Viscplasticity for High-Temperature Isotropic Materials," *Master's Thesis*, University of Akron, Ohio.

Iyer, S.K. and Lissenden, C.J.[2000a]. "Local and Overall Flow Surfaces for Composites Predicted by Micromechanics," *Composites B: Engineering*, Vol. 31, p. 327.

Iyer, S.K. and Lissenden, C.J.[2000b]. "Inelastic Anisotropy of Inconel 718: Experiments and Mathematical Representation," *Journal of Engineering Materials and Technology*, Trans. ASME, Vol. 122, p. 321.

Janosik, L.A. and Duffy, S.F.[1997]. "A Viscoplastic Constitutive Theory for Monolithic Ceramic Materials - I," *NASA Conference Publication, Materials Processing, Characterization and Modeling (PPM) and Other Propulsion, Research and Technology, Part 1 (of 2), no. 10193/1*, NASA Lewis Research Center, Cleveland, Ohio.

Jesser, W.A. and Kuhlmann-Wilsdorf, D.[1972]. "Flow Stress and Dislocation Structure of Ni Deformed at Very High Pressure," *Material Science and Engineering*, Vol. 9, p. 111.

Jung, J.[1981]. "A Note on the Influence of Hydrostatic Pressure on Dislocations," *Philosophical Magazine*, A43, no. 4, p. 1057.

Kachanov, L.M.[1986]. Introduction to Continuum Damage Mechanics. Martinus Nijhoff, Boston, MA.

Kalish, D. and Cohen, M.[1969]. "Anisotropy of properties in martensite as developed by thermomechanical treatments," *Trans. ASM*, Vol. 62, no. 2. p. 353.

Kalluri, S. and Bonacuse, P.J.[1990]. "A Data Acquisition and Control Program for Axial-Torsional Fatigue Testing," Applications of Automation Technology to Fatigue and Fracture Testing, ASTM STP 1092, A.A. Brown, N.E. Ashbaugh, and F.M. Smith (eds.), *American Society for Testing and Materials*, Philadelphia, p. 269.

Kang, H.D. and Willam, J.[1999]. "Localization Characteristics of Triaxial Concrete Model," *Journal of Engineering Mechanics*, Vol. 125, no. 8, p. 941.

Khan, A. and Wang, X.[1993]. "An Experimental Study on Subsequent Yield Surfaces after Finite Shear Prestraining," *International Journal of Plasticity*, Vol. 9, p. 889.

Khan, A. and Huang, S.[1995]. Continuum Theory of Plasticity. John Wiley and sons, New York.

Lee, Y.K. and Ghosh, J.[1996]. "The Significance of J_3 to the Prediction of Shear Bands," *International Journal of Plasticity*, Vol. 12, p. 1179.

Lemaitre, J. and Chaboche, J.L.[1990]. Mechanics of Solid Materials. Cambridge University Press, New York.

Leslie, W.C. and Sober, R.J.[1967]. "The strength of ferrite and of martensite as functions of compositions, temperature and strain rate," *Trans. ASM*, Vol. 60, no. 3, p. 459.

Lewandowski, J.J. and Lowhaphandu, P.[1998]. "Effects of Hydrostatic Pressure on Mechanical Behavior and Deformation Processing of Materials, *International Materials Review*, Vol. 43, no. 4, p. 145.

Lissenden, C.J. and Arnold, S.M.[1997a]. "Theoretical and Experimental Considerations in Representing Macroscale Flow/Damage Surfaces for Metal Matrix Composites," *International Journal of Plasticity*, Vol. 13, no. 4, p. 327.

Lissenden, C.J., Lerch, B.A., Ellis, J.R., and Robinson, D.N.[1997b]. "Experimental Determination of yield and Flow Surfaces Under Axial-Torsional Loading," Multiaxial Fatigue and Deformation Testing Techniques, ASTM STP 1280, S. Kalluri and P.J. Bonacuse (eds.), *American Society for Testing and Materials*, p. 92.

Lissenden, C.J., Gil, C.M., and Lerch, B.A.[1999]. "A Methodology for Determining Rate-Dependent Flow Surfaces for Inconel 718," *Journal of Testing and Evaluation*, Vol. 27, no. 6, p. 402.

Lissenden, C.J., Arnold, S.M., and Iyer, S.K.[2000]."Flow/Damage Surfaces for Fiber Reinforced Metals Having Different Periodic Microstructures," *International Journal of Plasticity*, Vol. 16, p. 1049.

Lubliner, J.[1972]. "On the Thermodynamic Foundations of Nonlinear Solid Mechanics," *International Journal of Non-linear Mechanics*, Vol. 7, p. 237.

Lubliner, J.[1973]. "On the Structure of Rate Equations of Materials with Internal Variables," *Acta Mechanica*, Vol. 17, p. 109.

Lubliner, J.[1990]. Plasticity Theory. Macmillan, New York.

Maier, G. and Novati, G.[1990], "Extremum Theorems for Finite Step Backward Difference Analysis of Elastic-Plastic Non-Linearly Hardening Solids," *International Journal of Plasticity*, Vol. 6, p. 1.

Malvern, L.E.[1969]. Introduction to the Mechanics of a Continuous Medium. Prentice Hall, Englewood Cliffs, NJ.

Mandl, G. and Luque, R.F.[1970]. "Fully Developed Plastic Shear Flow of Granular Materials," *Geotechnique*, Vol. 20, no. 3, p. 277.

Mannan, S.L. and Rodriguez, P.[1973]. "Strength Differential Effect in Zirconium Alloys," *Scripta Metallurgica*, Vol. 7, no. 10, p. 1069.

Mendelson, A.[1983]. Plasticity: Theory and Application. Kreiger, Malabar.

Michno, M.J. and Findley, W.N.[1974]. "Subsequent Yield Surfaces for Annealed Mild

Steel Under Dead-Weight Loading: Aging, Normality, Convexity, Corners, Bauschinger, and Cross Effects," *Journal of Engineering Materials and Technology*, Vol. 96, p. 56.

Michno, M.J. and Findley, W.N.[1976]. "A Historical Perspective of Yield Surface Investigations for Metals," *International Journal of Nonlinear Mechanics*, Vol. 11, p. 59.

Miller, A.K.(ed.)[1987]. Unified Constitutive Equations for Plastic Deformation and Creep of Engineering alloys. Elsevier Applied Science, New York.

Miller, I., Freund, J.E., and Johnson, R.A.[1990]. Probability and Statistics for Engineers. Englewood Cliffs, Prentice Hall, NJ.

Mroz, Z.[1963]. "Non-Associated Flow Law in Plasticity," *Journal de Mechanique*, Vol. 2, no. 1.

Naghdi, P.M., Essenburg, F., and Koff, W.[1958], "An Experimental Study of Initial and Subsequent Yield Surfaces in Plasticity," *Journal of Applied Mechanics*, Vol. 25, no. 2, p. 201.

Oblak, J.M., Paulonis, D.F., and Duvall, D.S.[1974]. "Coherency Strengthening in Ni Base Alloys Hardened by DO_{22} γ'' Precipitates," *Metallurgical Transactions*, Vol. 5, p. 143.

Olsen, R.J. and Ansell, G.S.[1969]. "The Strength Differential in Two Phase Alloys," *Trans. ASM*, Vol. 62, no. 3, pp 711.

Onat, E.T. and Leckie, F.A.[1988]. "Representation of Mechanical Behavior in Presence of Changing Internal Structure," *Journal of Applied Mechanics*, Vol. 55, p. 1.

Osgood, W.R.[1947]. "Combined-Stress Tests on 24S-T Aluminum Alloy Tubes," Journal of Applied Mechanics, *Trans. ASME*, Vol. 69, p. A-147.

Paulonis, D.F., Oblak, J.M., and Duvall, D.S.[1969]. "Precipitation in Nickel-Base Alloy 718," *Trans. ASM*, Vol. 62, p. 611.

Pampillo, C.A. and Davis, L.A.[1972]. "The Effective Modulus Interpretation of the Strength-Differential Effect in Ferrous Alloys," *Scripta Metallurgica*, Vol. 6, no. 8, p. 765.

Phillips, A.[1957]. "An Experimental Investigation of Plastic Stress-Strain Relations ,",

Proceedings of the Ninth International Congress of Applied Mechanics, Vol. 8, p. 23.

Phillips, A. and Gray, G.A.[1961]. "Experimental Investigation of Corners in the Yield Surface," *Journal of Basic Engineering*, Vol. 83, p. 275.

Phillips, A. and Tang, J.L.[1972]. "The Effect of Loading Path on the Yield Surface at Elevated Temperatures," *International Journal of Plasticity*, Vol. 8, p. 463.

Phillips, A. and Moon, H.[1977]. "An Experimental Investigation Concerning Yield Surfaces and Loading Surfaces," *Acta Mechanica*, Vol. 27, p. 91.

Phillips, A. and Lu, W.[1984]. "An Experimental Investigation of Yield Surfaces and Loading Surfaces of Pure Aluminum with Stress-Controlled and Strain-Controlled Paths of Loading," *Journal of Engineering Materials and Technology*, Trans. ASME, Vol. 106, p. 349.

Plietsch, R. and Ehrlich, K.[1997]. "Strength Differential Effect in Pseudo-elastic Ni-Ti Shape Memory Alloys," *Acta Metallurgica*, Vol. 45, no. 6, p. 2417.

Ponter, A.R.S.[1976]. "Convexity and Associated Continuum Properties of a Class of Constitutive Relationships," *Eur. J. Mech. A. Solids*, Vol. 15, p. 527.

Ponter, A.R.S. and Leckie, F.A.[1976]. "Constitutive Relations for the Time-Dependent Deformation of Metals," *Journal of Engineering Materials and Technology*, Vol. 98, p. 47.

Ponter, A.R.S.[1979]. "General Theorems for Dynamic Loading of Structures for a State Variable Description of Material Behavior," *Inst. Phys. Conf. Ser.*, Vol. 47, p. 130.

Ponter, A.R.S.[1980]. "Dynamic Behavior of Structures Composed of Strain and Work-Hardening Viscoplastic Materials," *International Journal of Solids and Structures*, Vol. 16, p. 793.

Radcliffe, S.V. and Leslie, W.C.[1969]. "The Extent and Nature of the Strength-Differential Effect in Steels," *Journal of Metals*, Vol. 21, no. 3, p. 279.

Rauch, G.C. and Leslie, W.C.[1972]. "The extent and nature of strength differential effect in steels," *Metallurgical Transactions*, Vol. 3, no. 2, p. 373.

Rauch, G. C., Daga, R. L., Radcliffe, S. V., Sober, R. J., and Leslie, W. C.[1975]. "Volume

Expansion, Pressure Effects, and the Strength Differential in as-quenched Iron-Carbon Martensite," *Metallurgical Transactions*, Vol. 6A, no. 12, p. 2279.

Robinson, D.N.[1985]. "On Thermomechanical Testing in Support of Constitutive Equation Development for High-Temperature Alloys," *NASA-CR-174879, NASA Lewis Research Center*, Cleveland, Ohio.

Robinson, D.N. and Ellis, J.R.[1986]. "A Multiaxial Theory of Viscoplasticity for Isotropic Materials," *NASA Conference Publication 2444: Turbine Engine Hot Section Technology*, p. 283.

Robinson, D.N. and Duffy, S.F.[1990]. "Continuum deformation theory for high-temperature metallic composites," *ASCE Journal of Engineering Mechanics*, Vol. 116, p. 832.

Rice, J.R.[1968]. "A Path-Independent Integral and the Approximate Analysis of Strain Concentrations by Notches and Cracks," *Journal of Applied Mechanics*, Vol. 35, p. 379.

Rice, J.R.[1970]. "On the Structure of Stress-Strain Relations for Time-Dependent Plastic Deformation in Metals," *Journal of Applied Mechanics*, Vol. 37, p. 728.

Rice, J.R.[1971]. "Inelastic Constitutive Relations for Solids: An Internal-Variable Theory and its Application to Metal Plasticity ," *Journal of Mechanics and Physics of Solids*, Vol. 19, p. 433.

Saleeb, A.F., Chang, T.Y., Graf, W., and Yingyeunyong, S.[1990]. "A Hybrid/Mixed Model for Nonlinear Shell Analysis and its Application to Large Rotation Problems," *International Journal for Numerical Methods in Engineering*, Vol. 29, p. 407.

Saleeb, A.F and Wilt, T.E.[1993]. "Analysis of the Anisotropic Viscoplastic Damage Response of Composite Laminates - Continuum Basis and Computational Algorithms," *International Journal for Numerical Methods in Engineering*, Vol. 39, p. 1629.

Saleeb , A.F., Gendy, A.S., Wilt, T.E., and Trowbridge, D.A.[1998], "Constitutive Material Parameter Estimator," User's Guide, The University of Akron, Ohio.

Schittkowski, K.[1981]. "The Nonlinear Programming Method of Wilson, Han and Powell with an Augmented Lagrangian Type Line Search Function," *Numerische Mathematik*,

Vol. 38, no. 1, p. 83.

Schmid, E.[1924]. "Neuere Untersuschungen an Metallkristallen," *Proceedings of the First International Congress of Applied Mechanics*, Waltman, Delft, p. 342.

Spencer, A.J.M. and Rivlin, R.S.[1962]. "Isotropic integrity bases for vectors and second-order tensors," *Archive for Rational Mechanics and Analysis*, Vol. 9, p. 45.

Spitzig, W.A., Sober, R.J., and Richmond, O.[1975]. "Pressure Dependence of Yielding and Associated Volume Expansion in Tempered Martensite," *Acta Metallurgica*, Vol. 23, p. 885.

Spitzig, W.A., Sober, R.J., and Richmond, O.[1976]. "Effect of Hydrostatic Pressure on the Deformation Behavior of Maraging and HY-80 Steels and its Implications for Plasticity Theory," *Acta Metallurgica*, Vol. 7A, p. 1703.

Spitzig, W.A.[1979]. " Effect of Hydrostatic Pressure on Plastic-Flow Properties of Iron Single Crystals," *Acta Metallurgica*, Vol. 27, no. 4, pp.523.

Spitzig, W.A. and Richmond, O.[1981]. "Deformation Behavior of Nitrogenated Fe-Ti-Mn and Fe-Ti single crystals," *Acta Metallurgica*, Vol. 29, no. 8, p. 1359.

Spitzig, W.A. and Richmond, O.[1984]. "Effect of Pressure on the Flow Stress of Metals," *Acta Metallurgica*, Vol. 32, no. 3, p. 457.

Sundararaman, M., Mukhopadhyay, P., and Banerjee, S.[1988]. "Deformation Behavior of γ'' Strengthened Inconel 718," *Acta Metallurgica*, Vol. 36. no. 4, p. 847.

Taylor, G.I. and Quinney, H.[1931]. "The Plastic Distortion of Metals," *Philosophical Transactions of the Royal Society*, London, Vol. A320, p. 323.

Walker, K.P.[1981]. "Research and development program for nonlinear structural modeling with advanced time-temperature dependent constitutive relationship," *NASA CR-165533.*

Wegener, K. and Schlegel, M.[1996]. "Suitability of Yield Functions for the Approximation of Subsequent Yield Surfaces," *International Journal of Plasticity*, Vol. 12, no. 9, p. 1151.

Willam, K.J. and Warnke, E.P.[1975]. "Constitutive Model for Triaxial Behavior of Concrete,"

International Association for Bridge Structure Engineering Proceedings, Vol. 19, p. 1.

William, J.F. and Svensson, N.L.[1970]. "The Effect of Tensile Prestrain on the Yield Locus of 1100 F Aluminum," *Journal of Strain Analysis*, Vol. 5, p. 128-139.

William, J.F. and Svensson, N.L.[1971]. "The Effect of Torsional Prestrain on the Yield Locus of 1100 F Aluminum," *Journal of Strain Analysis*, Vol. 6, p. 263.

Winstone, M.R., Wright, M.L., and Rawlings, R.D.[1973]. "The Strength Differential in Some Titanium alloys," *Scripta Metallurgica*, Vol. 7, no. 12, p. 1265.

Wu, Han C. and Yeh, Wei C.[1991]. "On the Experimental Determination of Yield Surfaces and Some Results of Annealed 304 Stainless Steel," *International Journal of Plasticity*, Vol. 7, p. 803.

Zhou, L.X. and Baker, T.N.[1994]. "Effects of Strain-Rate and Temperature on Deformation Behavior of Inconel 718 During High-Temperature Deformation," *Material Science and Engineering*, A177, p. 1.

Appendix A

Formulation with Generalized Threshold Function

A.1 Flow Law and Evolution Law

Dissipation Potential

$$\Omega \;=\; \kappa^2 \left[\frac{1}{2\mu} \frac{\langle F \rangle^{n+1}}{(n+1)} \;+\; \frac{R}{H} \frac{\langle G \rangle^{m+\beta+1}}{(m+\beta+1)} \right]$$

Gibb's Potential

$$\Phi \;=\; \frac{1}{2}\sigma_{ij}\epsilon_{ij} \;-\; \frac{\kappa^2}{(1+\beta)H} G^{\beta+1}$$

Generalized Functions

$$F = [a\ \tilde{I}_1^{2m_1} + b\ \tilde{J}_2^{m_1} + c\ \tilde{J}_3^{\frac{2m_1}{3}}]^{\frac{1}{m_1}} - 1.$$

$$G = [a{I'_1}^{2m_1} + b{J'_2}^{m_1} + c{J'_3}^{\frac{2m_1}{3}}]^{\frac{1}{m_1}}$$

Effective Stress Invariants

$$\begin{aligned} \tilde{I}_1 &= \sigma_{ii} - \alpha_{ii} \\ \tilde{J}_2 &= \frac{1}{2}\Sigma_{ij}\Sigma_{ij} \\ \tilde{J}_3 &= \frac{1}{3}\Sigma_{ij}\Sigma_{jk}\Sigma_{ki} \end{aligned}$$

Internal Stress Invariants

$$
\begin{aligned}
I_1' &= \alpha_{ii} \\
J_2' &= \frac{1}{2} a_{ij} a_{ij} \\
J_3' &= \frac{1}{3} a_{ij} a_{jk} a_{ki}
\end{aligned}
$$

Derivatives of generalized functions with respect to invariants

$$
\begin{aligned}
\frac{\partial F}{\partial \tilde{I}_1} &= 2aF^{1-m_1} \tilde{I}_1^{2m_1-1} \\
\frac{\partial F}{\partial \tilde{J}_2} &= bF^{1-m_1} \tilde{J}_2^{m_1-1} \\
\frac{\partial F}{\partial \tilde{J}_3} &= \frac{2c}{3} F^{1-m_1} \tilde{J}_3^{2m_1/3-1} \\
\frac{\partial^2 G}{\partial {I_1'}^2} &= 2aG^{1-m_1} {I_1'}^{2m_1-1} \\
\frac{\partial^2 G}{\partial {J_2'}^2} &= bG^{1-m_1} {J_2'}^{m_1-1} \\
\frac{\partial^2 G}{\partial {J_3'}^2} &= \frac{2c}{3} G^{1-m_1} {J_3'}^{2m_1/3-1}
\end{aligned}
$$

Derivatives of effective invariants with respect to stress

$$
\begin{aligned}
\frac{\partial \tilde{I}_1}{\partial \sigma_{ij}} &= \delta_{ij} \\
\frac{\partial \tilde{J}_2}{\partial \sigma_{ij}} &= \Sigma_{ij} \\
\frac{\partial \tilde{J}_3}{\partial \sigma_{ij}} &= \Sigma_{iq}\Sigma_{jq} - \frac{2}{3}\tilde{J}_2 \delta_{ij}
\end{aligned}
$$

$$
\begin{aligned}
\frac{\partial \tilde{I}_1}{\partial \alpha_{ij}} &= -\delta_{ij} \\
\frac{\partial \tilde{J}_2}{\partial \alpha_{ij}} &= -\Sigma_{ij} \\
\frac{\partial \tilde{J}_3}{\partial \alpha_{ij}} &= -\Sigma_{iq}\Sigma_{jq} + \frac{2}{3}\tilde{J}_2 \delta_{ij}
\end{aligned}
$$

Derivatives of internal invariants with respect to stress

$$\begin{aligned}\frac{\partial I_1'}{\partial \alpha_{ij}} &= \delta_{ij} \\ \frac{\partial J_2'}{\partial \alpha_{ij}} &= a_{ij} \\ \frac{\partial J_3'}{\partial \alpha_{ij}} &= a_{iq}a_{jq} - \frac{2}{3}J_2'\delta_{ij}\end{aligned}$$

Derivatives of generalized functions with respect to stress

$$\begin{aligned}\frac{\partial F}{\partial \sigma_{ij}} &= \frac{\partial F}{\partial \tilde{I}_1}\frac{\partial \tilde{I}_1}{\partial \sigma_{ij}} + \frac{\partial F}{\partial \tilde{J}_2}\frac{\partial \tilde{J}_2}{\partial \sigma_{ij}} + \frac{\partial F}{\partial \tilde{J}_3}\frac{\partial \tilde{J}_3}{\partial \sigma_{ij}} \\ &= (F+1)^{1-m_1}\Upsilon_{ij}\end{aligned} \tag{A.1}$$

where

$$\Upsilon_{ij} = (2a\tilde{I}_1^{2m_1-1} - \frac{4}{9}c\tilde{J}_2\tilde{J}_3^{\frac{2}{3}m_1-1})\delta_{ij} + b\tilde{J}_2^{m_1-1}\Sigma_{ij} + \frac{2}{3}c\tilde{J}_3^{\frac{2}{3}m_1-1}\Sigma_{iq}\Sigma_{jq}$$

$$\frac{\partial F}{\partial \alpha_{ij}} = -\frac{\partial F}{\partial \sigma_{ij}}$$

$$\frac{\partial G}{\partial \alpha_{ij}} = G^{1-m_1}\Theta_{ij} \tag{A.2}$$

where

$$\Theta_{ij} = (2aI_1'^{2m_1-1} - \frac{4}{9}cJ_2'J_3'^{\frac{2}{3}m_1-1})\delta_{ij} + bJ_2'^{m_1-1}a_{ij} + \frac{2}{3}cJ_3'^{\frac{2}{3}m_1-1}a_{iq}a_{jq}$$

Flow Law

$$\begin{aligned}\dot{\epsilon}_{ij} &= \frac{\partial \Omega}{\partial \sigma_{ij}} \\ &= \frac{\kappa^2}{2\mu}F^n\frac{\partial F}{\partial \sigma_{ij}}\end{aligned}$$

Substituting from equation A.1

$$\dot{\epsilon}_{ij} = \frac{\kappa^2}{2\mu}F^n(F+1)^{1-m_1}\Upsilon_{ij}$$

Evolution Law

$$\begin{aligned}\dot{\Lambda}_{ij} &= -\frac{\partial \Omega}{\partial \alpha_{ij}} \\ &= -\frac{\kappa^2}{2\mu}F^n\frac{\partial F}{\partial \sigma_{ij}} + \frac{\kappa^2 R}{H}G^{m+\beta}\frac{\partial G}{\partial \alpha_{ij}}\end{aligned}$$

Substituting from equation A.1 and A.2

$$\dot{\Lambda}_{ij} = \dot{\epsilon}^I_{ij} - \frac{\kappa^2 R}{H} G^{(1+\beta+m-m_1)} \Theta_{ij}$$

Internal Compliance

$$\begin{aligned} Q_{ijkl} &= -\frac{\partial^2 \Phi}{\partial \alpha_{ij} \partial \alpha_{kl}} \\ &= \frac{\kappa^2}{H} \frac{\partial [G^\beta \frac{\partial G}{\partial \alpha_{kl}}]}{\partial \alpha_{ij}} \\ &= \frac{\kappa^2 m_1}{H} \frac{\partial [G^{1+\beta-m_1} \Theta_{kl}]}{\partial \alpha_{ij}} \\ &= \frac{\kappa^2}{H} G^{1+\beta-m_1} \left[\frac{\partial \Theta_{kl}}{\partial \alpha_{ij}} + \frac{1+\beta-m_1}{G_1^m} \Theta_{ij} \Theta_{kl} \right] \end{aligned}$$

Each term in Θ_{kl} is differentiated by parts and the final expression for the internal compliance tensor is

$$\begin{aligned} &Q_{ijkl} = \qquad (A.3) \\ &\frac{\kappa^2}{H} G^{(1+\beta-m_1)} [(2a(2m_1-1) {I'_1}^{2m_1-2} - \frac{b}{3} {J'_2}^{m_1-1} + \frac{8c}{27}(\frac{2}{3}m_1 - 1) {J'_2}^2 {J'_3}^{\frac{2}{3}m_1-2}) \delta_{ij}\delta_{kl} \\ &+ b(m_1-1) {J'_2}^{m_1-2} a_{ij}a_{kl} + b {J'_2}^{m_1-1} \delta_{ik}\delta_{jl} \\ &+ \frac{2c}{3} {J'_3}^{\frac{2}{3}m_1-1} (a_{il}\delta_{kj} + a_{jl}\delta_{ik} - \frac{2}{3}a_{ij}\delta_{kl} + (\frac{2}{3}m_1 - 1)\frac{1}{J'_3}(a_{iq}a_{jq}a_{kp}a_{lp} - \frac{2J'_2}{3}a_{iq}a_{jq}\delta_{kl})) \\ &- \frac{4c}{9} {J'_3}^{\frac{2}{3}m_1-1} ((\frac{2}{3}m_1 - 1)\frac{J'_2}{J'_3} a_{kp}a_{lp}\delta_{ij} + a_{kl}\delta_{ij}) + \left(\frac{1+\beta-m_1}{G^{m_1}} \right) \Theta_{ij}\Theta_{kl}] \end{aligned}$$

Simplification for deviatoric models

For models not involving $\tilde{I}_1$ (hydrostatic pressure-independent material) the δ_{kl} is inconsequential in the internal constitutive rate equation because

$$\delta_{kl}\dot{\alpha}_{kl} = \dot{\alpha}_{kk} = 0$$

Thus the terms with δ_{kl} can be dropped and the internal compliance tensor simplifies to

$$
\begin{aligned}
Q_{ijkl} = & \\
& \frac{\kappa^2}{H} G^{(1+\beta-m_1)} [b(m_1-1) {J_2'}^{m_1-2} a_{ij} a_{kl} + b {J_2'}^{m_1-1} \delta_{ik} \delta_{jl} \\
& + \frac{2c}{3} {J_3'}^{\frac{2}{3}m_1-1} (a_{il}\delta_{kj} + a_{jl}\delta_{ik} + (\frac{2}{3}m_1 - 1)\frac{1}{J_3'} a_{iq} a_{jq} a_{kp} a_{lp}) \\
& - \frac{4c}{9} {J_3'}^{\frac{2}{3}m_1-1} ((\frac{2}{3}m_1 - 1)\frac{J_2'}{J_3'} a_{kp} a_{lp} \delta_{ij} + a_{kl}\delta_{ij}) \\
& + \left(\frac{1+\beta-m_1}{G^{m_1}} \right) \Theta_{ij} (b {J_2'}^{m_1-1} a_{kl} + \frac{2}{3} c {J_3'}^{\frac{2}{3}m_1-1} a_{kq} a_{lq})]
\end{aligned}
$$

Stress transformation to principal plane

Transformation of stresses from the axial-shear plane to the principal plane facilitated the numerical inversion of the internal compliance tensor (Q_{ijkl}) for loadings that start with shear.

A.2 Contracted Notation

Various tensors in the formulation have been changed to contracted notation for ease of programming.

$$\delta_{ij} = \begin{bmatrix} 1 & 1 & 1 & 0 & 0 & 0 \end{bmatrix}$$

$$\Sigma_{ij} = \begin{bmatrix} \Sigma_{11} & \Sigma_{22} & \Sigma_{33} & \Sigma_{23} & \Sigma_{31} & \Sigma_{12} \end{bmatrix}$$

$$a_{ij} = \begin{bmatrix} a_{11} & a_{22} & a_{33} & a_{23} & a_{31} & a_{12} \end{bmatrix}$$

$$\Sigma_{iq}\Sigma_{jq} = \begin{bmatrix} \Sigma_{11}^2 + \Sigma_{12}^2 + \Sigma_{13}^2 \\ \Sigma_{21}^2 + \Sigma_{22}^2 + \Sigma_{23}^2 \\ \Sigma_{31}^2 + \Sigma_{32}^2 + \Sigma_{33}^2 \\ \Sigma_{12}\Sigma_{13} + \Sigma_{22}\Sigma_{23} + \Sigma_{32}\Sigma_{33} \\ \Sigma_{11}\Sigma_{13} + \Sigma_{12}\Sigma_{23} + \Sigma_{13}\Sigma_{33} \\ \Sigma_{11}\Sigma_{12} + \Sigma_{12}\Sigma_{22} + \Sigma_{13}\Sigma_{32} \end{bmatrix}^T$$

$$a_{iq}a_{jq} = \begin{bmatrix} a_{11}^2 + a_{12}^2 + a_{13}^2 \\ a_{21}^2 + a_{22}^2 + a_{23}^2 \\ a_{31}^2 + a_{32}^2 + a_{33}^2 \\ a_{12}a_{13} + a_{22}a_{23} + a_{32}a_{33} \\ a_{11}a_{13} + a_{12}a_{23} + a_{13}a_{33} \\ a_{11}a_{12} + a_{12}a_{22} + a_{13}a_{32} \end{bmatrix}^T$$

$$\delta_{ik}\delta_{jl} = \begin{bmatrix} 1 & 0 & 0 & 0 & 0 & 0 \\ 0 & 1 & 0 & 0 & 0 & 0 \\ 0 & 0 & 1 & 0 & 0 & 0 \\ 0 & 0 & 0 & 1 & 0 & 0 \\ 0 & 0 & 0 & 0 & 1 & 0 \\ 0 & 0 & 0 & 0 & 0 & 1 \end{bmatrix}$$

$$a_{il}\delta_{kj} = \begin{bmatrix} a_{11} & 0 & 0 & 0 & 0 & a_{12} \\ 0 & a_{22} & 0 & a_{23} & 0 & 0 \\ 0 & 0 & a_{33} & 0 & a_{31} & 0 \\ 0 & 0 & a_{23} & 0 & a_{12} & 0 \\ a_{31} & 0 & 0 & 0 & 0 & a_{23} \\ 0 & a_{12} & 0 & a_{31} & 0 & 0 \end{bmatrix}$$

$$a_{jl}\delta_{ik} = \begin{bmatrix} a_{11} & 0 & 0 & 0 & 0 & a_{12} \\ 0 & a_{22} & 0 & a_{23} & 0 & 0 \\ 0 & 0 & a_{33} & 0 & a_{31} & 0 \\ 0 & a_{23} & 0 & a_{33} & 0 & 0 \\ 0 & 0 & a_{31} & 0 & a_{11} & 0 \\ a_{12} & 0 & 0 & 0 & 0 & a_{22} \end{bmatrix}$$

Appendix B

FORTRAN Program for Computing Material Response

```
      implicit double precision(a-h,o-z)
      common / one / q0,q1,q2,q3,q4
      common / six / xk,xmu,xn,ra,beta,xa,xb,xc,xm,xh,xm1,m
      common / eight / ctemp
      dimension sb(6),eb(6),a(6),epl(6),dep(6),adot(6),c(6,6),acap(6)
      dimension th(6),sig(6),dev(6),dp(6)
      q0 = 0.d0
      q1 = 1.d0
      q2 = 2.d0
      q3 = 3.d0
      q4 = 4.d0
      pi = q4*atan(q1)
      open (12,file='nn5.inp',status='old')
      open (13,file='gnew.dat',status='unknown')

c read current temperature and Poisson ratio
      read(12,*) ctemp,xnu
      call GVPROP(XK,XMU)
```

```
c read matrix temperature-independent GVIPS parameters
      read(12,*) xn,xh,beta,xm,ra
c read threshold surface parameters
      read(12,*) xa,xb,xc,xm1
c material properties (elastic)
      call ELPROPS(emod,alfa,c,xnu)
      gm = emod/(q1 + xnu)/q2
c read no. of load segments and probes
      read(12,*) nstep,ipro

      do 1000, m=1,nstep
      read(12,*) ttim,ninc,sigi,sigf,taui,tauf
      timinc = ttim/real(ninc)

      tau = taui
      siga = sigi
      deltau = tauf-taui
      delsig = sigf-sigi
      dtau=deltau/real(ninc)
      dsig=delsig/real(ninc)

      do 500, k=1,ninc
c Strain control loading
      eb(1) = siga
      siga = siga + dsig
      eb(2) = tau
      tau = tau + dtau
      ax = emod*(eb(1)-taxe)
      sh = q2*gm*(eb(2)-tshe)
c transformation to principal stress
sb(1)=ax/q2 + sqrt(ax**q2/q4 + sh**q2)
sb(2)=ax/q2 - sqrt(ax**q2/q4 + sh**q2)
```

```
      call GVIPS(sb,a,adot,dep,c,xj1,xj2,xj3,sig)
c calculate plastic strains
      do 60, i=1,6
        a(i) = a(i) + adot(i)*timinc
dp(i)=dep(i)*timinc
   60   epl(i) = epl(i) + dep(i)*timinc

      axe=q0
      she=q0
      theta=abs(q1/q2*atan(q2*sh/ax))
c transform principal inelastic strain increments to axial and shear components
      axe=q1/q2*(dp(1)+dp(2)+abs(dp(1)-dp(2))*cos(q2*theta))
      she=q1/q2*(dp(1)-dp(2))*sin(q2*theta)
c compute total inelastic strain
      taxe=taxe+axe
      tshe=tshe+she

       if(k/1000.0-int(k/1000.0).eq.q0)then
        write(13,9995) k,ctime,ax,sh,xj1,xj2,xj3,taxe,tshe
       endif

      ctime = ctime + timinc
  500 continue
 1000 continue
 9995 format(i8,9d12.4)
      stop
      end

c#######################################################################
      subroutine gvprop(kapa,xmu)
      implicit double precision (a-h,o-z)
```

```
      double precision kapa,kapa0
      common / eight / ctemp
        kapa = 234.7
        xmu = 1.7681d5
      return
      end
c#########################################################################
      subroutine elprops(emod,alfa,c,xnu)
c elastic stiffness tensor
      implicit double precision(a-h,o-z)
      common / one / q0,q1,q2,q3,q4
      common / eight / ctemp
      dimension c(6,6)
      emod = 165360.0
      xlam = xnu*emod/((q1 + xnu)*(q1 - q2*xnu))
      xmu = emod/(q2*(q1 + xnu))

      c(1,1) = xlam + q2*xmu
      c(2,2) = c(1,1)
      c(3,3) = c(1,1)
      c(1,2) = xlam
      c(1,3) = c(1,2)
      c(2,3) = c(1,2)
      c(2,1) = c(1,2)
      c(3,1) = c(1,3)
      c(3,2) = c(2,3)
      c(4,4) = xmu
      c(5,5) = xmu
      c(6,6) = xmu
      return
      end
C#########################################################################
```

```
      subroutine gvips(st,at,adot,dep,c,xj1,xj2,xj3,sig)
c Formulation with generalized threshold function
      implicit double precision(a-h,o-z)
      common / one / q0,q1,q2,q3,q4
      common / two / ctemp
      common / six / xk,xmu,xn,ra,beta,xa,xb,xc,xm,xh,xm1,m
      dimension st(6),dep(6),dev(6),sig(6),xl(6,6),at0(6)
      dimension acap(6),at(6),adot(6),c(6,6),xq(6,6),xq1(6,6)
      dimension xu(6),su(6),delta(6),xv(6,6),xw(6,6),yi(6,6)
      dimension pi(6),th(6),xu1(6),yi1(6,6),th1(6),pi1(6),dep1(6)
      dimension indx(6),th0(6),th2(6),p1(6,6),p2(6,6)

      if(xa.ne.q0)then
      at0(1) = (Q2*at(1) - at(2) - at(3))/Q3
      at0(2) = (Q2*at(2) - at(1) - at(3))/Q3
      at0(3) = (Q2*at(3) - at(2) - at(1))/Q3
      else
      at0(1)=at(1)
      at0(2)=at(2)
      at0(3)=at(3)
      endif
      at0(4) = at(4)
      at0(5) = at(5)
      at0(6) = at(6)

      xi1=at(1)+at(2)+at(3)
      ast=st(1)+st(2)

C deviatoric stress components
      dev(1) = (q2*st(1) - st(2) - st(3))/q3
      dev(2) = (q2*st(2) - st(1) - st(3))/q3
      dev(3) = (q2*st(3) - st(2) - st(1))/q3
```

```
      dev(4) = st(4)
      dev(5) = st(5)
      dev(6) = st(6)
C effective deviatoric stress components
      do 10, i=1,6
   10 sig(i) = dev(i) - at0(i)

c first effective invariant
        xj1=st(1)+st(2)+st(3)-xi1

        delta(1)=q1
        delta(2)=q1
        delta(3)=q1
        delta(4)=q0
        delta(5)=q0
        delta(6)=q0

su(1)= sig(1)**q2 + sig(6)**q2 + sig(5)**q2
su(2)= sig(2)**q2 + sig(4)**q2 + sig(6)**q2
su(3)= sig(3)**q2 + sig(4)**q2 + sig(5)**q2
su(4)= sig(6)*sig(5) + sig(2)*sig(4) + sig(3)*sig(4)
su(5)= sig(1)*sig(5) + sig(4)*sig(6) + sig(3)*sig(5)
su(6)= sig(1)*sig(6) + sig(2)*sig(6) + sig(4)*sig(5)

        xu1(1)= at0(1)**q2 + at0(6)**q2 + at0(5)**q2
xu1(2)= at0(2)**q2 + at0(4)**q2 + at0(6)**q2
xu1(3)= at0(3)**q2 + at0(4)**q2 + at0(5)**q2
xu1(4)= at0(6)*at0(5) + at0(2)*at0(4) + at0(3)*at0(4)
xu1(5)= at0(1)*at0(5) + at0(4)*at0(6) + at0(3)*at0(5)
xu1(6)= at0(1)*at0(6) + at0(2)*at0(6) + at0(4)*at0(5)

do 12, i=1,6
```

```
      do 12, j=1,6
         xv(i,j)=q0
         xw(i,j)=q0
         if(i.eq.j)then
         yi(i,j)=q1
         else
             yi(i,j)=q0
                 endif
      12   continue

c 2nd & 3rd effective invariant
         XI2 = Q0
         XJ2 = Q0
         XI3 = Q0
         XJ3 = Q0

         DO 20, I=1,3
         XI3 = XI3 + Q1*(at0(I)*xu1(I)+q2*at0(i+3)*xu1(I+3))/Q3
      20 XJ3 = XJ3 + Q1*(sig(I)*su(I)+q2*sig(I+3)*su(i+3))/Q3

         DO 21, I=1,3
         XI2 = XI2 + Q1*(at0(I)*at0(I)/Q2 + at0(I+3)*at0(I+3))
      21 XJ2 = XJ2 + Q1*(SIG(I)*SIG(I)/Q2 + SIG(I+3)*SIG(I+3))

         sxj1=q1
         sxj3=q1
         if(xj1.lt.q0)sxj1=-q1
         if(xj3.lt.q0)sxj3=-q1

c setting minimum values for internal invariants (Go for stability)
         if(xa.ne.q0.and.xc.ne.q0.and.ast.ne.q0)then
cong1=30.0
```

```
cong2=900.0
cong3=27000.0
      elseif(xa.ne.q0.and.xc.eq.q0.and.ast.ne.q0)then
        cong1=30.0
cong2=900.0
      elseif(xa.eq.q0.and.xc.ne.q0.and.ast.ne.q0)then
       cong2=900.0
       cong3=27000.0
      elseif(xa.eq.q0.and.xc.eq.q0.or.ast.eq.q0)then
       cong2=900.0
      endif

      if(xj2.eq.q0) return

      xek2 = xb*xj2**(xm1-q1)
      if(xc.ne.q0.and.ast.ne.q0)then
        xek3 = q2/q3*xc*sxj3*abs(xj3)**(q2/q3*xm1-q1)
      else
        xek3 = q0
      endif

      if(xa.ne.q0.and.xc.ne.q0.and.ast.ne.q0)then
       exe=xa*sxj1*abs(xj1)**(2*xm1)+xb*xj2**xm1+
     +    xc*sxj3*abs(xj3)**(2*xm1/3)
       xek1 = q2*xa*sxj1*abs(xj1)**(q2*xm1-q1)
     +       -4.0/9.0*xc*xj2*sxj3*abs(xj3)**(q2/q3*xm1-q1)
      elseif(xc.ne.q0.and.xa.eq.q0.and.ast.ne.q0)then
       exe=xb*xj2**xm1+xc*sxj3*abs(xj3)**(2*xm1/3)
       xek1 =-4.0/9.0*xc*xj2*sxj3*abs(xj3)**(q2/q3*xm1-q1)
      elseif(xa.ne.q0.and.xc.eq.q0.and.ast.ne.q0)then
       exe=xa*sxj1*abs(xj1)**(2*xm1)+xb*xj2**xm1
       xek1 = q2*xa*sxj1*abs(xj1)**(q2*xm1-q1)
```

```
      elseif(xa.eq.q0.and.xc.eq.q0.or.ast.eq.q0)then
       exe=xb*xj2**xm1
       xek1=q0
      endif

      do 123, i=1,6
  123    pi(i) = xek1*delta(i) + xek2*sig(i) + xek3*su(i)

c function F
      fcap =  (abs(exe))**(q1/xm1) - q1
      if(fcap.lt.q0) fcap = q0
      flit = fcap**xn

c inelastic strain rate tensor
      do 30, i=1,6
   30 dep(i) = xk*xk/q2/xmu*flit*(fcap+q1)**(q1-xm1)*pi(i)

      if(xa.ne.q0.and.xc.ne.q0.and.ast.ne.q0)then
        if(abs(xi1).lt.abs(cong1))xi1=cong1
        if(xi2.lt.cong2)xi2=cong2
        if(abs(xi3).lt.abs(cong3))xi3=cong3
      elseif(xa.ne.q0.and.xc.eq.q0.and.ast.ne.q0)then
        if(abs(xi1).lt.abs(cong1))xi1=cong1
if(xi2.lt.cong2)xi2=cong2
      elseif(xa.eq.q0.and.xc.ne.q0.and.ast.ne.q0)then
if(abs(xi3).lt.abs(cong3))xi3=cong3
if(xi2.lt.cong2)xi2=cong2
      elseif(xa.eq.q0.and.xc.eq.q0.or.ast.eq.q0)then
        if(xi2.lt.cong2)xi2=cong2
      endif

      sxi1=q1
```

```
      sxi3=q1

      if(xi1.lt.q0)sxi1=-q1
      if(xi3.lt.q0)sxi3=-q1

      if(xi2.gt.q0)then
      if(xc.eq.q0.and.xa.ne.q0)then
       gcap=xa*sxi1*abs(xi1)**(q2*xm1)+xb*xi2**xm1
      elseif(xa.eq.q0.and.xc.ne.q0.and.ast.ne.q0)then
       gcap=xb*xi2**xm1+xc*sxi3*abs(xi3)**(q2*xm1/q3)
      elseif(xc.ne.q0.and.xa.ne.q0.and.ast.ne.q0)then
       gcap=xa*sxi1*abs(xi1)**(q2*xm1)+xb*xi2**xm1
     +      +xc*sxi3*abs(xi3)**(q2*xm1/q3)
      elseif(xc.eq.q0.and.xa.eq.q0.or.ast.eq.q0)then
       gcap=xb*xi2**xm1
      endif
      endif
c function G
       gcap=(abs(gcap))**(q1/xm1)

 xik2 = xb*xi2**(xm1-q1)
         if(xc.ne.q0.and.ast.ne.q0)then
          xik3 = q2/q3*xc*sxi3*abs(xi3)**(q2/q3*xm1-q1)
         else
          xik3 = q0
 endif

 if(xc.ne.q0.and.xa.ne.q0.and.ast.ne.q0)then
         xik1 = q2*xa*sxi1*abs(xi1)**(q2*xm1-q1)
     +           -4.0/9.0*xc*xi2*sxi3*abs(xi3)**(q2/q3*xm1-q1)
         elseif(xc.ne.q0.and.xa.eq.q0.and.ast.ne.q0)then
         xik1 = -4.0/9.0*xc*xi2*sxi3*abs(xi3)**(q2/q3*xm1-q1)
```

```
        elseif(xa.ne.q0.and.xc.eq.q0.and.ast.ne.q0)then
        xik1 = q2*xa*sxi1*abs(xi1)**(q2*xm1-q1)
elseif(xc.eq.q0.and.xa.eq.q0.or.ast.eq.q0)then
xik1=q0
        endif

     do 122, i=1,6
        th1(i)=xik2*at0(i)+xik3*xu1(i)
 122    th(i) = xik1*delta(i) + xik2*at0(i) + xik3*xu1(i)



       xv(1,1)=at0(1)
       xv(1,6)=at0(6)
       xv(2,2)=at0(2)
       xv(2,4)=at0(4)
       xv(3,3)=at0(3)
       xv(3,5)=at0(5)
       xv(4,2)=at0(4)
       xv(4,4)=at0(3)
       xv(5,3)=at0(5)
       xv(5,5)=at0(1)
       xv(6,1)=at0(6)
       xv(6,6)=at0(2)

       xw(1,1)=at0(1)
       xw(1,6)=at0(6)
       xw(2,2)=at0(2)
       xw(2,4)=at0(4)
       xw(3,3)=at0(3)
       xw(3,5)=at0(5)
       xw(4,3)=at0(4)
       xw(4,5)=at0(6)
```

```
         xw(5,1)=at0(5)
         xw(5,6)=at0(4)
         xw(6,2)=at0(6)
         xw(6,4)=at0(5)

      if(xc.ne.q0.and.xa.ne.q0.and.ast.ne.q0)then
       z1 = q2*xa*(q2*xm1-q1)*sxi1*abs(xi1)**(q2*xm1-q2)
           +  - xb/q3*xi2**(xm1-q1)
           +  + 8.0*xc/27.0*(q2/q3*xm1-q1)*sxi3*abs(xi3)**
           +   (q2/q3*xm1-q2)*xi2*xi2
      elseif(xc.ne.q0.and.xa.eq.q0.and.ast.ne.q0)then
       z1=- xb/q3*xi2**(xm1-q1)
           +  + 8.0*xc/27.0*(q2/q3*xm1-q1)*sxi3*abs(xi3)**
           +   (q2/q3*xm1-q2)*xi2*xi2
         elseif(xa.ne.q0.and.xc.eq.q0.and.ast.ne.q0)then
          z1=q2*xa*(q2*xm1-q1)*sxi1*abs(xi1)**(q2*xm1-q2)
           +  -xb/q3*xi2**(xm1-q1)
      endif

         z2 = xb*(xm1-q1)*xi2**(xm1-q2)
         z3 = xb*xi2**(xm1-q1)

         if(xc.ne.q0.and.ast.ne.q0)then
          cn1 = sxi3*abs(xi3)**(q2*xm1/q3-q1)
          cn2 = sxi3*abs(xi3)**(q2*xm1/q3-q2)
         else
          cn1=q0
          cn2=q0
         endif
         cn3 = (q1-xm1+beta)/gcap**xm1

      c internal compliance tensor
```

```
      if(xa.eq.q0.and.xc.eq.q0.or.ast.eq.q0)then
      do 31, i=1,6
      do 31, j=1,6
         31   xq(i,j)=gcap**beta/xh*
           +          (beta/gcap/xk/xk*at0(i)*at0(j)+yi(i,j))
      elseif(xc.ne.q0.and.xa.eq.q0.and.ast.ne.q0)then
      do 32, i=1,6
            do 32, j=1,6
         32     xq(i,j) = xk*xk/xh*gcap**(beta+q1-xm1)*
           +      (z2*at0(i)*at0(j) + z3*yi(i,j)
           +    + cn1*q2*xc/q3*(xw(i,j)+xv(i,j)
           +       -q2/q3*delta(i)*at0(j))
           +    + cn2*q2*xc/q3*(q2*xm1/q3-q1)*(xu1(i)*xu1(j)
           +      -q2/q3*xi2*delta(i)*xu1(j))
           +    + cn3*th(i)*th1(j))
            elseif(xa.ne.q0.and.xc.eq.q0.and.ast.ne.q0)then
      do 33, i=1,6
            do 33, j=1,6
         33     xq(i,j) = xk*xk/xh*gcap**(beta+q1-xm1)*
           +     (z1*delta(i)*delta(j)
           +    + z2*at0(i)*at0(j) + z3*yi(i,j)
           +    + cn3*th(i)*th(j))
            elseif(xa.ne.q0.and.xc.ne.q0.and.ast.ne.q0)then
      do 34, i=1,6
            do 34, j=1,6
         34     xq(i,j) = xk*xk/xh*gcap**(beta+q1-xm1)*
           +     (z1*delta(i)*delta(j)
           +    + z2*at0(i)*at0(j) + z3*yi(i,j)
           +    + cn1*q2*xc/q3*(xw(i,j)+xv(i,j)-q2/q3*at0(i)*delta(j)
           +       -q2/q3*delta(i)*at0(j))
           +    + cn2*q2*xc/q3*(q2*xm1/q3-q1)*(xu1(i)*xu1(j)-
           +       q2*xi2/q3*xu1(i)*delta(j)-q2/q3*xi2*delta(i)*xu1(j))
```

```
     +    + cn3*th(i)*th(j))
        endif

c internal stiffness tensor
call invert(xq,6,6,xl)

c internal strain rate
do 70, i=1,6
   70    acap(i)=(dep(i)-ra*xk*xk/xh*
     +           gcap**(q1+beta+xm-xm1)*th(i))

c convert tensorial shear components to contracted (vector) components
      do 80, i=4,6
   80   acap(i) = q2*acap(i)

c internal constitutive rate equation
      do 90, i=1,6
      adot(i) = q0
      do 90, j=1,6
          adot(i) = adot(i) + xl(i,j)*acap(j)
   90 continue

C CONVERT CONTRACTED SHEAR COMPONENTS BACK TO TENSORIAL COMPONENTS
      DO 100, I=4,6
  100   ACAP(I) = ACAP(I)/Q2

      RETURN
      END

C*********************************************************************
       subroutine invert(a,n,m,d)
c        inverts n x n matrix a. result returned as array d
```

```
c        m is the dimensioned size of arrays a and d

      implicit double precision(a-h,o-z)
      dimension a(m,m),d(m,m),w(138,276)
      do 5 i=1,n
         do 5 j=1,n
            w(i,j)=a(i,j)
            if(i.eq.j) then
               w(i,j+n)=1.
            else
               w(i,j+n)=0.0d0
            end if
    5 continue
      do 50 k=1,n
         do 10 l=1,2*n-k+1
            j=2*n+1-l
            w(k,j)=w(k,j)/w(k,k)
   10    continue
         do 30 i=1,n
            if(i.eq.k) goto 30
            do 20 l=1,2*n-k+1
               j=2*n+1-l
               w(i,j)=w(i,j)-w(i,k)*w(k,j)
   20       continue
   30    continue
   50 continue
      do 60 i=1,n
         do 60 j=1,n
            d(i,j)=w(i,j+n)
   60 continue
      return
      end
```

Appendix C

MATLAB Program for Determining Convexity

```
m=1.0;
ij=1;
for sav=654:-4:-654
lc=1;
for c=2.2e-6
a=2.6e-7;
b=1.8154e-5;
i=1;
for lam=1:1:27
ik=i*ij;
k=0;
th=pi*lam/180;
rj2=(1-a*(9*sav^2)^m)/(b+c/3^m*(2*cos(3*th))^(2*m/3));
rj2=(abs(rj2))^(1/(2*m));

% principal stresses
s1=sav+2/sqrt(3)*rj2*cos(th);
s2=sav+2/sqrt(3)*rj2*cos(th-2*pi/3);
```

```
s3=sav+2/sqrt(3)*rj2*cos(th+2*pi/3);

% invariants
i1=s1+s2+s3;
j2=1/3*((s1-s2)^2+(s2-s3)^2+(s3-s1)^2);
j3=1/27*(2*s1-s2-s3)*(2*s2-s1-s3)*(2*s3-s1-s2);
snj3=1;
if j3 < 0
snj3=-1;
end

%derivatives for hessian matrix
d1=b*j2^(-1 + m)*m;
d3=b*j2^(-2 + m)*(-1 + m)*m;
d5=0;
if i1 == 0
d0=0;
d6=0;
else
d0=a*2*m*i1^(2*m-1);
d6=2*a*i1^(-2 + 2*m)*m*(-1 + 2*m);
end
if j3 == 0
d2=0;
d4=0;
else
d2=(2*c*snj3*(abs(j3))^(-1 + (2*m)/3.)*m)/3.;
d4=(2*c*snj3*(abs(j3))^(-2 + (2*m)/3.)*(-1 + (2*m)/3.)*m)/3.;
end
dj0=1;
dj1=1/3*(2*s1-s2-s3);
dj2=1/3*(2*s2-s1-s3);
```

```
dj3=1/9*(2*s1^2-s2^2-s3^2-2*s1*s2-2*s1*s3+4*s2*s3);
dj4=1/9*(2*s2^2-s1^2-s3^2-2*s1*s2-2*s2*s3+4*s1*s3);
dj5=2/3;
dj6=2/3;
dj7=2/9*(2*s1-s2-s3);
dj8=2/9*(2*s2-s1-s3);
dj9=-1/3;
dj10=2/9*(2*s3-s1-s2);
dj11=1;
dj12=1/3*(2*s3-s1-s2);
dj13=2/3;
dj14=-1/3;
dj15=-1/3;
dj16=1/9*(2*s3^2-s1^2-s2^2-2*s1*s3-2*s2*s3+4*s1*s2);
dj17=2/9*(2*s3-s1-s2);
dj18=2/9*(2*s2-s1-s3);
dj19=2/9*(2*s1-s2-s3);
m11=d6 + d1*dj5 + d3*dj1*dj1 + d2*dj7 + d4*dj3*dj3;
m12=d6 + d1*dj9 + d3*dj2*dj1 + d2*dj10+ d4*dj4*dj3;
m22=d6 + d1*dj6 + d3*dj2*dj2 + d2*dj8 + d4*dj4*dj4;
m13=d6 + d3*dj1*dj12 + d1*dj14 + d4*dj3*dj16 + d2*dj18;
m23=d6 + d3*dj2*dj12 + d1*dj15 + d4*dj4*dj16 + d2*dj19;
m33=d6 + d1*dj13 + d3*dj12^2 + d2*dj17 + d4*dj16^2;

% curvature tensor
x=[m11 m12 m13
m12 m22 m23
m13 m23 m33];
u1=d0 + d1*dj1 + d2*dj3;
u2=d0 + d1*dj2 + d2*dj4;
u3=d0 + d1*dj12+ d2*dj16;
du=(u1^2+u2^2+u3^2)^0.5;
```

```
% unit vector in tangential direction
u=[u1/du u2/du u3/du]';
bm=eye(3)-u*u';

% orthonormalization
[pm,s,v]=svd(bm);
q=pm(:,1:2);

% curvature in tangential direction
kur(i)=min(eig(q'*x*q));
kurr=kur(i);
l(i)=lam;
res(ik,1)=sav;
res(ik,2)=lam;
res(ik,3)=kurr;
if kur(i) < 0.0
lamc(ik)=lam;
str(ik)=sav;
kc(ik)=kurr;
cr(lc,ik)=c;
lc=lc+1;
end
k=k+1;
end
i=i+1;
end
ij=ij+1;
end
```

Appendix D

Correlation for Biaxial Loading

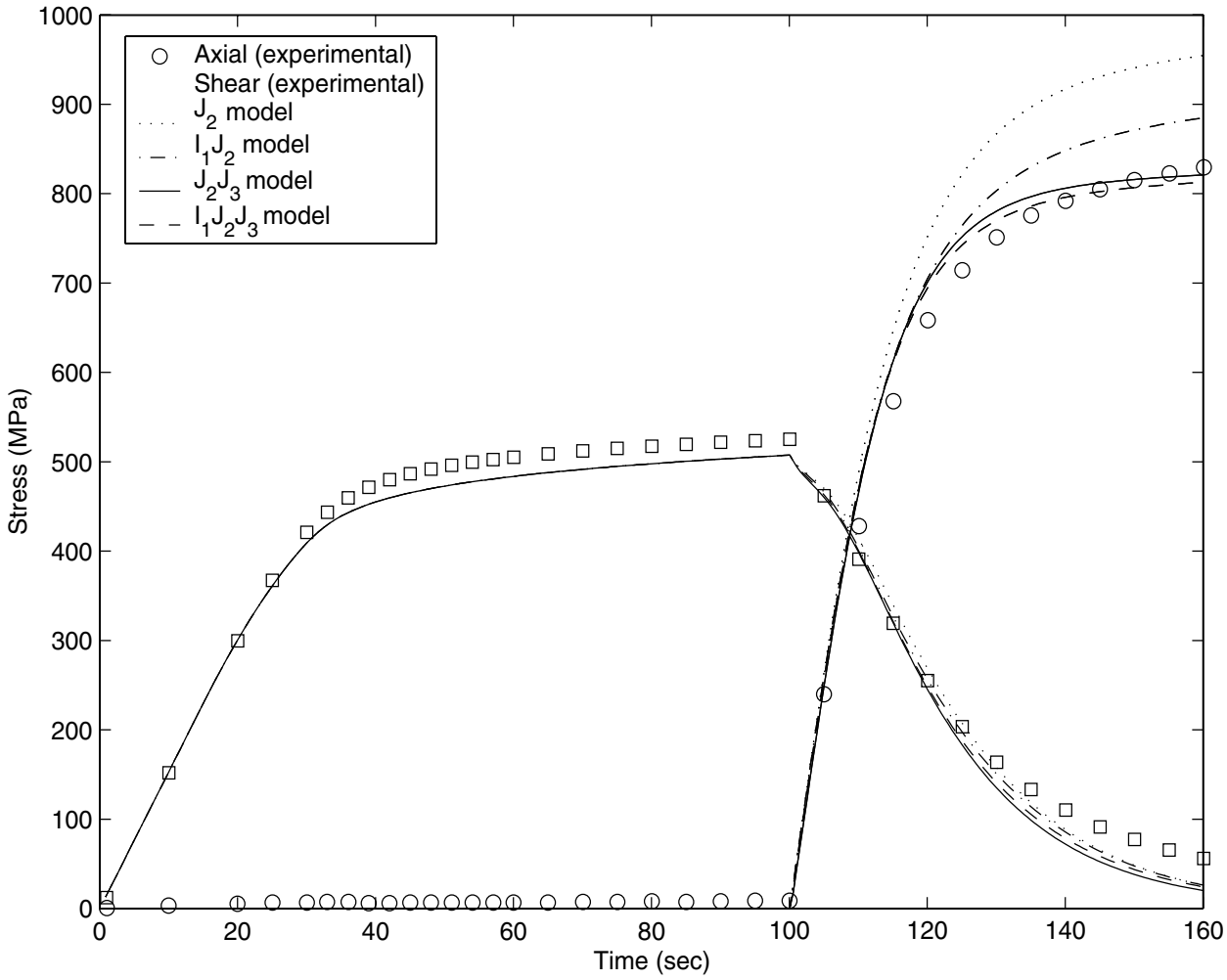

Figure D.1: Shear-tensile loading (IN4) ($m_1 = 0.6$)

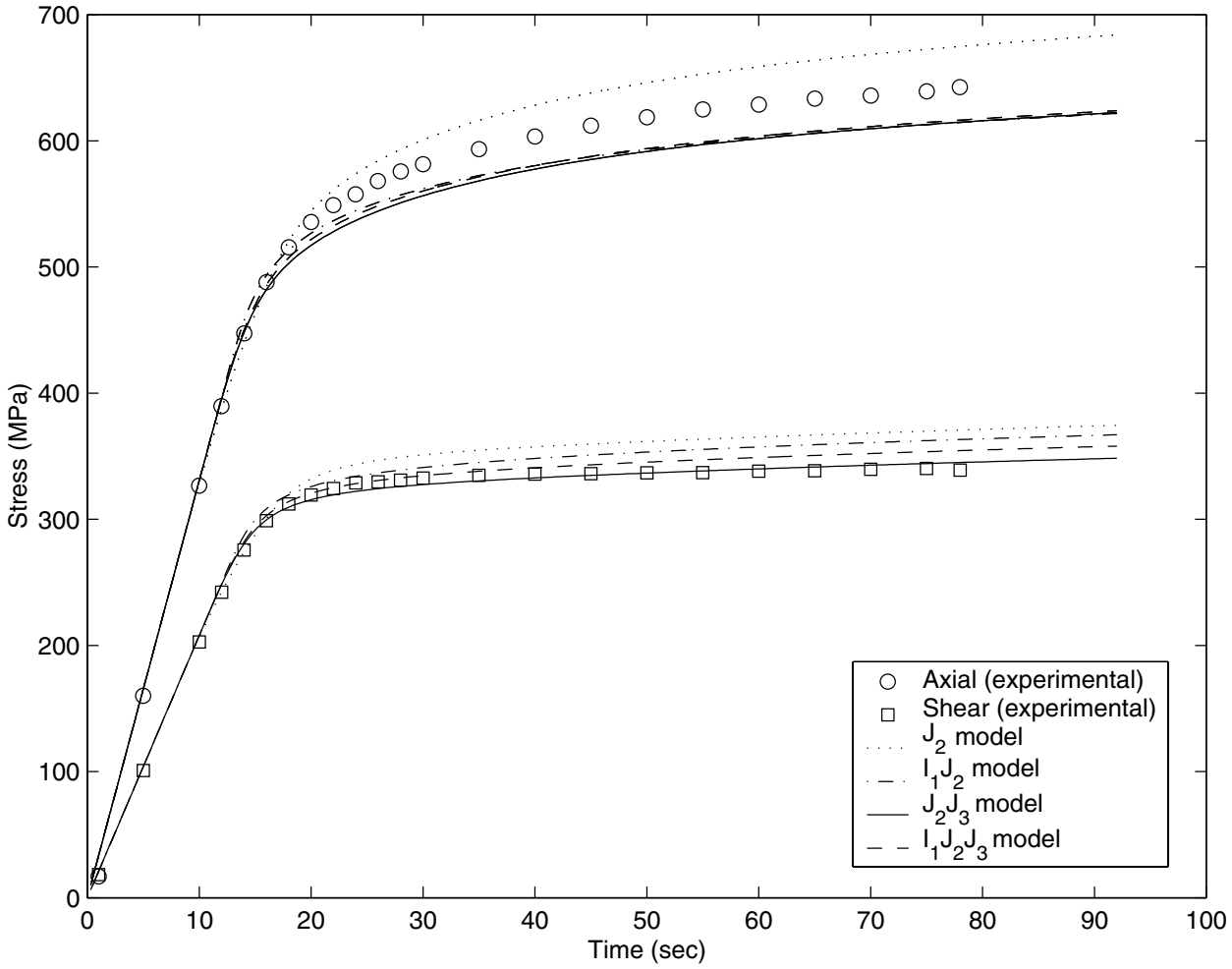

Figure D.2: Proportional loading (IN5) ($m_1 = 0.6$)

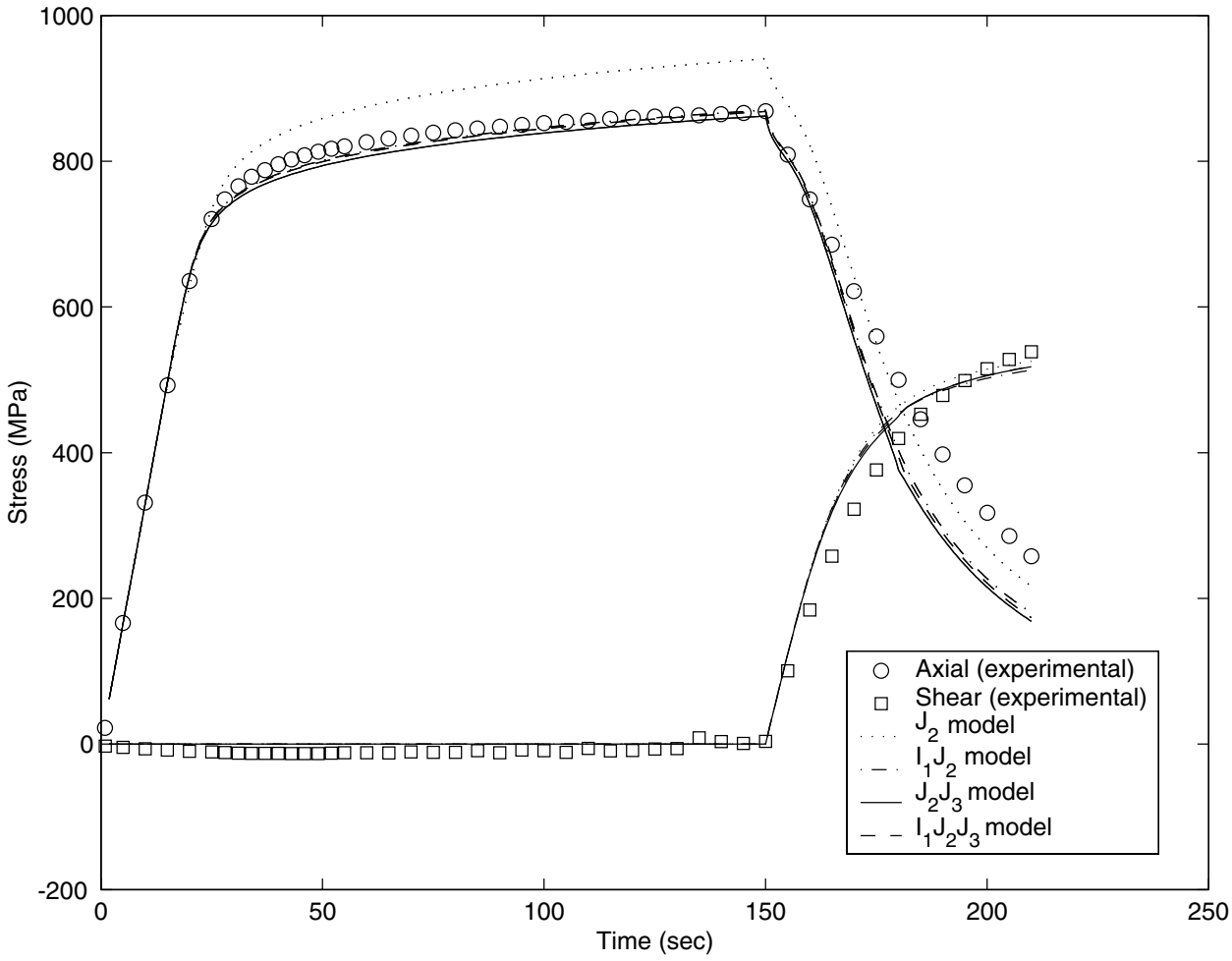

Figure D.3: Tensile-shear loading (IN6)($m_1 = 0.6$)

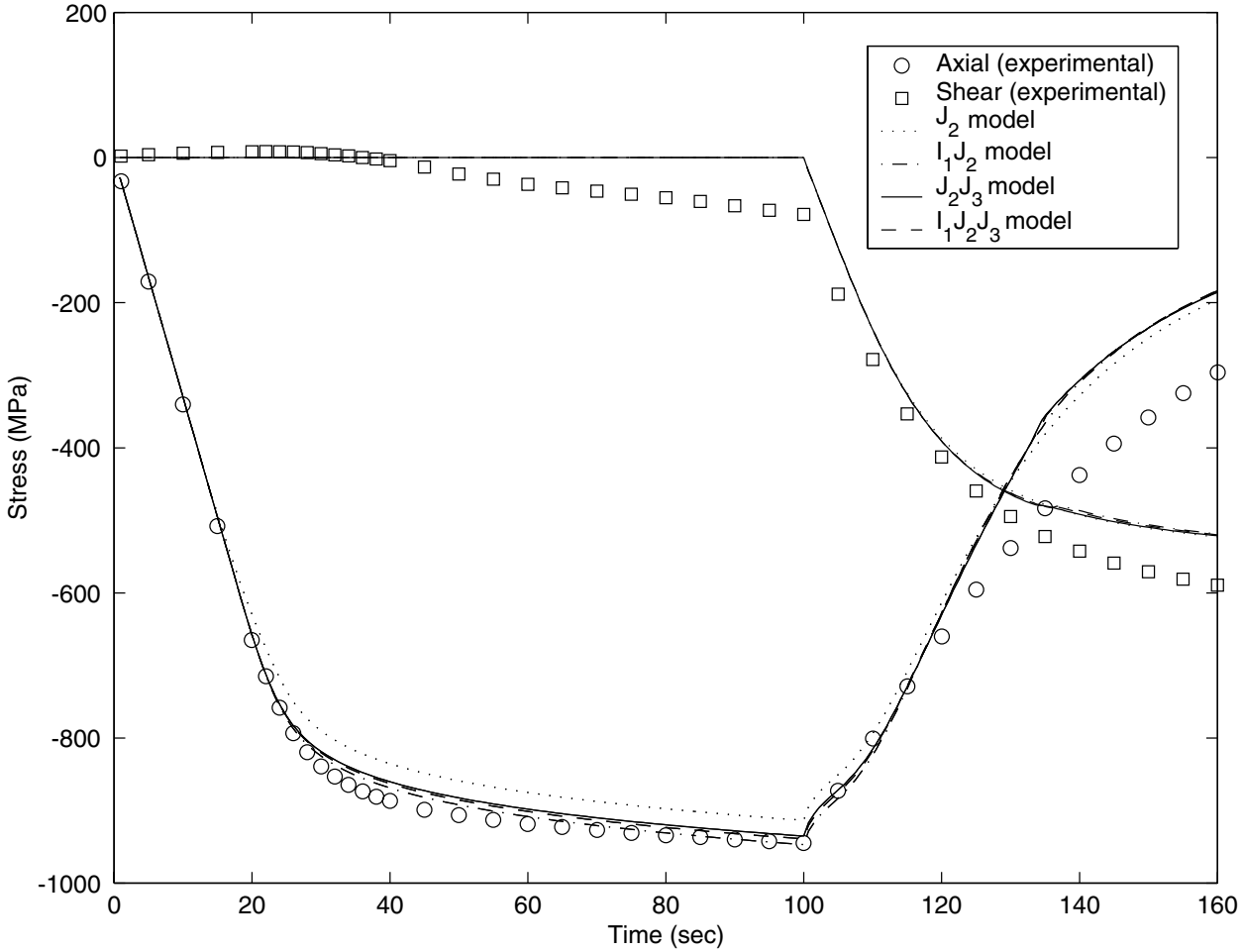

Figure D.4: Compressive-shear loading (IN2)($m_1 = 0.6$)

REPORT DOCUMENTATION PAGE

Form Approved
OMB No. 0704-0188

1. AGENCY USE ONLY (*Leave blank*)	2. REPORT DATE	3. REPORT TYPE AND DATES COVERED
	April 2001	Final Contractor Report

4. TITLE AND SUBTITLE

Viscoplastic Model Development to Account for Strength Differential: Application to Aged Inconel 718 at Elevated Temperature

5. FUNDING NUMBERS

WU–708–31–13–00
NCC3–597

6. AUTHOR(S)

Saiganesh Iyer

7. PERFORMING ORGANIZATION NAME(S) AND ADDRESS(ES)

Pennsylvania State University
227 Hammond Building
University Park, Pennsylvania 16802–6801

8. PERFORMING ORGANIZATION REPORT NUMBER

E–12668

9. SPONSORING/MONITORING AGENCY NAME(S) AND ADDRESS(ES)

National Aeronautics and Space Administration
Washington, DC 20546–0001

10. SPONSORING/MONITORING AGENCY REPORT NUMBER

NASA CR—2001-210715

11. SUPPLEMENTARY NOTES

This report was submitted as a dissertation in partial fulfillment of the requirements for the degree Doctor of Philosophy to the Pennsylvania State University, The Graduate School, College of Engineering, University Park, Pennsylvania, 2000. Project Manager, Brad Lerch, Structures and Acoustics Division, NASA Glenn Research Center, organization code 5920, 216–433–5522.

12a. DISTRIBUTION/AVAILABILITY STATEMENT

Unclassified - Unlimited
Subject Categories: 26 and 39 Distribution: Nonstandard

Available electronically at http://gltrs.grc.nasa.gov/GLTRS

This publication is available from the NASA Center for AeroSpace Information, 301–621–0390.

12b. DISTRIBUTION CODE

13. ABSTRACT ***(Maximum 200 words)***

The magnitude of yield and flow stresses in aged Inconel 718 are observed to be different in tension and compression. This phenomenon, called the *Strength differential* (SD), contradicts the metal plasticity axiom that the second deviatoric stress invariant alone is sufficient for representing yield and flow. Apparently, at least one of the other two stress invariants is also significant. A *unified viscoplastic model* was developed that is able to account for the SD effect in aged Inconel 718. Building this model involved both theory and experiments. First, a general threshold function was proposed that depends on all three stress invariants and then the flow and evolution laws were developed using a potential-based thermodynamic framework. Judiciously chosen shear and axial tests were conducted to characterize the material. Shear tests involved monotonic loading, relaxation, and creep tests with different loading rates and load levels. The axial tests were tension and compression tests that resulted in sufficiently large inelastic strains. All tests were performed at 650 °C. The viscoplastic material parameters were determined by optimizing the fit to the shear tests, during which the first and the third stress invariants remained zero. The threshold surface parameters were then fit to the tension and compression test data. An experimental procedure was established to quantify the effect of each stress invariant on inelastic deformation. This requires conducting tests with nonproportional three-dimensional load paths. Validation of the model was done using biaxial tests on tubular specimens of aged Inconel 718 using proportional and nonproportional axial-torsion loading. These biaxial tests also helped to determine the most appropriate form of the threshold function; that is, how to combine the stress invariants. Of the set of trial threshold functions, the ones that incorporated the third stress invariant give the best predictions. However, inclusion of the first stress invariant does not significantly improve the model predictions. The model shows excellent predictive capability for nonproportional load paths. Additionally, it reduces to the well-known models of Mises, Drucker and Drucker-Prager. The requisite experiments involve reasonably simple load paths in the axial-shear stress plane and hence can be performed on a variety of different materials; be they metallic, geological, polymeric, ceramic or granular. The general form of the threshold function allows representation of inelastic deformation in a range of materials.

14. SUBJECT TERMS	15. NUMBER OF PAGES
Inconel 718; Yield surfaces; Multiaxial stress; Inelasticity; Viscoplasticity; Strength differential	204
	16. PRICE CODE: A10

17. SECURITY CLASSIFICATION OF REPORT	18. SECURITY CLASSIFICATION OF THIS PAGE	19. SECURITY CLASSIFICATION OF ABSTRACT	20. LIMITATION OF ABSTRACT
Unclassified	Unclassified	Unclassified	